Experimental Evaluation of a Distributed Fiber Optic Sensor for Mining Application

by

Behrad Mollahasani Madjdabadi

A thesis

presented to University of Waterloo

in fulfillment of the

thesis requirement for the degree of

Doctor of Philosophy

in

Civil and Environmental Engineering

Waterloo, Ontario, Canada, 2016

Author's Declaration

I hereby declare that I am the sole author of this thesis. This is a true copy of the thesis, including any required final revisions, as accepted by my examiners.

I understand that my thesis may be made electronically available to the public.

Behrad Mollahasani Madjdabadi

Abstract

Triggered remote seismic events have been widely studied in the earthquake engineering context where various possible explanations have been provided, including directivity of dynamic stresses, a critically stressed environment, the presence of hydrothermal geological environments at remote distances, and so on. Similar events have been observed in underground mining regions; however, they have rarely been studied in terms of the underlying mechanisms such as the presence of faults of marginal stability, increases in the stress gradient between mined-out regions as a result of connective fractures, unclamping effect on geological features such as dikes or joint swarms, and so on.

This research was triggered in part by the hypothesis that remote seismic events in mines could be triggered when gravity-driven displacements are transferred to distances far from active mining (10's to 100's of metres). Accordingly, the thesis focuses on experimental research on a novel deformation sensing sensor for future verification of this assumption. A secondary focus is mathematical modeling to help understand the deformation mechanisms and magnitudes that may take place in a jointed rock mass.

Distributed Brillouin sensing systems (DBSs) have found growing applications in engineering and are attracting attention in the field of underground structures including mining. The capability for continuous measurements of strain over large distances makes DBSs a promising monitoring approach for understanding deformation field evolution within a rock mass, particularly when the sensor is installed away from "excavation damaged zones" (EDZ). A purpose-built fiber optic sensing cable, a vital component of DBSs, was assessed in laboratory conditions to establish the capability and limitations of this technology to monitor deformation fields over large distances.

A test program was performed to observe DBSs response to various perturbations including axial and shear strain resulting from joint movements. These tests included assessments of the strain-free cable response and the application of extensional and lateral displacement to various sensing cable lengths (strained lengths from 1 m down to 1 cm). Furthermore, tests were done to evaluate the time-dependent behavior of the cable and to observe the effect of strain transfer using a soft host material (i.e., a soft grout) under lateral displacement.

The noise level of the DBSs range was ±77 με, determined through repeated measurements on an unstrained cable. Stretching test results showed a linear correlation between the applied strain and the Brillouin frequency shift change for all strained lengths above half the spatial resolution[1] of the DBSs. However, for strained lengths shorter than half the spatial resolution, no strain response was measurable and this is due to the applied internal signal processing of the DBSs to

[1] The minimum length of a strained event that can be accurately measured by the sensor

detect peak Brillouin gain spectrum and noise level. The stability with time of the measurements was excellent for test periods up to 15 hours.

Lateral displacement test results showed a less consistent response compared to extension tests for a given applied displacement. The Brillouin frequency shift change is linearly correlated with the applied displacement in tension but it shows a parabolic variation with lateral displacement. Moreover, the registered frequency response (correlated with strain) of the system decreased significantly when the sensing cable was embedded in a sand-filled tube compared with direct cable displacement.

A comprehensive laboratory scale testing program was undertaken to study the response of the system to different loading paths in time and space domains. Purely extensional displacement fields were applied to demonstrate that the system could produce repeatable displacement responses for three different configurations of distributed strained patterns.

A borehole installation method was developed by testing the sensing cable's response while embedded in mortar beams. When the cable is directly embedded in the mortar, uncontrolled self-debonding happens that introduces uncertainties in the measurements. This limitation was overcome by anchoring debonded sections of the sensing cable at regular spacing. This arrangement produced consistent strain patterns for each strained interval. It was shown that the performance of the debonded sections changes for longer anchor spacing and for closely spaced joints where more than one joint crosses the debonded interval.

The influence of borehole diameter and strength of the filling material were evaluated for their possible effects on the strain transfer process to the sensing cable. With the anchored arrangement of debonded cables, these properties of the grout did not have a measurable effect on the results, and as long as the tensile strength of the grout is low enough to break at the joint locations, the strain transfer performance from the rockmass to the sensing cable was excellent.

A study was devoted to understanding such a deformation monitoring system under various shear displacement conditions. These included the difference in response of the system in direct shear compared to tests performed in direct tension. The system response was evaluated for various strained lengths as well as distances over which the bending strains are acting (kink lengths). The latter was found to be an important factor influencing monitoring results. In addition, the system behavior under shear displacement where the sensor is inclined with respect to the joint strike was evaluated to understand the effect of a combined extension and shear displacement. The effect of the existence of two joints over the strained lengths was assessed in both direct and inclined shear. A new relation was established between the registered Brillouin frequency shift change and all contributing components of deformation when the sensor is elongated while under shear displacement.

The testing program shows that Distributed Brillouin Sensing (DBS) technology has promise for detecting deformations over long distances. Not only strain localization occurring at pre-existing discontinuities or at developing cracks can be detected by this sensor, but also strain levels

well below the typical damage initiation threshold (~0.1%) for hard brittle rocks are above the basic noise level of the system. However, the sensing element is quite fragile when under shear displacement and can easily break at small shear displacements. Therefore, it is better to have an idea of the dominant deformation mechanism in the rock mass before the installation of the sensor. The sensor would be much more durable where the rock mass experiences less shearing.

Mathematical simulations of a 2D rock mass were carried out using the distinct element method. Two major parameters including interlocking degree and pre-existing conditions such as mined-out zones at higher levels were studied. Different rock mass models with varying block sizes, joint set orientations, and joint persistency were built to study the effect of interlock on the displacement pattern away from mining. In general, displacement as large as 5 cm could travel distances as far as 500 m away from the active mining zone. The exact displacement pattern is largely controlled by the characteristics of the joints sets. However, the transfer of large displacements was limited to distances of the size of the mining boundary, where rock mass interlocking promote arching. Furthermore, with non-persistent joint sets, a few shear slip events were noticed at higher levels whereas more remote joints did not show slip. All slip events were close to the mining boundary.

Remote shear slip events, could not be generated by changing parameters representing the degree of interlock in the rock mass. When a backfilled old mine was added to the middle height of the model, some 500 m away from active mining, results showed that a large number of joints around the old mining zone slipped due to displacements induced by the distant deeper mining. It was found that the pre-existing excavation and the mine extraction strategy is a critical factor for providing conditions under which such slip events at remote distances occur from active mining.

Acknowledgements

I would like to express my sincere appreciation to my supervisor Professor Maurice Dusseault for his ongoing support, valuable insights, and stimulating guidance throughout these years. I also wish to express my appreciation for the support and technical guidance on the thesis by my co-supervisor Professor Giovanni Cascante.

I extend my deep gratitude to Professor Peter Kaiser, whose careful guidance and attentive comments through the project were tremendously helpful. Sincere appreciation to Dr. Benoît Valley for his valuable comments, continuous support, precious motivation, and always-kind attention.

This work was funded by an equipment grant from NSERC (National Sciences and Engineering Research Council of Canada) and by CEMI (Centre for Excellence in Mining Innovation) with funds obtained from the Ontario Ministry of Research and Innovation through the SUMIT program (Smart Underground Monitoring and Integrated Technology), a collaborative research program between Ontario Universities under the leadership of Laurentian University.

I would also like to thank Professors Dana Strickland of Physics and Jenny Wen of IQC for letting me to use their labs and fusion splicers as well as UW technical staff, specifically the Structural Laboratory and Douglas Hirst, and the Science Machine shop staff and Harmen Vander Heide.

I express strong appreciation to my friends, especially Mohammadreza Jalali and Vahid Sohrabi, who always encouraged me to continue and gave me many great ideas to solve problems and see them differently.

Profound thanks to my mother Saeedeh Pourfakhraee for being the greatest mentor and supporting me in all possible ways. Special thanks to my father Hamid Madjdabadi for his unconditional love and support. To my sister Ima and brothers Behdin and Behrang, special thanks for their affection, encouragement, and cheerfulness. Many thanks to my love of life, Leila Ahmadi, who has supported me throughout the entire process. I will be grateful forever for your love, patience and moral support.

To my mother and father …

TABLE OF CONTENTS

LIST OF FIGURES

LIST OF TABLES

1. Introduction

This research is about detailed laboratory evaluation of a novel distributed fibre optic sensor to better understand its basic performance, its response in direct tension and shear, and also the optimum installation procedure in a borehole. The system is meant to measure the deformation field away from active mining and to see how the hard massive rock blocks move towards the openings. With the knowledge of deformation patterns, it becomes possible to see if there is a relation between relative rock block movement and remote seismicity; an issue that has not been understood clearly.

1.1. Mining-induced seismicity

Based on Cook (Cook, 1976), perturbations in the stress state of a rock mass around mine excavations lead to movements of the rock and this in turn may lead to slip yield events which are evidenced as mining-induced seismicity. Fracturing and seismicity are common events in deep level mining where ore extraction induces stress-driven rock mass failure (Spottiswoode, Linzer, & Majiet, 2008). Different factors influence mining-induced seismicity including the mined area (volume and geometry), extraction method (rate and sequencing), geological and rock mass characteristics and the in-situ far-field stresses at the mine depth (Milev & Spottiswoode, 2002).

Hasegawa et al. (Hasegawa, Wetmiller, & Gendzwill, 1989) explained mechanisms by which mining-induced seismicity could occur in underground mines, as shown in Figure 1-1. Extrusion of in-place rock material into an opening forms an extended cavity, whether the extrusion occurs as a rockburst or rockfall (Figure 1-1(a)). Pillar burst happens because of accumulation of unsustainable strains (stresses) resulting from both stope convergence and creep effects (Figure 1-1(b)). A mine roof (back) consisting of a strong rock that is undergoing bending will tend to fracture in tension in the bottom fiber, potentially leading to roof beam collapse (Figure 1-1(c)). More commonly, large shear displacements can occur along crushed rock zones in pre-existing faults near stope faces, and these may be called burst fractures, which create vibrations in the rock mass (McGarr, 1971). A rupture through intact rock usually takes place in a normal faulting manner (Figure 1-1(d)), and it can occur above a mine stope (McGarr & Green, 1975). Also, ruptures of a thrust fault nature (Figure 1-1(e)) can happen either in intact rock close to a stope or on a pre-existing fault in ground where high horizontal stresses exist ($\sigma_v = \sigma_3$, $\sigma_{HMAX} >> \sigma_v$). Another mechanism could happen as an almost horizontal rupture similar to overthrust faulting (Figure 1-1(f)) above the mine roof if sub-horizontal layers slip relative to each another (Hasegawa et al., 1989).

Several research studies have been devoted to understanding the connection between large seismic events and various geological structures in underground mining (e.g. (Gay et al., 1984; Lourence, Jung, & Sprenke, 1993)). Not all large seismic events will cause damage to underground structures, but those seismic events prone to induce damage, known as rockbursts or fault slip, can have severe consequences and may even generate fatalities. At the Klerksdorp gold-field mine

(Gay et al., 1984), most of the large seismic events that caused fatalities were associated with geological features such as dykes or faults. Dykes and faults play an important role in mining-induced seismicity as regions around these pre-existing features can often be at a critical state of stability such that fairly small changes in energy (alteration of stresses or strain changes) cause sudden failure. In practice, changes in elastic strains and stresses in a rock mass surrounding a stope are transformed to inelastic deformation along weaker features, such as a fault or a joint, as mining progresses (McGarr, 1971). Also, structures such as dykes or other features that lead to sharp stiffness contrasts across a narrow contact surface cause shear stress accumulations to happen naturally as mining progresses, and these surfaces are therefore more prone to rupture.

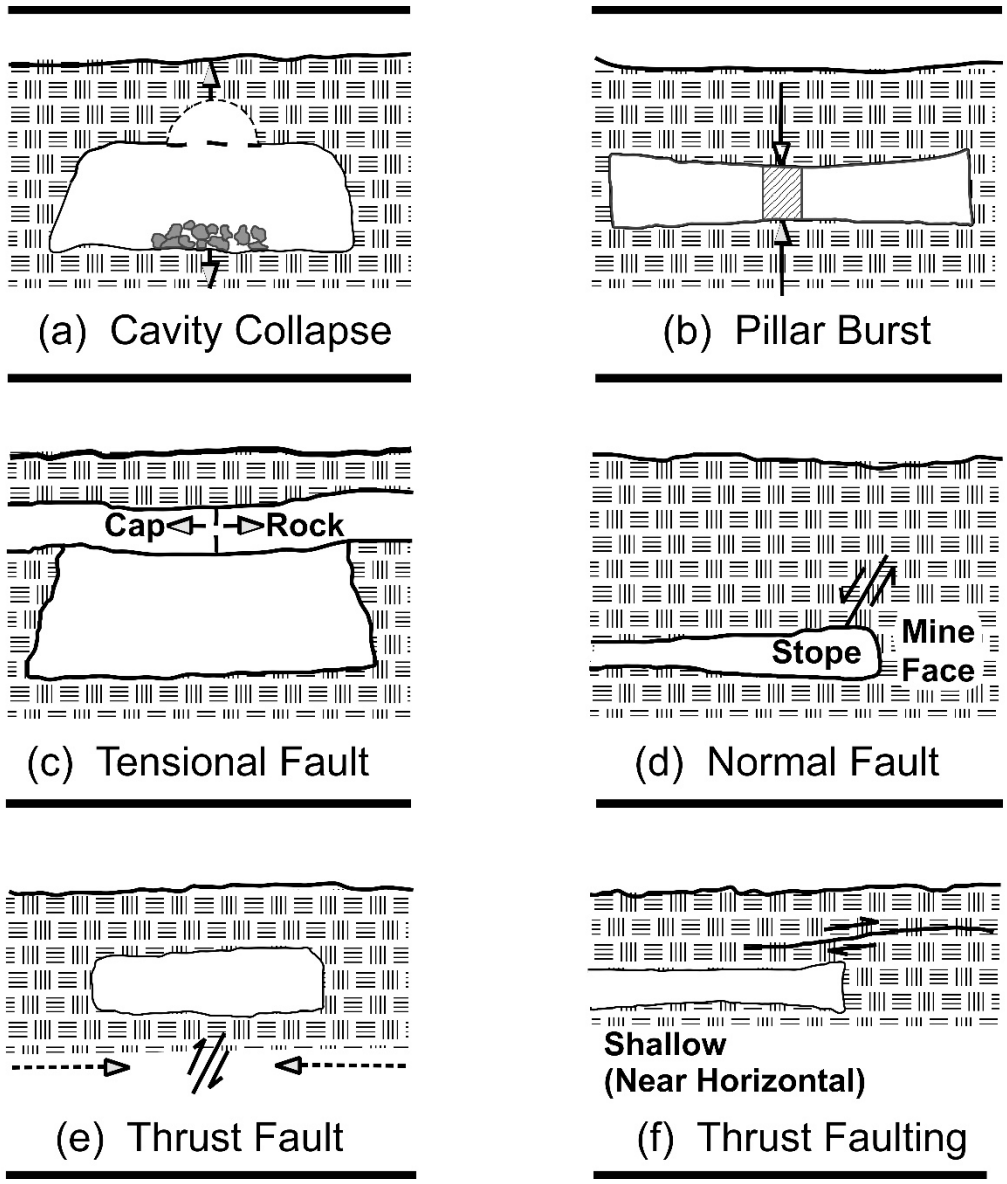

Figure 1-1. Six possible mechanisms for mining-induced tremors are schematically shown. Solid arrows represent the direction of mine-induced force on the rock mass during induced seismicity. Dashed arrow in (e) indicates ambient tectonic stress (modified from (Horner & Hasegawa, 1978)**)**

Changes in strain energy of a rock mass induced by fault slip generally depend on the location of the fault relative to the stopes. Stope convergence could happen because of mining-induced fault slip where the fault intersects the stope or is very close to it. Because of this volume change (i.e. convergence), a part of the stored energy is released. In contrast, if a fault located at a distance remote to the active stopes undergoes shear displacement, the elastic strain energy near it is redistributed to a larger volume by the slip, or the total energy decreases since no volume change occurs (McGarr, 2000). A shear fracture which intersects a tabular ore body stope would experience a shear displacement almost ten times more than a shear fracture located far ahead of the face (Spottiswoode et al., 2008). Among a number of intersecting faults, those critically oriented such that induced shear stresses are highest would most likely be activated, assuming that other factors such as the fault's strength properties are constant. In contrast, widely-spaced faults have the least chance of interaction with mining zones and developments since any shear displacement on one will not likely produce sufficient stress perturbations around the others as to trigger further slip and sudden energy release (Dupin, Sassi, & Angelier, 1993).

1.2. Problem definition and hypothesis

Typically rock failures and seismic events are directly related in space and time with active mining, generally occurring within tens of meters from the active mining front (Cook, 1976). Apart from near-field seismicity related to the mining-induced stress changes, it is expected that the more remote rock mass is seismically quiet (unless in a tectonically active area) and not affected by the mine workings. However, some failures have been observed that are spatially remote from current activity in the mine and occur at time periods not related to major blasts. These events have been considered to occur in association with geological features on a regional scale (Cook, 1976).

These remote events are often located at distances where the stress change directly attributable to the extraction of a stope would be expected to be negligible (Kaiser, Vasak, Suorineni, & Thibodeau, 2005; Urbancic & Trifu, 1995). Although stress-driven failures close to opening boundaries have been well studied through seismic monitoring (Cai, Kaiser, & Martin, 1998, 2001) and other approaches (extensometers, stress cells…), the causes for mining-induced remote seismicity remain poorly understood. Understanding of such events will increase mine safety and economy.

For this research, it is hypothesized that distant seismic events may be triggered by remote stress-changes induced by gravity-driven deformation processes (GDDP). According to this GDDP hypothesis, deformations induced by ore extraction will propagate quite far under gravitational stress. It should be noted that transfer of deformations could be facilitated by mining at lower levels Hence, based on GDDP, it is a transfer of deformations, not stress, that leads to stress changes at remote locations. .

This transfer process is a chain-like movement of discrete, massive rock blocks. Kaiser et al. (Kaiser et al., 2005) used a train analogy to describe the sequential movement of rock blocks, in that the movement will transfer along the whole system. The last car in a train will not feel the locomotive movement immediately and will start moving only with some delay. Similarly, if there

is such a delay, or a deformation gradient, in the chain-like displacement of rock blocks, stress might buildup and induce a failure if intact rock blocks and joints are already highly stressed.

1.3.1. Gravity-driven deformation process (GDDP)

When an excavation is created in an undisturbed, massive, hard rock mass, deformation transfer will be limited to the excavation boundaries. This situation is similar to block cave mining where the very first cave will stop propagating not long after the undercut has formed.

The deformation transfer will be prevented from propagating to upper levels in the rock mass because stress-arching happens. Stress-arching depends on a number of factors such as interlocking degree of the rock mass, intact rock strength (breakability of the rock), and the overall rock mass stiffness which affects the load transfer system around the mining area. Therefore, distant seismic events because of stress changes induced by deformation transfer cannot happen at remote location from the active mining because the elastic deformations attenuate quickly with distance.

The interlocking degree depends on a number of parameters such as block size and shape, which both vary with the number of joint sets, their orientation, persistency, and surface characteristics (rigidity at various scales).

With respect to the block size, scale effects should be considered. For example, numerical modeling of a block caving mine for two different block sizes with the same undercut size showed that the deformation propagated more readily to higher levels in the case of smaller block size. This is because the degree of freedom for the larger rock blocks is limited in comparison with smaller blocks and also stress-arching occurs at a relatively early stage of caving, a situation similar to that shown in Figure 1-2(a). The reader is referred to appendix A1 for the complete results of the modeling carried out.

In the 2D given example, the rock mass have only two joint sets. In the case that there are more joint sets forming larger numbers of smaller blocks that decrease the interlocking degree, or a low-strength intact rock that can break under the applied stresses, the deformation propagation will not stop at a small distance above the mining level because of stress–arching. Under such circumstances, displacement will be able to propagate further, even to the ground surface, forming a collapse chimney or resulting in a settlement trough. According to these settlement profiles within the rock mass, zero lateral deformation boundaries (DBs) will be formed, as shown in Figure 1-2(b). Formation of these DBs, might cause a deformation gradient in the movement of the massive rock blocks above the mining level. Consequently, a horizontal stress change will be induced at the DBs because of such deformation gradients.

However, there are many different situations where mining will be under progress in a disturbed rock mass. Such a disturbance could be a pre-existing mined-out block at some distance from the active mining at some higher levels. Such a condition is shown in Figure 1-2(c). Similar to the previous case in (b) deformation boundaries will also be formed in this case and the potential deformation gradient might induce a horizontal $\Delta\sigma$ at DBs. The difference between (b) and (c) is

that the rock mass surrounding the pre-excavated mines at higher levels have been disturbed. Stress redistribution around older mining zones can be possibly so high that even a small increase of the stress can result in intact rock failure. Furthermore, there are many joints around these mine openings that are critically stressed, apart from those joints that have already slipped.

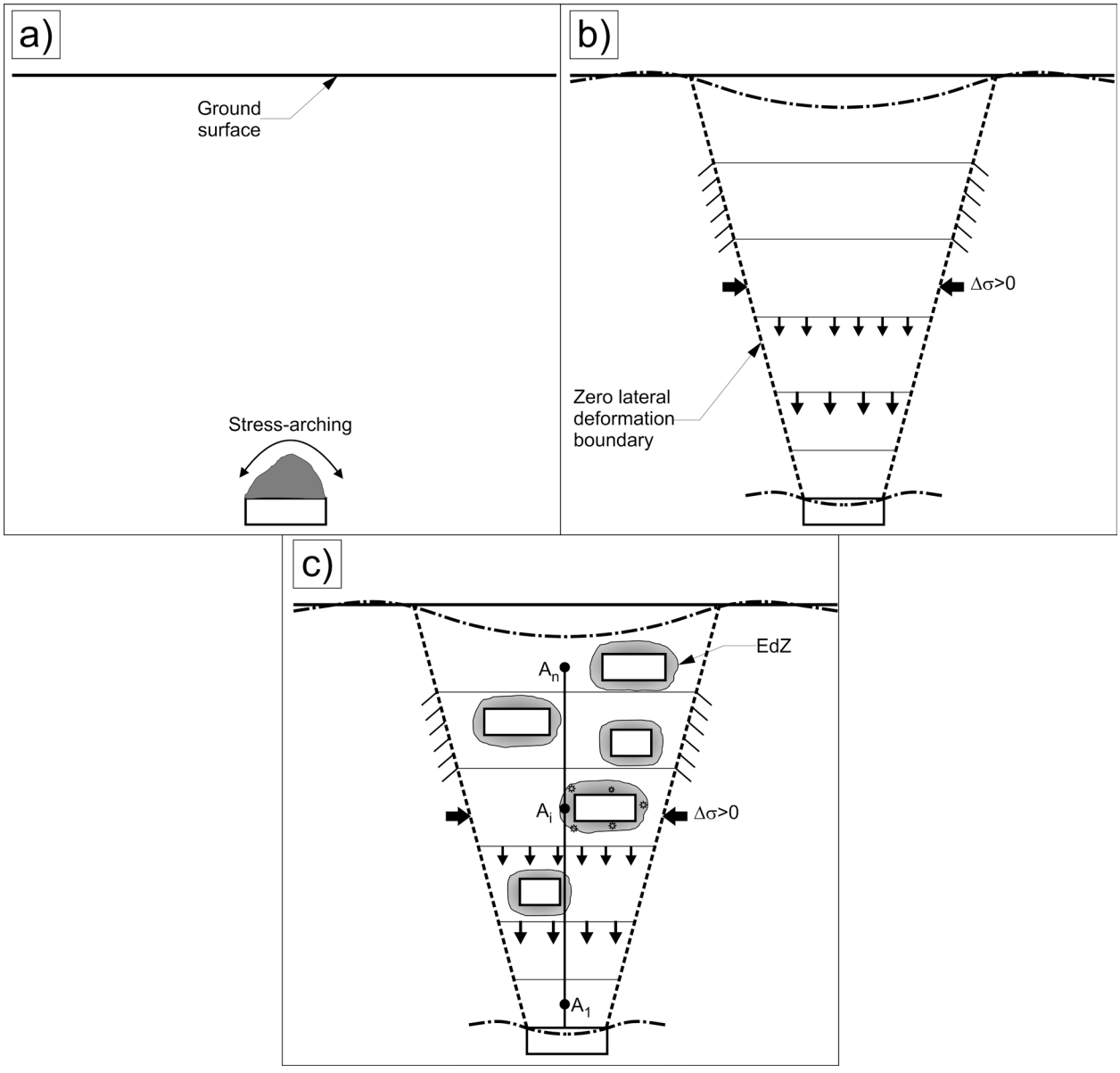

Figure 1-2. a) Stress-arching occurs when mining in massive or moderately jointed or highly interlocked rock mass. b) mining in highly jointed or less interlocked rock mass can cause displacement propagation to much higher levels so that a settlement bowl can form on the surface. c) mined-out zones above current mining levels in case (b) can result in occurrence of some seismic events around a highly disturbed rock mass (i.e. EDZ) at higher levels. This is because the stress change due to gravity-driven deformation transfer happens at the zero deformation boundaries

Case (c) in Figure 1-2 was considered for further study in numerical modeling. The objective was to understand if the GDDP hypothesis is reasonable, because mining at lower levels can cause shear slip along joints or intact rock failure when the rock mass at some distance above the mining

level was disturbed because of pre-existing excavations. The rock mass had two joint sets inclined at 60° and 120° with effective joint persistency values of 73% and 60%, respectively. Figure 1-3(a) shows the shear slip events at the middle of the rock mass around an old backfilled mine. Figure 1-3(b) show the shear slip distribution after the main mining activity is simulated using a 200 m long trapdoor, where the rock moved down 40 cm. Although stress-arching happened at some distance above the trapdoor and large displacements were prevented from propagating to upper levels, over 300 joints that were critically stressed after the old mining slipped after the simulated mining at lower levels. This simple model showed that the GDDP hypothesis can explain some remote seismicity where the rock mass is disturbed and critically stressed conditions already exist before the main (deeper) mining activity.

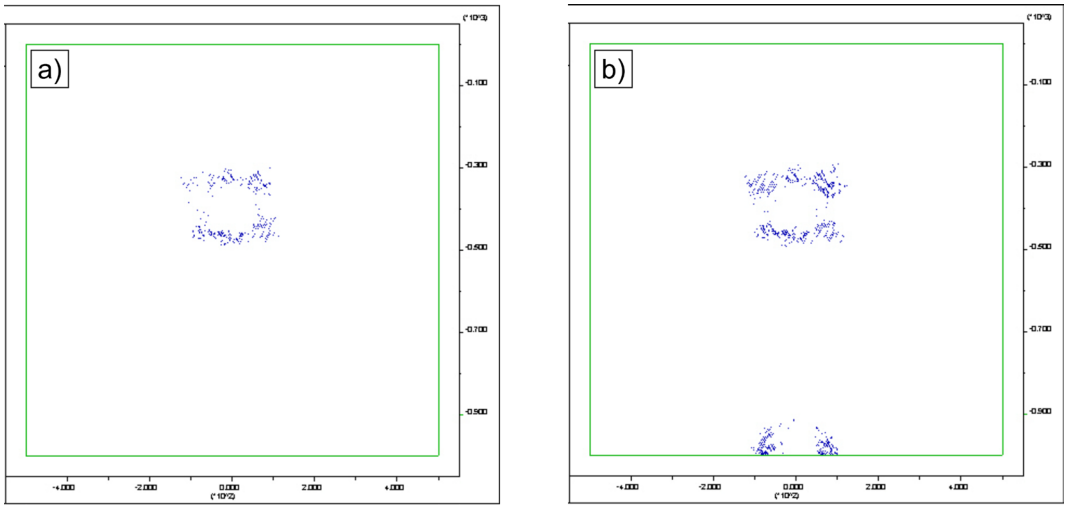

Figure 1-3. Shear slip distribution along joints in a discrete element model of a large volume of rock mass where a 100×100 m² area in the middle of the model was backfilled a) before and b) after a deeper zone was extracted.

1.3. Research motivation

The last case shown in Figure 1-2(c) is a typical condition for underground hard rock mining environments in Canada. According to the GDDP hypothesis, displacement propagates to higher levels where rock blocks move towards an opening in a sequential manner. Therefore, understanding if a deformation gradient exists between moving massive rock blocks, within which mines had been extracted, can help clarify a potential relation between GDDP and remote seismicity.

The main motivation for this thesis is, therefore, to measure the deformation between two seismically active areas, i.e. old extracted zones at higher levels above the current active mining, to see if, for example, the displacement rate at point Ai is similar to that at point A1 (similar to the condition where particles can flow in a silo), or to examine whether rock blocks are moving at different rates. To this end, measurements with a distributed deformation sensor that can return many measurement points along its length will enable us to study the deformation field away from active mining.

Such a distributed deformation sensor was installed in the Coleman Mine in Sudbury for the first time. A 25 m high sill pillar was instrumented with five distributed sensors and monitored for over two months. Three sensors were broken in early stages of the sill pillar mining, and analysis of measurements from the two remaining sensors did not yield much information. On one of these two sensors, a very high strain response was noticed in a small section, a response quite different from the rest of the sensor data. This high local strain was found to be associated with a rock block detaching from the mine back at a joint location, and confirmed with the results from optical imaging of the borehole. It was then decided to study the strain response of such a system in great detail in the laboratory before trying more field installations.

1.3. Research objectives

Deformation measurement is usually executed locally near excavation boundaries where the rock mass is most disturbed. More distant from the excavated damaged zone (EDZ), the rock mass surrounding the entire mine geometry is treated as the loading system and to date has never been directly monitored for deformations. Various parameters influence the mechanical behaviour of the system to mining activity, including the stiffness of the rock mass in the hangingwall, footwall, and orebody, and the presence of structural features such as faults and dykes. Therefore, there is a need to understand deformation fields at a much greater scale than the regional proximal to openings, i.e. at the mine scale.

This research seeks to better understand the underlying mechanisms contributing to the trigger of distant seismic events in underground mines. Hence, the main objective of the research was to study a novel deformation sensing system that is capable of monitoring deformation at large distances from mining such that a better understanding of the process leading to the occurrence of remote seismicity in mines.

A better understanding of the relation between deformation fields within the rock mass and remote seismic events can help test hypotheses such as at remote distances. The tested deformation measurement device is therefore meant to be deployed to record the deformation pattern away from active mining. Although optical fibre technology has been in use for almost a decade in different engineering contexts, there is a limited number of cases where such a system has been applied in underground mining. Consequently, a detailed examination of a suitable fibre optic system is needed before deployment in an underground mining environment where many activities and factors may have an adverse effect on measurements. This thesis presents the findings of a comprehensive laboratory testing program that was set up to explore the following:

- study the performance of the selected system in terms of accuracy, resolution, and repeatability;
- define the base noise level of the system;
- establish the relation between deformation and the system's internal measured parameter, i.e. frequency (Chapter 2);

- explore the sensing system's response to direct tension;
- explore the system's response to spatial and sequential distribution of applied deformations;
- investigate the strain transfer processes when the sensor is embedded in a filling material;
- explore time-dependencies of the system response when under constant strain; and
- investigate the response to direct shear displacement when the sensor is installed in a borehole crossing various joints at different inclinations.

In addition, practical questions for successful utilization of fiber optics are addressed:

- Is the system capable of registering the relative movement of a series of rock blocks next to each other?
- What would be the system response be when rock blocks deform in different sequences over the course of mining?
- What is the best installation procedure?
- What grout properties are required for hole filling to achieve optimal strain transfer?
- What borehole size should be used for the system to have optimum performance?

1.4. Deformation measurement

1.4.1. Conventional and new sensors

The main instrument conventionally used for rock mass deformation measurement is the borehole extensometer (BX). These instruments have either single or multiple anchors (MPBX) that measure the average deformation of the rock mass between that anchor and a fixed reference surface. MPBXs measure the deformation in one direction, which is along the rod axis; therefore they must be installed in other directions in order to obtain the deformation tensor.

There are other instruments that work based on deformation measurement. For example, overcoring stress measurement devices use electrical strain gauges (ESG). There are some drawbacks using ESGs in underground excavations such as difficulty in proper attachment to the rock, monitoring of strains in the close vicinity of the gauge, sensitivity to noise and electro-magnetic interference, frailty in damp and wet environments, and low stability for long-term monitoring (Bhalla, Yang, Zhao, & Soh, 2005).

Another common type of strain gauges is based on the vibrating wire principle (VWSG). VWSG measures the vibration frequency of a tensioned wire attached across a gage length to compute the strain the rock is experiencing (Y. W. Yang, Bhalla, Wang, Soh, & Zhao, 2007). There are some advantages in using VWSG over ESG such as consistency in long-term strain monitoring, and insensitivity to signal distortion during transmission over long distances since they are frequency-based. However, they are more expensive and massive than ESGs and are easily affected by external mechanical vibrations (Bhalla et al., 2005).

Recent developments in fiber optic sensor (FOS) technology have shown great potential for their use as the next generation of sensors. They are capable of conveying a huge amount of data at gigabit rates. There are also many advances in the various optoelectronic devices which can be combined with fiber optics to create different types of sensors (p, T, ε, vibrations,…) (Fidanboylu & Efendioglu, 2009).

Fiber optics based sensors (FOS) have many advantages compared to conventional electronic sensors including higher sensitivity, larger dynamic range, wider frequency bandwidth, more varied configurations or geometries, locatable near in situ operations, multiplexing capability to form sensing networks, remote sensing capability, more resistant to harsh environments, reliable long-life operation, electromagnetic pulse (lightning) immunity, lightweight, and multifunctional sensing capabilities (Homuth, Chen, & VanEeckhout, 1998).

1.4.2. Spatial measurement methods

1.4.2.1. Local sensors

Average strain over a select distance within the rock mass has traditionally been measured by extensometers. The simplest extensometer has only one anchor so that deformation of the rock mass between this point and a fixed reference surface is measured. More anchors can be used in an extensometer where the relative rock mass deformation can be measured along different lengths.

Direct strain measurements at a single point of the rock mass can only be achieved by directly mounted strain gauges. Stress measurement in underground structures such as overcoring with the CSIRO-cell is based on this kind of change-in-strain monitoring. Also, during laboratory tests on rock specimens, strain gauges are usually glued to a small part small part of the rock surface at axial and transverse directions (although some rock laboratories use far longer and more expensive strain gauges covering 40-60 of the axial length and 50% of the circumference.

Various tests have been accomplished in the laboratory to explore the possibility of utilizing point-wise FOS for static and dynamic measurements of deformation, stress, and temperature in underground structures in rock. Fiber Bragg Grating (FBG) (described in Chapter 2) methods have been used in a number of experiments for performance compared to ESGs (Y. Yang, Annamdas, Wang, & Zhou, 2008). Furthermore, FBGs have been utilized in rods to form a Bragg Grating Extensometer (BGX) (Schmidt-Hattenberger & Borm, 1998) and embedded in rock bolts in an underground mine for evaluating its dynamic response (Schmidt-Hattenberger, Borm, & Amberg, 1999). Also, FBGs have been used in arrays in an underground mine to explore correlations between small-scale and large-scale deformations induced by deep mining (H. F. Wang et al., 2010).

1.4.2.2. Semi-distributed sensors

As mentioned earlier, because of inhomogeneity of the rock mass at different scales (crystal size to km-scale), knowledge of the deformation just at one or even several point locations around

an excavation might not be sufficient for the purpose of continuous safety assessment or design verification. Multiplexing gauges spaced at some distances along a line (e.g. extensometers in a grouted hole) has been used for linear displacement and deformation measurement of the rock mass in the vicinity of excavations.

Multiplexed FBGs have been used in mining sites for measuring deformations in the roof of tunnels, stopes and in hanging walls, for load variations in pillars between stopes where the sensors are incorporated in standard pressure cells (Pierre Ferdinand et al., 1995), for monitoring strain and temperature around a tunnel with semi-distributed sensors along a rockbolt (Nellen, Frank, Brönnimann, Sennhauser, & Broennimann, 2000), for monitoring the roof state with sensors distributed along steel bars as strain gauges and long-gauge-length displacement sensors, as well as environmental sensors to collect real time data on parameters including water pressure and temperature (Liu et al., 2009).

The location of sensors along an optic fiber can be selected based on the requirements for monitoring with a denser quantity of sensors for places with higher strain localizations (high strain gradients). Some examples include the following: a lesser number of FBGs were installed at the lower part along strengthening dam anchors compared to the upper part, where the surrounding rock mass would receive much of the anchor loads (Dietz, Habel, & Feddersen, 2001) For evaluation of subsidence behavior of unconsolidated strata into which the main shaft of a mine in China was bored, 10 places at different layers of the strata were considered for embedding FBG sensors incorporated into glass fibre reinforced polymer (GFRP) (Chai et al., 2011), as well as two intervals along a borehole; where a potential slip surface for slope movement along fractures was anticipated, it was monitored with multiplexed FBGs grouted with an expanding admixture (Moore, Gischig, Button, & Loew, 2010).

1.4.2.3. Fully distributed sensors

Distributed sensors have the capability to record data within a volume of rock along the entire length of a monitoring profile. In this manner a large number of points can be continuously monitored just using a single fiber optic sensor (Roland Hoepffner, 2008; Daniele Inaudi & Glišić, 2006a).

The technology employed for this research falls in this category. For the purpose of measuring gravity-driven rock mass deformation processes (to assess the hypothesis of this thesis), it is required that a sensor have special characteristics and capabilities to continuously measure relative movement over long distances and remote from active mining. Before this technology can find field application, several potential limitations need to be assessed and relations established (e.g., between fibre strain and axial/shear movement of rock).

There is currently a gap in static deformation measurement devices that are able to monitor large structures with numerous measurements per sensor. Although multiple point borehole extensometers (MPBX) have been used for similar objectives, there are certain drawbacks in using them such as a limited number of points along the borehole and requirements for larger borehole

size as the number of points increases. It is anticipated that fibre optic monitoring can overcome these deficiencies.

1.5. Thesis structure

The thesis includes seven chapters. This first chapter provides the background and an overview of the subject matter, presents the problem, and outlines the research goals. The second chapter "Distributed Brillouin Sensing Technology", provides a general summary of available distributed sensing systems and a more detailed review of the Brillouin backscattered system working principles. This chapter also includes a description of a number of technology applications in different engineering projects.

Chapters 3 to 5 constitute the main body of the work performed for this research. The paper related to Chapter 3 has been published in a peer-reviewed journal (Measurement), the paper related to Chapter 4 has been submitted to a peer-reviewed journal (International Journal of Rock Mechanics and Mining Sciences), and the work described in Chapter 5 is being prepared for submission.

Chapter 3 presents an overview of the distributed sensing system adopted for the laboratory test conducted for this thesis. In this chapter, the strain-free response of the sensor, the base noise level, the relation of deformation and the system's internal measuring parameter is established, the repeatability and time-dependent response is examined, and the sensor response in simple tension is studied and reported.

Chapter 4 discusses the capability of the system to detect the spatial distribution of strained sections with respect to the system limits and the size of the induced strains. In addition, the system was evaluated for its performance in the detection of strain events in different time and space sequences. This chapter also provides a comprehensive study on the optimum installation procedure for field installations. The tests addressed issues of installation: whether the sensor should be directly embedded in grout or debonded along its length at certain locations, what grout properties should be used, and what borehole size should be drilled.

Chapter 5 presents the last task of the testing program in which the system is assessed when the sensing elements are strained by shear displacements. The sensor was studied under direct shear when it was it was attached to a surface by regularly spaced pins or when it was embedded in a borehole filled with grout. Shear at single or multiple joints at different inclinations to the sensor was studied.

Chapter 6 summarizes the outcomes of the research and provide some recommendations for future studies.

Appendix A elaborates on the gravity-driven deformation process, introduced in Section 1.2, and on numerical simulation to quantify the deformation mechanism and to explain the potential for remote seismicity. Accordingly, numerical simulations of a large assembly of rock blocks were performed and a number of parameters were varied during a parametric analysis to study the

physical processes that may give rise to the distant seismic events occasionally noted around mines.

2. Distributed Brillouin Sensing Technology: Principals and Applications

Parts of this chapter have been extracted from a published paper in the journal "Measurement", with the following citation:

Madjdabadi B, Valley B, Dusseault MB, Kaiser PK. Experimental evaluation of a distributed Brillouin sensing system for measuring extensional and shear deformation in rock. Measurement 2016;77:54–66. doi:10.1016/j.measurement.2015.08.040

2.1. Point fiber optic sensing basics

2.1.1. Fiber optic structure

A fiber optic sensor has three components (Figure 2-1): a core, a cladding, and a coating or buffer. Optical fibers are of two design types called single mode and multimode that differ only in the core diameter (Fidanboylu & Efendioglu, 2009).

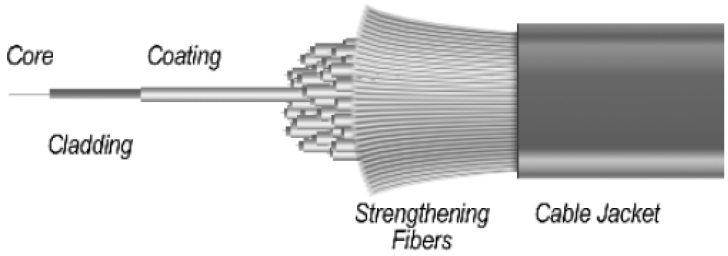

Figure 2-1. Basic structure of an optical fiber (Fidanboylu & Efendioglu, 2009)

A fiber optic sensor works based on guiding light along its length utilizing the "total internal reflection". The critical angle of incidence is the angle at which total internal reflection happens. As shown in Figure 2-2, when light incidence with an angle greater than the critical angle occurs, light is entirely mirrored back into the glass medium (Fidanboylu & Efendioglu, 2009; Roland Hoepffner, 2008).

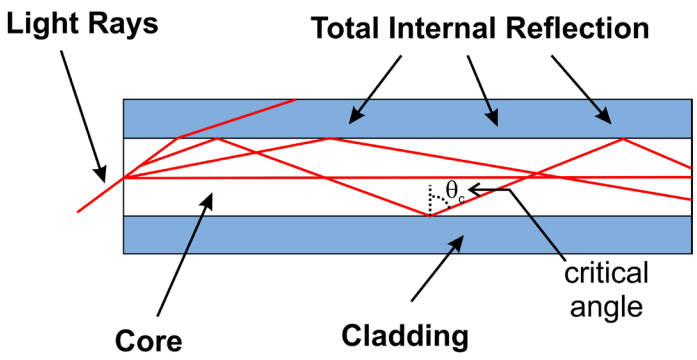

Figure 2-2. Total internal reflection in an optical fiber (modified from (Fidanboylu & Efendioglu, 2009)**)**

2.1.2. Sensing components

An optical fiber sensor system has an overall structure consisting of five major parts (Figure 2-3): 1) an optical source such as a Laser, LED, Laser diode, etc., 2) the optical fiber, 3) the sensing or modulator element which converts the measurand to an optical signal, 4) an optical detector, and 5) processing electronics such as an oscilloscope or optical spectrum analyzer.

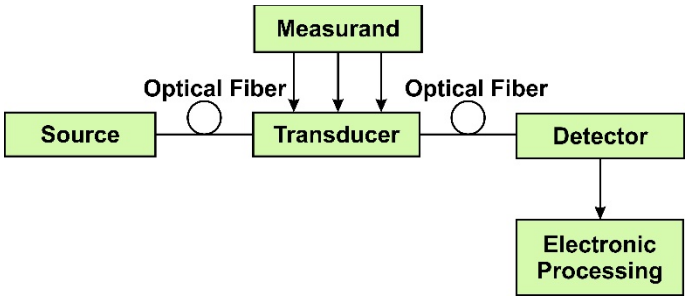

Figure 2-3. Basic parts of an optical fiber sensor system (modified form (Fidanboylu & Efendioglu, 2009)**)**

Changes in the physical property of the glass core of the optical fiber are measured. The changes in the fiber result from mechanical interactions of the surrounding environment or any temperature change (Roland Hoepffner, 2008).

2.1.3. Fiber optic sensor types

Fiber optic sensors are categorized into three classes based on sensor configuration, operating principle, and application. Based on the location of the sensor, two types (intrinsic and extrinsic) define the sensor configuration. According to application, there are three sorts of sensors: physical, chemical, and bio-medical. The light can be modulated in four ways based on changes in intensity, phase, frequency, and polarization (Fidanboylu & Efendioglu, 2009; Homuth et al., 1998).

Intensity Based Fiber Optic Sensors, also known as intensiometric FOS, rely on the variations of the radiant power transmitted through an optical fiber (Heasley, Dubaniewicz, & DiMartino, 1997). Intensity-based sensors often use multimode large core fibers, as they need more light. They take advantage of simplicity of operation, low cost, possibility of being multiplexed, high potential to act as real distributed sensors (Fidanboylu & Efendioglu, 2009), good performance at recording

temperature, high pressure, and high voltage (Homuth et al., 1998). However, they have some limitations; for example, the relative measurements and changes in the intensity of the light source may cause unrealistic readings unless an accurate referencing system is used (Fidanboylu & Efendioglu, 2009).

Phase Modulated Fiber Optic Sensors, also known as interferometric FOS, use changes in the phase of light traveling within the fiber induced by the quantity, e.g. strain, being measured (Heasley et al., 1997). In an interferometer, the light is separated into two beams where one beam is subjected to the sensing environment experiencing a phase shift, while the other is used as a reference preserved from the sensing environment, after which the beams are remixed and interfere with each other.

Wavelength Modulated Fiber Optic Sensors are based on the variation in the wavelength of light to detect changes in, e.g. strain. The most usual type of these sensors is called the fiber Bragg grating (FBG). Among all various available point fibre optic sensors, FBG has found great approval in the field of underground structures monitoring, especially strain monitoring (Y. Yang et al., 2008).

Fiber Bragg gratings (FBGs) are made by creating periodic changes in the refractive index in a single-mode fiber core. They are mostly produced using the exposure of the core to UV projection interference pattern. According to the structure of the grating, if light from a broadband source reaches it, a part of the light is mirrored back while the rest of the light passes (Figure 2-4). Studying the reflected wavelength of a BG or its variation gives information about strain and temperature changes (Bhalla et al., 2005; Nellen et al., 2000).

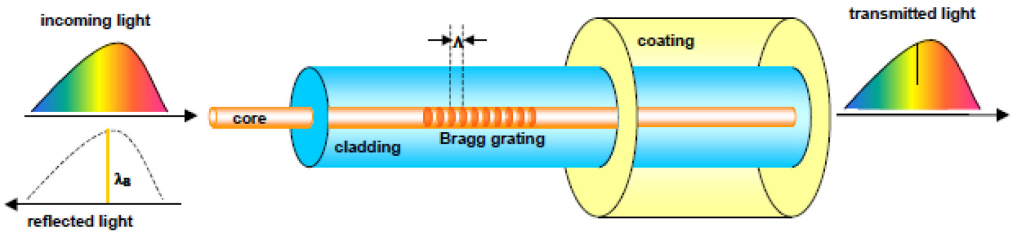

Figure 2-4. Optical fiber Bragg grating principle (Nellen et al., 2000)

Periodicity of the grating and the photo-elastic effect expand or contract when the Bragg wavelength changes after an external mechanical strain is applied. Similarly, temperature changes can lead to thermal expansion or shrinkage of the periodic grating as well as the refractive index. These variations show that FBGs can be used as sensor elements to record strains and temperatures. Furthermore, a temperature correction is needed if a FBG works as a strain sensor. To do such a compensation correctly, another FBG is installed closely to the strain sensor so that it records the wavelength shift because of temperature variation only (Bhalla et al., 2005).

2.2. Types of distributed sensing

The concept of distributed sensing is simple: it is meant to replace numerous point sensors with a single linear sensing element along which the sensing system can provide a value for the quantity to be monitored, such as strain. The sensing element in this concept plays a role not only as the transmission medium of the signal from/to the processing device, but it also converts the measurand into a modulation of the signal. Proper modulations on the signal can be obtained by identifying the appropriate phenomenon activated by the measured quantity (Luc Thévenaz, 2006).

When light is sent through an optical fiber, the light interacting process which is called scattering causes losses. A small portion of the light is back-scattered, propagating in the opposite direction of the pulsed light, and it is used for sensing purposes. Three types of light scattering happen in an optical fiber: Rayleigh, Brillouin, and Raman scattering (Figure 2-5). A pair of spectra observed on both sides of the Rayleigh peak are the Brillouin scattered lines. The left spectrum with a frequency lower than that of the incident light is called the Stokes peak, while the right spectrum with an up-shifted frequency is called the Anti-Stokes peak.

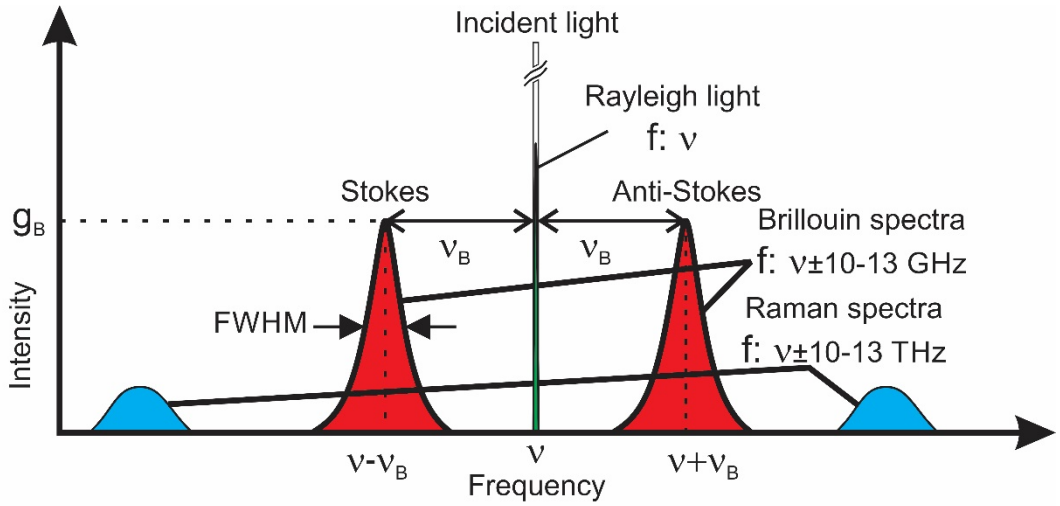

Figure 2-5. Typical spectra of scattered light in an optical fiber. ΔT affects both Raman and Brillouin components, whereas only strain changes the Brillouin component (modified from [21]). FWHM stands for the full width at half maximum.

These techniques all use both time and frequency domains to understand the location and the intensity of all events along the fiber length (X. Bao & Chen, 2012). Raman and Brillouin scattering have found great acceptance as sensing methods for distributed sensors. Both are based on the difference between the optical properties of the pulsed and the back-scattered lights. Compared to the incident light frequency, ν, the Raman scattering light is shifted ±10-13 THz, whereas Brillouin scattering frequency varies by ±10-13 GHz (Adachi, 2008). The intensity of Raman scattering light is sensitive to temperature changes (ΔT), making it a reliable and widely used temperature sensing system.

Scattering can be either spontaneous or stimulated, considering the mechanism by which the magnitude of the measured quantity is converted into a modulation of the position-dependent light

(Luc Thévenaz, 2006). In spontaneous scattering, the medium property is not strongly affected when the input light is scattered. This type of scattering is the principle used for the Rayleigh scattering based optical time domain reflectometry (OTDR), but it has also been successfully implemented using the two inelastic Brillouin and Raman scattering.

On the other hand, the optical property of the medium might change if the intensity of the light rises to a certain level. Under these circumstances, the scattered light is proportional to the power of the launched light, and the scattering type becomes a stimulated scattering. In short, the scattering regime evolves from spontaneous to stimulated when the medium behaviour changes from linear to non-linear (X. Bao & Chen, 2012).

2.2.1. Rayleigh scattering

In the Rayleigh scattering process the incident and scattered light have the same frequency, i.e., no frequency shift occurs, hence it is an elastic process. Furthermore, it is a linear scattering process in which the scattered light has a proportional power to that of incident light. Also, the spectra of the pulse has a width in the MHz range (X. Bao & Chen, 2012).

An optical time domain reflectometer, first demonstrated more than two decades ago (Barnoski, Rourke, Jensen, & Melville, 1977), that benefits from the Rayleigh scattering characteristics is used in order to evaluate losses and locate any break or other anomalous trends in fiber optic cables and networks because of high spatial resolution (discussed in Section 2.2.5) and high sensitivity (Juarez, Maier, & Taylor, 2005).

2.2.2. Raman scattering

Since the scattered light has a different frequency with respect to the frequency of the incident light, both Raman and Brillouin scattering are inelastic scattering. The spontaneous Raman loss occurs as a result of the interaction of the input light with thermally excited acoustic waves; therefore the scattering is temperature dependent (Adachi, 2008).

The ratio of the power scattered at the wavelengths of the Stokes peak to that of the Anti-Stokes peak is found to be exponentially dependent on temperature. The accumulated power in the Stokes and Anti-Stokes scattered waves determines the sensitivity of the system to temperature change (Luc Thévenaz, 2006). Using a Raman system with multi-mode fibers, a resolution of 0.1°C for ΔT and a spatial resolution of 1 m over a 10 km length is feasible (Daniele Inaudi, 2003).

2.2.3. Brillouin scattering

As a potential replacement for the classic OTDR to measure local attenuation along a fiber optic, Distributed Brillouin sensing was initially proposed in the late 1980s (Horiguchi & Tateda, 1989). However, it was quickly found that there were more capabilities for sensing because of the intrinsic sensitivity of Brillouin scattering to temperature and deformation changes in the sensing element (Luc Thévenaz, 2010).

In spontaneous Brillouin scattering, the scattered light reaches a peak over its sharp spectrum (Figure 2-5) at a frequency shifted from the pulsed light computed by Eq. 2.1, known as the Brillouin frequency shift, ν_B.

$$\nu_B = 2nV_a/\lambda_o \qquad (2.1)$$

Here, n is the effective refractive index of the fibre, V_a (~5800 m/s) is the acoustic wave velocity of the fibre core, and λ_o is the vacuum wavelength of the incident light. V_a is dependent on temperature and density changes because of strain along the sensing fibre, as is the Brillouin frequency shift. The acoustic velocity, V_a, in a solid is dependent on the bulk modulus, K, and the material density, ρ, according to Eq. 2.2:

$$V_a = \sqrt{K/\rho} \qquad (2.2)$$

The material density changes with temperature because of thermal expansion, therefore the frequency at which the Brillouin spectra peaks also varies with temperature (ΔT). The material density can also be altered with any deformation ($\Delta\varepsilon$) along the fiber length (Luc Thévenaz, 2010). Hence, the Brillouin frequency shift dependence to strain and temperature change can be given by Eq. 2.3:

$$\nu_B = \nu_{B0} + C_\varepsilon \Delta\varepsilon + C_T \Delta T \qquad (2.3)$$

The Brillouin frequency at the initial reading at a given (T,ε) condition is ν_{B0}, and $\Delta\varepsilon$ and ΔT are the strain and temperature changes at subsequent measurements.

In comparison with other distributed sensing techniques, there are a number of advantages in using Brillouin scattering (Luc Thévenaz, 2010):

- In this technique, standard single-mode fiber optics are used; since these fibers are low-loss they can provide several tens of kilometers of distance range as well as compatibility with telecommunication components.
- Brillouin scattering is based on frequency modulation, therefore it is more accurate and stable for long-term use compared to intensity-based Raman techniques.
- Using stimulated Brillouin scattering technique, a much greater intensity of the scattering process is possible resulting in a higher signal-to-noise ratio.

2.2.3.1. Brillouin optical time domain reflectometry (BOTDR)

Similar to the Rayleigh based OTDR, in this method the spontaneous Brillouin light backscattered from an intense pulse is measured as a function of time (Horiguchi, Shimizu, Kurashima, Tateda, & Koyamada, 1995). Although the Brillouin backscattered signal is 100 times weaker than the Rayleigh backscattering, it is amplified by coherent mixing with the pumped light. The frequency of the modulated backscattered signal is scanned in a step-wise manner: the reconstruction process of the frequency distribution of the backscattered signal at each position

can be accomplished through analysis of the signal amplitude as a function of frequency and locating the frequency at which the Brillouin spectra peaks.

This measurement technique has proven to be an efficient sensing device in some field situations, since access is only required to one fiber end. These fibre optic sensors can provide numerous measurements in a 10 km distance range with a 1 m spatial resolution. With a spatial resolution of 2 m, the monitoring length can increase to 30 km (Luc Thévenaz, Nikles, Fellay, Facchini, & Robert, 1998). Measurement resolution can reach 1°C for ΔT and 2×10^{-5} for $\Delta\varepsilon$ sensing (Daniele Inaudi & Glišić, 2006b). Such figures are based on the 2^{14} times signal averaging.

2.2.3.2. Brillouin optical time domain analysis (BOTDA)

This method benefits from the stimulated regime of Brillouin scattering (SBS) and works based on a non-linear interaction. In stimulated scattering, BOTDA, a weak continuous wave (CW) light called the probe beam is back-propagated into one end of the fiber while an intense pumped pulse is simultaneously sent into the other end. The stimulation process, i.e. gain, becomes maximized when the frequency difference between these two beams is equal to the Brillouin frequency shift. The gain process is accomplished through monitoring the power transfer ratio from the pumped light to the probe light at certain light frequencies in a step-wise manner. The Brillouin gain spectrum can therefore be locally rebuilt when the gain as a function of frequency at any individual sampling point along the fibre optic is analysed, as shown in Figure 2-6.

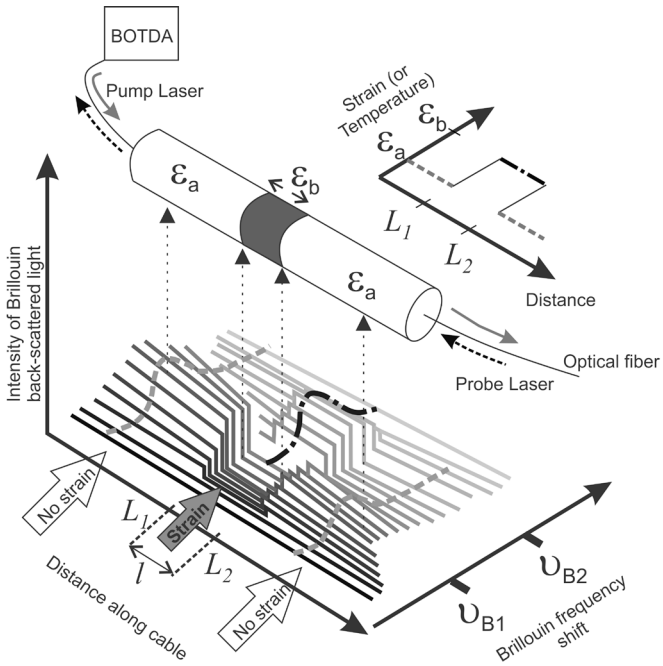

Figure 2-6. Effect of strain on Brillouin gain spectrum for a BOTDA system; the Brillouin gain peaks when the frequency difference between pump and probe signals becomes equal to the local Brillouin frequency shift (modified from [21])

According to the BOTDA scheme, the measurement is performed in a loop, therefore, access to both fiber optic ends is required. The same limitations (described in Section 2.2.5) for spatial

resolution in BOTDR technique exist in BOTDA method. A 1 m spatial resolution in this method is obtained over a 30 km distance range through averaging signal for fewer than about 1000 times for the same efficiency as BOTDR.

2.2.4. DiTeSt™ and SMARTprofile™

The DBSs used for the present study is a BOTDA commercially known as DiTeSt™ manufactured by Omnisens SA. Table 2-1 gives the DiTeSt™ configuration used for all measurements.

Table 2-1. DiTeSt™ configuration used in the all measurements

Spatial resolution L_{SR}	Sampling interval L_{SI}	Distance resolution	Frequency resolution	Frequency scan range
0.5 m	0.1 m	0.1 m	1 MHz	10.2-11.1 GHz

A special fiber optic cable, called SMARTprofile™ made by Smartec, is used as the sensing cable. The SMARTprofile™ has two separate ε-T sensor pairs, S1-T1 and S2-T2. Strain sensors are directly embedded in the polyethylene (PE) thermoplastic jacket in a way that any external force on the jacket fully transfers to the fiber optic sensor. The temperature sensors are placed in a tube before embedding in the PE jacket to provide a strain-free condition, so they are only affected by ΔT, not $\Delta\varepsilon$.

2.2.5. Spatial resolution and strained length

The sensing system shows sensitivity to ΔT and $\Delta\varepsilon$ at any location along the sensing cable; however, the Brillouin frequency shift is measured at discrete points (sampling intervals - SI) spaced at a constant interval (L_{SI} - Table 2-1). The location of each discrete point along the cable, x_i, is a linear function of the sampling interval, L_{SI}, the number of points, n, and the coordinate of the first point, x_0. The measurement at each point is computed through averaging of frequency measurements at all sampling points over the spatial resolution. The spatial resolution, L_{SR}, of a DBS system is controlled by the pulse width and corresponds to a fiber length below which the strain is not registered with complete available accuracy (Glišić, Chen, & Hubbell, 2011). According to Table 2-1, L_{SR} = 50 cm includes five sampling points of L_{SI} = 10 cm.

Three different strained section lengths, l, relative to the spatial resolution, L_{SR}, are given as examples to better understand the relationship between the spatial resolution and the strained length. These scenarios are 1) $l > L_{SR}$, Figure 2-7a, 2) $L_{SR}/2 < l < L_{SR}$, Figure 2-7b, and 3) $l < L_{SR}/2$, Figure 2-7c. Three cases are possible in each scenario. Case 1 in all scenarios is encountered when the sampling point is in the strain-free section and located at least $L_{SR}/2$ away from the edges of the strained section. In this case no frequency change is registered at the sampling point. In Case 2 of all scenarios the sampling points are within $\pm L_{SR}/2$ m of the edge of the strained section and thus the spatial resolution window partially covers both the strain-free and the strained sections. Therefore it is expected that the Brillouin frequency shift change, $\Delta\nu_B$, will show a linear variation

over sampling points within this window, indicated as the sloped portion of the frequency response in Figure 2-7a and b. This linear trend would be proportional to the strained length ratio within $L_{SR,}$ discussed in more detail in Chapter 4.

For scenario 1, Case 3 corresponds to all sampling points that are within the strained section located at a distance at least $\pm L_{SR}/2$ away from the section ends. In other words, all the sampling points over the spatial resolution interval are strained, so that these points should register a $\Delta\nu_B$ which gives the closest strain to the applied strain, shown as the flat maximum frequency response in Figure 2-7a. In contrast to scenario 1, in Case 2 for the second scenario not all but the majority of the sampling points within the spatial resolution interval are strained, i.e. since the length covered by the spatial resolution is larger than the whole strained length a few points from the unstrained section also contribute to the frequency response. Accordingly, it is expected that the DBSs registers less of a frequency response over these points than the applied strain that is shown as the flat maximum section in Figure 2-7b. Scenario 3 is a special condition when none of the sampling points would register the $\Delta\nu_B$ (applied strain) regardless of the location of the points with respect to the strained section, because the number of sampling points over the strained section is fewer than half the points covered by the spatial resolution window.

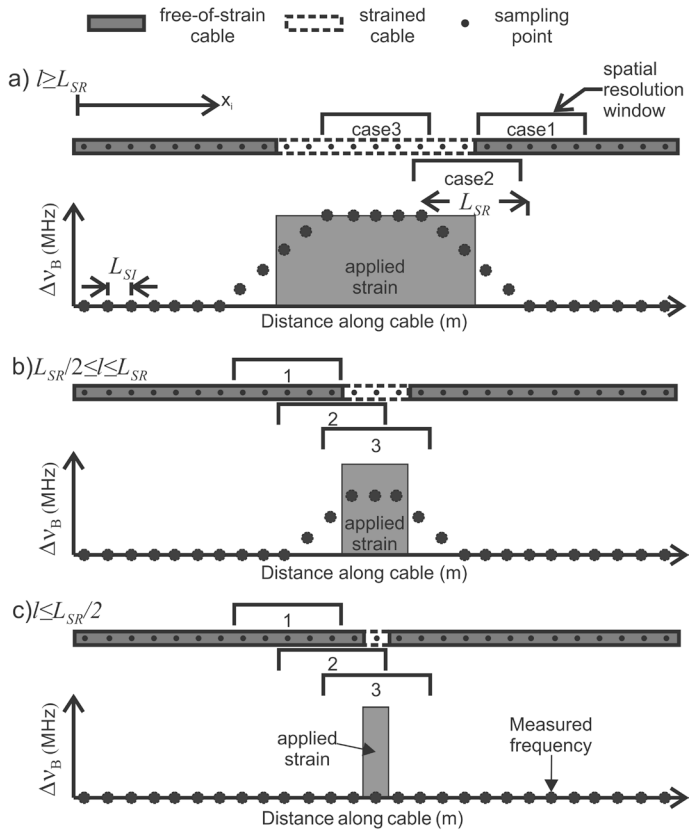

Figure 2-7 Effect of length of strained section, *l*, with respect to spatial resolution, L_{SR}; no frequency response is expected for $l \le L_{SR}/2$, linear variation of frequency change with strained length for $L_{SR}/2 < l < L_{SR}$, and frequency change is independent of the strained length for $l \ge L_{SR}$ (Madjdabadi, Valley, Dusseault, & Kaiser, 2016)

According to the conceptual representation of spatial resolution in Figure 2-7, Ohsaki et al. (Ohsaki, Tateda, & Omatsu, 2002) showed that the measured strain, ε_m, for a length shorter than L_{SR} can be linearly correlated with the applied strain, ε_a, through Eq. 2.4. However, as will be discussed in Chapter 4, the response of the DiTeSt™ for a strained length less than L_{SR} is different from what they concluded.

$$\varepsilon_m = l/L_{SR} \times \varepsilon_a \qquad for\, l \le L_{SR} \qquad (2.4)$$

The minimum available spatial resolution in DBS based devices is mostly limited to 1 m. the reason it cannot be shorter is that "*…if the pulse spans over a bandwidth larger than the Brillouin gain spectrum, the backscattered signal will show a broader spectral distribution given by the convolution of the natural Brillouin gain distribution with the pulse spectrum. This will smear out the backscattered signal over a wide spectral range and the measurement contrast vanishes. Since the natural Brillouin linewidth is given by the acoustic lifetime of about 10 ns, the activating pulse should not be shorter than this time, corresponding to a spatial resolution of 1 m*" (Luc Thévenaz, 2010).

2.3. Distributed Brillouin sensing technology applications

Distributed Brillouin sensing (DBS) systems were first used in the late 1980's to measure local attenuation in optical fibers (Horiguchi & Tateda, 1989). Since then, they have been used for monitoring in different applications including, but not limited to, electrical power lines (L Thévenaz, Facchini, Fellay, Nikles, & Robert, 2001), oil and gas pipelines (Daniele Inaudi & Glišić, 2006a), coiled tubing (Daniele Inaudi & Glišić, 2006b), concrete and steel bridges (Glišić et al., 2011; Glišić, Posenato, & Inaudi, 2007; He, Zhou, & Jinping, 2012), composite structures (Murayama & Kageyama, 2003), embankments and dams (Johansson & Watley, 2007), and landslide and slope stability assessment (Iten, Hauswirth, & Puzrin, 2011). They have also been applied to the monitoring of underground excavations including shallow tunnels (Hisham Mohamad, Bennett, Soga, Mair, et al., 2007) and underground mines (Naruse et al., 2007).

The following sections will provide a brief summary of non-geotechnical and geotechnical applications of the DBSs. These sections are categorized in two main classes of field and laboratory evaluations of these systems.

2.3.1. Laboratory cases

Experimental research using DBS systems has been reported in the field of energy and power. Optical fiber ground wires (OPGW), used in both earth and communication lines in electric power networks, are prone to damage because of exposure to lightning stroke and covering by ice. In an experimental study these two damaging factors were simulated while an OPGW was monitored using a BOTDR for both strain and temperature sensing (L. Lu et al., 2014). A scour monitoring system equipped with a BOTDA sensor was designed where a steel pipe buried in a water channel was tested with a heating belt closely run parallel to it (X.-F. Zhao, Li, Ba, & Ou, 2012). An outdoor experiment on a buried water tube along which controlled leakage occurred was monitored using a BOTDA for the early detection of oil and gas pipeline breaks and locations (D Inaudi,

Belli, & Walder, 2008). A BOTDA distributed sensor was integrated in a steel coiled tubing in order to develop a high-temperature, corrosion and fatigue resistant, intelligent system for electric drilling operations (Daniele Inaudi & Glišić, 2006b). In a large scale experiment, a 18 cm OD casing instrumented with a BOTDR was mechanically tested to evaluate the DBS technology performance and limits, the load transfer process, and the reliability of a downhole sensing system with an application of continuous monitoring of casing and completion mechanical deformation in depleting reservoir wells (Li, America, Parker, Farhadiroushan, & Blacklaw, 2004).

Among all structural materials, steel and concrete have vastly been the major focus of many experimental projects for studying the response of DBS systems for different engineering applications. In an outdoor experiment, a 7 m long steel beam loaded on half its length was monitored for a 24 hr period for performance evaluation of a BOTDA in temperature corrected strain measurement (X. Bao, Demerchant, Brown, & Bremner, 2001). In an experimental simulation of train movement, a 3.3 m long steel rail was equipped with a correlation enhanced BOTDA sensor to map the longitudinal strain distribution in the rails (Yoon, Song, Kim, & Kim, 2011). Steel pipe used in the oil and gas industry was tested under different loading conditions while the longitudinal and loop strain distribution of the outer surface of the pipe was monitored using a BOTDA for detection of localized pipe wall buckling (Zou, Bao, Ravet, & Chen, 2006)

Numerous laboratory-scale trials have been accomplished using these novel sensors, i.e. DBS, to evaluate their performance in measurement of deformation under different loading conditions in comparison with more conventional sensors as well as their capability to detect any induced damage in different materials.

A square aluminum tube was loaded in a two-point flexural configuration with a BOTDR for verifying the compressive and tensile response of the beam (Kim, Lee, & Kwon, 2002). In a similar study, two superimposed steel beams were tested in a flexural configuration for evaluation of a BOTDA in identifying any defect in the bending beams (Bernini et al., 2006). In a novel application, steel rebars in a number of reinforced concrete specimens equipped with three differently embedded distributed sensors were monitored using a BOTDA for deformation induced by corrosion expansion (X. Zhao et al., 2011). A 3 m long steel beam was statically loaded as its deformation distribution at two different temperatures was monitored using a BOTDA with the purpose of crack detection and long-term performance of steel bridge girders (Mufti, Thomson, Inaudi, Vogel, & McMahon, 2011)

Steel strands equipped with fiber optic sensors embedded in a number of pre-stressed concrete beams were pull-out tested while pre-stress loss was monitored with a BOTDA (Lan, Zhou, & Ou, 2014). Strain developed in reinforcing elements during bending test of concrete beams was measured using a BOTDA (Zeng et al., 2002). Similarly, a reinforced concrete slab was monitored with a BOTDA during bending loading for tensile and compressive strain measurement (Martín-Pérez et al., 2010). A concrete column reinforced with fiber reinforced fiber (FRP) rods and sheets was monitored with circumferentially laid-out distributed BOTDA sensor along its height while it was pulled or pushed to the sides for locating FRP-concrete debonding points and induced cracks

(X. Y. Bao, Ravet, & Zou, 2005). A 38 cm long corrugated mortar specimen instrumented with a new BOTDA based distributed sensor was tested for evaluation of autogenous shrinkage and cracking processes in mortar (Y. Bao, Meng, Chen, Chen, & Khayat, 2015).

A small-scale laboratory test, in which a soil slope model was monitored with a BOTDR, was performed to study the feasibility of this technique for early-warning detection of any movement when the sensor was integrated into the soil (B. Wang, Li, Shi, & Wei, 2008). A large-scale laboratory experiment was done during which two artificial sinkholes embedded underneath a soil layer were formed to evaluate a BOTDR sensor performance used as an early cavity detection and sinkhole warning system in railway tunnels (Lanticq et al., 2009). In another similar large-scale experiment, a shallow horizontally laid-out distributed sensor in a soil trench along with sensors vertically embedded within mini-piles were tested for studying the performance of a BOTDR system to provide a smart underground security fence in detection of excavation of smuggling tunnels (Assaf Klar & Linker, 2010).

A physical model of a mining panel, developed to study the feasibility of backfilling during mining work, was diagonally extracted in two steps followed by backfilling while deformational behaviour of the model was monitored using a BOTDR based senor embedded in the body of the model above the roof and on the surface (Nan & Gao, 2011). In a series of experiments, beams made of concrete, wood, and aluminum were bent over a wood arch with a BOTDA distributed sensor surface attached using four different methods for assessment of a future underground mining displacement monitoring application (Noni, MacLaughlin, & Wang, 2011). A 5 m long PVC sensor tube was tested under different horizontal and vertical displacement scenarios while it was monitored using a BOTDR based sensor attached along four lines of pipe surface separated 90° from one another for evaluating the DBS performance in capturing in-plane and out-of-plane tube bending with an application in underground mine tunnel wall displacement monitoring (Moffat, Sotomayor, & Beltrán, 2015).

2.3.2. Field studies

Although most of the literature reported on the use of DBS systems is laboratory research work, since it is under ongoing development, there are several field trials in different engineering contexts. They have even been applied in an innovative solution for increasing the perimeter security of critical infrastructures where a BOTDA based sensor was integrated into several fences (P. Ferdinand et al., 2012).

Energy and power sections of industry have benefited from distributed sensing technology. Seabed embedded power transmission lines and gas pipelines instrumented with BOTDA based distributed sensors were monitored in terms of both temperature and strain for ensuring the integrity of these infrastructures, improving the construction validation, and detection of possible leaks in different oil and gas projects (Rochat & Nikles, 2012).

DBS systems have been applied for structural health monitoring of various civil engineering structures including railways, bridges, piles, dams, and tunnels. A 60 m long section of a railway

was monitored using a BOTDA for demonstration of the technology potentials in providing information about train identification, axle counting, speed detection, and dynamic load calculation (Minardo, Porcaro, Giannetta, Bernini, & Zeni, 2013). A 300 m long section of FRP reinforced concrete pavement of a highway was monitored with an integrated polarization-dependent BOTDA sensor for distributed impact waves resulting from highway traffic (X. Bao et al., 2008).

Structural damage induced by a destructive test on a concrete bridge was monitored with a BOTDR (W. Zhang, Shi, Zhang, Liu, & Zhu, 2007). In a field trial, a bridge during construction was instrumented with two different optical sensing methods; one long-gauge FBG spectrometry and the other BOTDA embedded in the concrete for comparison of their performance in temperature and strain measurements (Glišić et al., 2011). In a similar study, deformation measurement of a supporting beam of a road bridge with a span length of 44.4 m during a load test was performed using a BOTDA (Minardo, Bernini, Amato, & Zeni, 2012). Two small concrete bridges were monitored using two different sensing element packaging based on BOTDR for static load measurement and strain localization induced by crack formation (Bastianini, Rizzo, Galati, Deza, & Nanni, 2005). Many more examples can be found in the literature for bridge monitoring, whether steel or concrete, as partly summarized in Table 2-2.

Landslide monitoring using DBS technologies has also shown great success in several field trials. A road section suspected of having slope movement was selected for a monitoring campaign in which a pair of BOTDR based sensors was installed in two boreholes on the road and backfilled with a grout mix for locating the active shear plane within the soil slope (Momand, 2010). A BOTDR based sensor attached to a lock-block retaining wall was used to monitor a deforming mass as a part of monitoring campaign for better understanding and managing the Ripley Slide (Huntley et al., 2014). A road-, soil-, and borehole-embedded BOTDA based distributed sensor was used for evaluation of differential soil displacement because of a creeping landslide, determination of its boundary extension on the surface and sliding surfaces, and detection of the transition zone between the stable ground and moving area (Iten, 2011). A network of BOTDR based distributed sensors was implemented on a highway slope where the in-depth and surficial rock and soil deformation pattern, axial strain distribution along anchors and inclinometers were monitored (B Shi, SUI, LIU, & ZHANG, 2006).

A geotextile integrated distributed sensor based on BOTDA has been field tested for soil displacement monitoring and dike protection in rivers and gravity dams (Krebber et al., 2010). Similarly, a BOTDR based instrumented geotextile has been tested for evaluation of its performance in a railway embankment (Liehr et al., 2008). A 8 m long hollow ground anchor equipped with a distributed sensor working based on SBS was designed and installed as a smart wall support for an excavation pit and pull-out tested (Iten, 2011).

BOTDR instrumented mini-piles were placed around existing piles for foundation improvement. Furthermore, similar mini-piles reinforced with steel bars equipped with pre-strained BOTDR based sensors were installed close to a future tunnel excavation for the purpose

of integrity monitoring of piles (A Klar et al., 2006). A 750 m long section of one of two 1150 m long parallel tunnels with a maximum depth of 13 m was instrumented with a BOTDR based distributed sensor attached to the surface of the concrete arch for measurement of the general deformation pattern of the tunnel (such as uneven subsidence) and also of localized deformation of the concrete arch resulting from crack formation (Bin Shi et al., 2003). In a study of excavation induced deformation of two shallow tunnels with a minimum clear separation of 2.3 m, the circumferential strain distribution of concrete liners of one of the tunnels with the more advanced face was monitored with a BOTDR while the other tunnel was excavated with a TBM (Hisham Mohamad, Bennett, Soga, Mair, et al., 2007). One of the forepoling steel pipes used for pre-strengthening of the soil mass around a tunnel was monitored using a BOTDA before, during, and after excavation in order to measure ground deformation and settlement for later refinement of design and operational parameters (Guzik, Yokoyama, Matsuda, & Kishida, 2013).

In an underground laboratory intermediate scale experiment, a 30×30×15 m^3 volume of drained fractured rock mass was drilled by a horizontal borehole through a contained fault, then sealed and fluid injected while a surface mounted BOTDA distributed sensor monitored spatial distribution of localized deformation at the fracture locations for application in studying complex hydromechanical response of the rockmass during high and low frequency loading and unloading loops (Cappa, Guglielmi, Gaffet, Lançon, & Lamarque, 2006). A BOTDR based distributed sensor used in an underground mine to study mine state specifically deformation variations while mining activities at different levels was in progress when [54] was published. The instrumentation level was at the ventilation tunnel where the deformation of 200 m of the ceiling and sidewalls of the tunnel was monitored using pin-attached sensors to the rock mass (Naruse et al., 2007). In a similar study, the strain tubes (STs), explained earlier in Section 2.3.2, were tried in an underground mine for displacement monitoring of sidewalls and roof of a tunnel (Moffat et al., 2015). The STs were attached to the rock mass at four points along the tube length located at the undercut level of the mine.

Table 2-2 provides a brief summary of the aforementioned DBS applications in two laboratory and field scales.

Table 2-2. Summary of DBS systems used in different engineering contexts

Trail scale	DBS technique	L_{SR} (m)	Measured quantity	Application	Ref.
Laboratory	BOTDR	2	Strain, temperature	Electric power line health monitoring	(L. Lu et al., 2014)
	BOTDA	1	Temperature	Scour monitoring system for ensuring the heating power line for subsea buried pipelines	(X.-F. Zhao et al., 2012)
	BOTDA	1	Strain	Strain distribution monitoring along soil-buried energy pipelines subjected to permanent shear displacement due to earthquake-induced ground movement	(Glišić & Yao, 2012)

Table 2-2 (cont.). Summary of DBS systems used in different engineering contexts

	BOTDA	0.15	Strain	Detection of localized energy pipe wall buckling	(Zou et al., 2006)
	BOTDA	0.13	Strain	Structural degradation (wall-thinning) of steel pipes	(Zou et al., 2004)
	BOTDA	1	Strain, temperature	Temperature, corrosion, and fatigue monitoring of steel coil tubing used in electric drilling techniques	(Daniele Inaudi & Glišić, 2006b)
	BOTDR	1	Strain, temperature	Continuous monitoring system for casing and completion deformation in intelligent wells	(Li et al., 2004)
	BOTDA	0.1	Strain	Early detection of crack formation and location in ceramic surfaces	(Zou & Feng, 2008)
	BOTDR	3	Strain	Aluminum alloy beam deflection	(Kim et al., 2002)
	BOCDA	0.04	Strain	Longitudinal strain distribution of steel rails	(Yoon et al., 2011)
	BOTDA	1	Strain	Defect detection in steel beam bending	(Bernini et al., 2006)
	BOTDA	0.07	Strain	Crack detection in steel beams	(Chen, Shen, & Shin, 2011)
	BOTDA	0.5	Strain, temperature	Temperature corrected strain measurement of a steel beam under a complicated loading condition	(X. Bao et al., 2001)
	BOTDR	1	Strain	Efficiency evaluation of a novel fibre reinforced polymer (FRP) sheet used for enhancement of a full-scale pre-stressed concrete girder	(Z. Wu, Xu, Hayashi, & Machida, 2006)
	BOTDA	0.1	Strain, temperature	Crack deformation and long-term performance of steel girders in bridges	(Mufti et al., 2011)
	BOTDA	1	Strain	Steel corrosion expansion induced detection and its deformation measurement in reinforced concrete structures	(X. Zhao et al., 2011)
	BOTDA	1	Strain	Pre-stress loss control in pre-stressed concrete beam	(Lan et al., 2014)
	BOTDA	0.5	Strain	Strain measurement developed in reinforcing elements in concrete beams	(Zeng et al., 2002)
	BOTDA	0.2	Strain	Tensile and compressive strain measurement in reinforced concrete slab	(Martín-Pérez et al., 2010)
	BOCDA	0.04	Strain	Crack identification in a pre-notched concrete specimen	(Imai & Feng, 2012)
	BOTDA	0.15	Strain	Crack detection in reinforced concrete beam under bending loading	(Deif et al., 2010)
	BOTDA	0.15	Strain	Locating FRP concrete debonding point and induced cracks during a FRP reinforced concrete column laterally loaded	(X. Y. Bao et al., 2005)
	BOTDA	1	Strain, temperature	Monitoring behaviour of concrete structures at different construction stages for hydration process, cyclic and torsional loading	(Yehia, Landolsi, Hassan, & Hallal, 2014)
	BOTDA	-	Strain, temperature	Shrinkage and cracking evolution in mortar specimen	(Y. Bao et al., 2015)
	BOTDR	1	Strain	Capability of a DBS system for an early-warning monitoring system in soil slope movement	(B. Wang et al., 2008)

Table 2-2 (cont.). Summary of DBS systems used in different engineering contexts

	BOTDR	1	Strain	Soil cavity detection and sinkhole warning in railway tunnels	(Lanticq et al., 2009)
	BOTDR	-	Strain	Underground mine tunnel sidewall and ceiling displacement monitoring using a smart PVC tube equipped with distributed sensors	(Moffat et al., 2015)
	BOTDR	1	Strain	Smuggling tunneling induced displacement monitoring for enhancing border security	(Assaf Klar & Linker, 2010)
	BOTDA	-	Strain	Performance evaluation of different surface attachment methods of distributed sensors to beams for underground mining displacement monitoring application	(Noni et al., 2011)
	BOTDR	1	Strain	Monitoring deformation pattern of a mining panel during stope excavation and backfilling	(Nan & Gao, 2011)
Field	BOTDA	3-5	Strain, temperature	Integrity monitoring and leak, hot spot, and break detection in power line and pipelines	(Rochat & Nikles, 2012)
	BOTDA	1	Strain, temperature	Temperature, corrosion, and fatigue monitoring of steel coil tubing used in electric drilling techniques	(Daniele Inaudi & Glišić, 2006b)
	BOTDR	-	Strain	Longitudinal strain distribution in shallow soil buried pipeline affected by underneath tunnelling operations	(Vorster et al., 2006)
	BOTDA	1	Strain	Enhancing the security of important infrastructure using a smart fence	(P. Ferdinand et al., 2012)
	BOTDA	2	Impact wave	Reinforced concrete pavement monitoring for impact wave due to highway traffic	(X. Bao et al., 2008)
	BOTDA	1	Strain	Railway monitoring for retrieving information about train traffic	(Minardo et al., 2013)
	BOTDA	0.03	Strain	Railway soil embankment health monitoring system	(Liehr et al., 2008)
	BOTDA	-	Strain, temperature	Bridge construction	(Glišić et al., 2011)
	BOTDR	1	Strain	Bridge damage identification	(W. Zhang et al., 2007)
	BOTDA	1	Strain, temperature	Crack deformation and long-term performance of steel girders in bridges	(Enckell, Glišić, Myrvoll, & Bergstrand, 2011)
	BOTDA	3	Strain	Deformation measurement during bridge supporting beam load test	(Minardo et al., 2012)
	BOTDR	-	Strain, temperature	Static load measurement and strain localization due to crack formation in small concrete bridges	(Bastianini et al., 2005)
	BOTDA	0.5	Strain	Long-term structural integrity monitoring of a civil defence infrastructure	(He, Wu, & Zhou, 2007)
	BOTDR	1	Strain	Borehole inclinometer casing monitoring for locating the potential sliding surface of a landslide, surface and in-depth movement of a dam	(R Hoepffner, Singer, Thuro, & Aufleger, 2008)
	BOFDA	0.1	Strain	Soil displacement and dike protection using an intelligent system based on geotextiles for dam and river integrity applications	(Krebber et al., 2010)

Table 2-2 (cont.). Summary of DBS systems used in different engineering contexts

	BOTDR	-	Strain	Understanding deformational behaviour of Ripley Slide	(Huntley et al., 2014)
	BOTDR	0.3	Strain	Slope movement monitoring for shear plane detection	(Momand, 2010)
	BOTDR	-	Strain	Slope mass and support strain and movement monitoring	(B Shi et al., 2006)
	BOTDA	1	Strain	Determination of landslide boundary on the surface and below the ground Smart DBS integrated ground anchor for excavation wall support	(Iten, 2011)
	BOTDR	-	Strain	Strain distribution along a secant pile wall near an in-progress construction site	(Hisham Mohamad, Bennett, Soga, Klar, & Pellow, 2007)
	BOTDR	1	Strain	Axial and bending strain distribution along a precast pile while driven into the soil	(Y. Lu, Shi, Wei, Chen, & Zhang, 2012)
	BOTDR	1	Strain	Foundation improvement and pile integrity monitoring	(A Klar et al., 2006)
	BOTDR	1	Strain	Monitoring of shallow tunnel deformation field and of strain localization due to induced cracks	(Bin Shi et al., 2003)
	BOTDR	1	Strain	Joint movement monitoring of concrete tunnel lining	(Soga et al., 2010)
	BOTDA	-	Strain	Measurement of spatial distribution of deformation field for hydromechanical behaviour of rock masses	(Cappa et al., 2006)
	BOTDR	1	Strain	Monitoring of excavation-induced strain of a twin tunnel	(Hisham Mohamad, Bennett, Soga, Mair, et al., 2007)
	BOTDA	0.1	Strain	Ground settlement measurement due to tunnel excavation	(Guzik et al., 2013)
	BOTDR	1	Strain	Deformation profile and crack detection in an old masonry tunnel lining induced by a new ongoing tunnel excavation beneath it	(H. Mohamad, Bennett, Soga, Mair, & Bowers, 2010)
	BOTDR	1	Strain	Deformation evolution in ventilation tunnel during an upper-hand mining operation	(Naruse et al., 2007)
	BOTDR	-	Strain	Underground mine tunnel sidewall and ceiling displacement monitoring using a smart PVC tube equipped with distributed sensors	(Moffat et al., 2015)

All presented case studies during last two sections were meant either to examine the performance of a commercially available distributed sensor for strain measurements in the laboratory or the applicability and capability of such systems for field measurement. Therefore, in each study, measurements had been designed to answer a specific question. In this sense, all cases were different, although there were similarities among the cases.

For this research, we also had a question and the experimental studies were designed accordingly to address this question. Therefore, this study was quite different from all those studies presented in Table 2-2. The only common issue among all those cases with this research was the linear relation between Brillouin frequency shift change and applied strain. However, this research studied spatial and sequential distribution of strained events along the sensor, as well as sensor embedment methods in mortar beams while each beam was cracked at different locations, and eventually the sensor response when it was under shear displacement. None of the aforementioned tests have ever been done in the laboratory. In conclusion, all the results presented in coming chapters are novel and specific.

3. Primary evaluation of a distributed Brillouin sensing system

3.1. Introduction

Microseismic events are common in deep underground mining as the rock mass responds to excavation operations. Such events are typically located close to excavation boundaries, but there have been large seismic events distant from mined-out regions, particularly as the extraction ratio increases (Kaiser et al., 2005). Apart from near-field events that are known as stress-induced events, distant events cannot easily be explained by elastic field stress changes; deformation field variations caused by gravity-driven rock block movements may be a better way of explaining these events. Hence, to understand rock mass behaviour around a mine, more distant deformations must be measured, and in this regard, distributed optical fiber sensors (DOFSs) may help understanding and modeling of three-dimensional load transfer mechanisms and rock mass response.

If a DBSs is to be installed in a deep underground mine to monitor the remote deformation field, proper characterisation of the sensing system performance and limitations before field installation is necessary. This chapter presents results from an experimental test program on the response of a DBSs, including longitudinal extension, lateral displacement, and measurements on unstrained cable for noise level assessment.

This chapter was mainly extracted from the published paper in Measurement journal with the following citation:

Madjdabadi B, Valley B, Dusseault MB, Kaiser PK. Experimental evaluation of a distributed Brillouin sensing system for measuring extensional and shear deformation in rock. Measurement 2016;77:54–66. doi:10.1016/j.measurement.2015.08.040

3.2. Strain-free response of SMARTprofile™

As a first step, a 30 m long section of SMARTprofile™ cable is interrogated by the DiTeSt™ during almost 14 hours resulting in 422 ν_B measurement profiles along the cable while ΔT and $\Delta\varepsilon$ were zero. This is to quantify the noise level of the system below which any ΔT or $\Delta\varepsilon$ at any location along the cable cannot be discriminated from an unchanged section because of the presence of noise. This also allows quantification of the repeatability of the measurements and identification of eventual measurement drift, if any. The sensing cable configuration including the connection sequence of the sensors and DiTeSt™ is shown in Figure 3-1. (ΔT during all tests presented in this chapter was constant.)

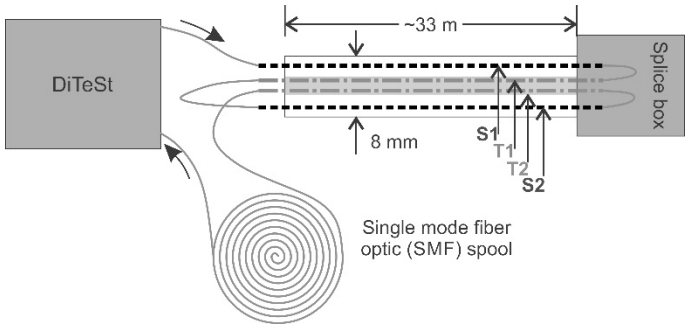

Figure 3-1 DiTeSt™ and SMARTprofile™ connection status for the unstrained cable testing. There are two strain (S1-S2) and two temperature (T1-T2) sensors embedded in the SMARTprofile™.

3.2.1. Frequency spatial offset issues

Figure 3-2 shows Brillouin frequency shift in GHz along the ε and T sensors length for all measurements before referencing with respect to the first measurement. Generally, there is a clear difference between ν_B registered at the strain and temperature sensors because of the different embedment conditions of the sensors (Section 2.2.4). Also, being embedded in the PE jacket causes larger fluctuations in frequency measurements along the strain sensors than along the temperature sensors.

As stated in Section 2.2.3, variation in the Brillouin frequency shift is the parameter of interest to compute, thus all measurements must be referenced to the first measurement, i.e. the first measurement values are subtracted from all subsequent measurements in order to show changes. However, there are a number of outlier measurements where the DiTeSt™ registered completely wrong profiles along the entire cable which should be cleaned from the data before referencing. These outliers occurred along both strain and temperature sensors as well as connection fibers, although they are largely found as fluctuations in the strain sensors. These outliers mostly occurred when the system crashed for reasons such as extended runtime. These outliers are suppressed using a robust processing algorithm based on interquartile range (IQR) analysis (Posenato, Kripakaran, Inaudi, & Smith, 2010).

In addition, it is noted that some measurements are offset relative to others along the horizontal axis. This offset is a location misalignment that occurs over the entire cable but it is more noticeable at the strain sensors, especially where there is a large difference in the Brillouin frequency shift, e.g. at the location where strain and temperature sensors meet (Figure 3-2b). A probable reason for this misalignment is thought to be the 10 cm distance resolution of the system. This resolution is the ability of the system to detect the sampling point at its correct location along the cable so that a measurement at a point might be located either at its real position or within ±10 cm.

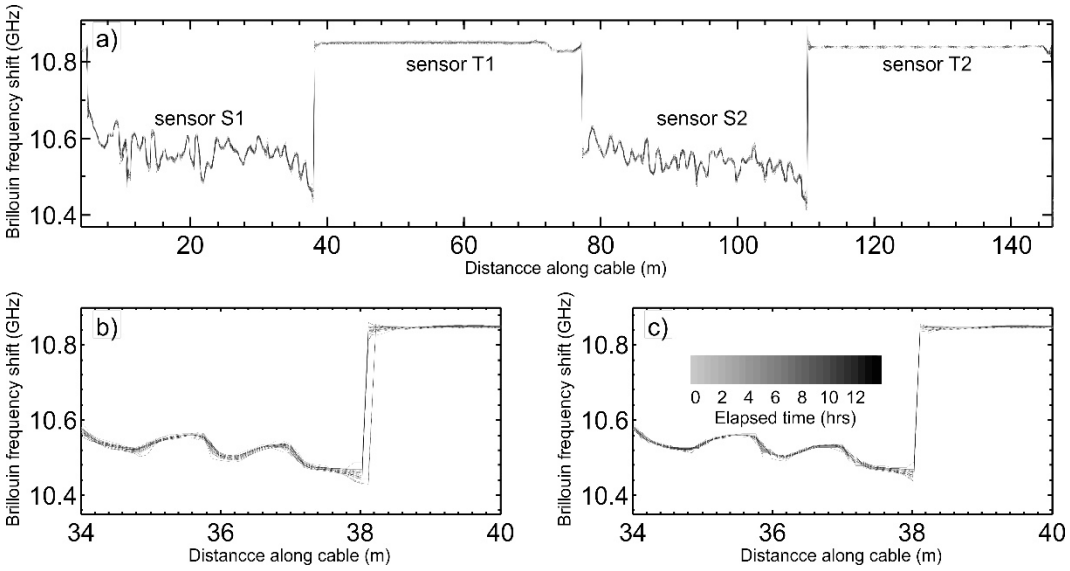

Figure 3-2 a) Over 400 registered Brillouin frequency shift profiles for strain sensors, b) magnified view of the profile where S1 meets T1 showing a clear offset along the length, c) the same profile shown in (b) after removing the offset issue

This issue along the sensing cable affects data referencing. An attempt was made to locally realign the measurements using a simple comparative algorithm based on the assumption that misalignment never exceeds one 10 cm distance sampling interval. As shown in Figure 3-3, three frequency changes between the initial reading (j=1) and subsequent readings (j>1) for a point i and points before (i-1) and after (i+1) are considered and compared: $\Delta\nu_i = \nu_{i,j} - \nu_{i,1}$, $\Delta\nu_{i-1} = \nu_{i-1,j} - \nu_{i,1}$ and $\Delta\nu_{i+1} = \nu_{i+1,j} - \nu_{i,1}$. The smallest value of these three differences is considered as the more reliable, and the frequency shift readings are corrected accordingly: if $\Delta\nu_i$ is the smallest (Figure 3-3a), $\nu_{i,j}$ is kept unchanged. If $\Delta\nu_{i-1}$ or $\Delta\nu_{i+1}$ are the smallest (Figure 3-3b & c) then $\nu_{i,j} = \nu_{i-1,j}$ or $\nu_{i,j} = \nu_{i+1,j}$, respectively.

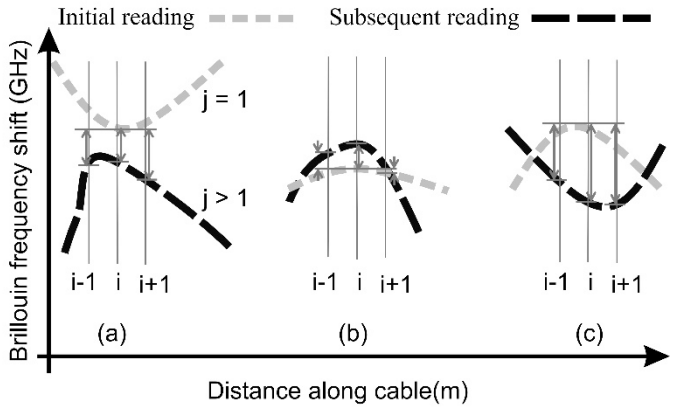

Figure 3-3 Simple representation of the algorithm developed for reducing the spatial offset issue. Refer to text for a, b, and c.

Figure 3-2c shows the corrected original Brillouin frequencies after application of this algorithm; previously offset measurements are now aligned at their appropriate locations, resulting

in better accuracy for later data analysis. It should be noted that this method has facilitated discrimination between unstrained sections and locally strained sections; therefore, it will not remove the real strain as an outlier.

3.2.2. Base noise level

The Brillouin frequency shifts are now corrected for outliers and misalignment issues. Referencing all measurements with the first measurement provides the relative Brillouin frequency shift, as shown in Figure 3-4 for sensor S1, which brings ν_B data at each sampling point to almost zero. However, the $\Delta\nu_B$ data show fluctuations at all locations along the cable, so any small external ΔT or $\Delta\varepsilon$ in the cable would be masked if smaller than the noise level. In other words, the minimum physical change (ΔT, $\Delta\varepsilon$) applied to the cable must be above the noise level of the frequency profile in order to be detected as an anomaly along the cable.

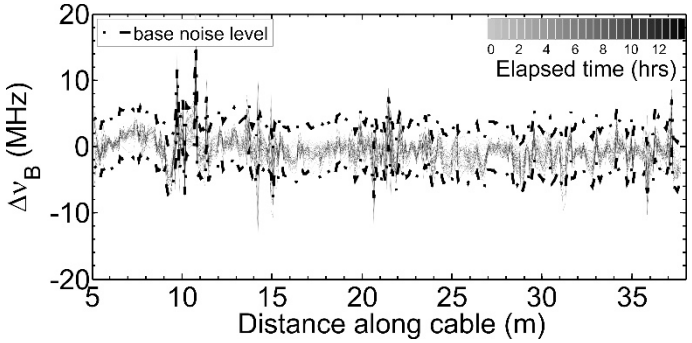

Figure 3-4 Base noise interval of the processed Brillouin frequency shift change for sensor S1 to constrain the base noise level of the DiTeSt™

From Figure 3-4 it is noted that the frequency fluctuation at each point along the cable is different. Furthermore, because of the manufacturing process of the SMARTprofile™ cables, each shows dissimilar fluctuations at a particular point (distance along cable), so it is not possible to have the same standard deviation for a single point, e.g. at 5 m distance, for two different cables. Each point for every cable has its own standard deviation (SD), different from other points along the cables. Although it is possible to obtain such a noise level SD at each individual point, it might be time consuming. Rather a computed noise level based on the data recorded in this test can be used as an indicator of expected noise level for all SMARTprofile™ cables.

A simple statistical analysis was performed on the $\Delta\nu_B$ data at every point along cable (S1, S2, T1, and T2) in order to find the base noise level. Three standard deviations (3×SD) for all points were stored in a matrix as a random variable. Then, the average of 3×SDs for all points along the cable was used to find a single, best 3×SD for the entire cable, giving upper and lower bounds for the noise level, as shown with black dashed lines in Figure 3-4, where this 3×SD was added to and subtracted from the mean of the $\Delta\nu_B$ at each point, respectively.

The noise levels are summarized in Table 3-1 for all sensors. The correlation factors applied to $\Delta\nu_B$ to obtain $\Delta\varepsilon$ and ΔT are recommended by the DiTeSt™ manufacturer as 0.05055 MHz/με and

1.15 MHz/°C for ε and T sensors, respectively. It can be seen that strain variations due to noise are constrained to less than 160 με (~±77 με).

Table 3-1 Base accuracy summary of the sensing cable

Sensors		Strain sensors			Temperature sensors		
		S1	S2	Avg.	T1	T2	Avg.
Mean of 3×SDs	Units						
	MHz	±3.6	±4.2	±3.9	±3.2	±2.9	±3.0
	με or °C	±71.3	±82.4	±76.9	±2.7	±2.5	±2.6

3.3. Extensional Test

In this section the DiTeSt™ response was evaluated when the sensing cable was longitudinally stretched (at constant *T*). The test was executed for different strained lengths, *l*, from 100 cm down to 1 cm. Displacement was applied to each strained length with 0.1 mm increments in order to induce a maximum 5000 με at the final step. Figure 3-5 shows the test set-up and how the SMARTprofile™ cable was clamped and strained. Each clamp was an small aluminum block (1.5 cm wide, 5 cm long) containing a slot of dimension just under the cable cross-sectional area (4×8 mm) to ensure a good grip on the cable, as schematically shown in Figure 3-5.

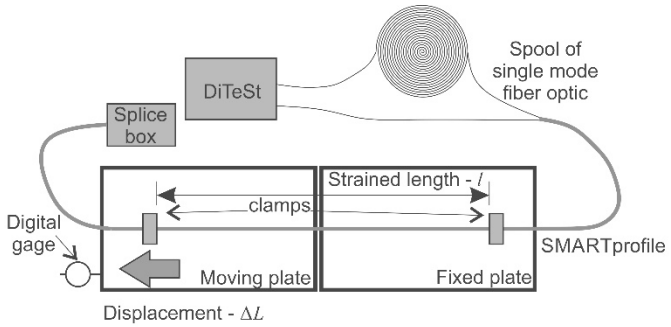

Figure 3-5 SMARTprofile™ is clamped at both ends of the strained length, *l*, one on the fixed plate and the other on the moving plate.

3.3.1. Linear Correlation

Figure 3-6a plots the relative Brillouin frequency shift change against distance along cable for all strained lengths, *l*, at the final displacement step, an applied 5000 με. A clear response was observed for all strained lengths above 25 cm, which is equal to half the spatial resolution, L_{SR}. For $l < L_{SR} = 50$ cm, it is expected from Section 2.2.5 that the frequency change response should be less than the applied microstrain. However, this effect was not observed and the $\Delta\nu_B$ for $l = 40$ and 30 cm was similar to that for $l \geq 50$ cm. However, it sometimes happened that the system could not detect any changes in the frequency profile for the 30 cm strained length.

On the other hand, no systematic $\Delta\nu_B$ is evident in Figure 3-6a for all $l < 0.5 \times L_{SR}$, i.e. $l < 25$ cm, as explained in Section 2.2.5 and as confirmed by Glišić *et al*. (Glišić et al., 2011). Actually, an irregular response is observed; for example, for a 20 cm length $\Delta\nu_B$ initially increased slightly to less than 20 MHz for 0.6 mm tensioning followed by a drop with an increase in applied strain,

Figure 3-6c. Both of these issues are better understood in terms of the Brillouin gain spectrum, as discussed in Section 3.3.3.

As stated earlier, $\Delta\varepsilon$ and Brillouin frequency shift change are highly correlated. Figure 3-6b plots $\Delta\nu_B$ at the middle of each strained section, indicated by the vertical dashed rectangle, versus the applied microstrain. The solid line represents the manufacturer's recommended correlation coefficient, i.e. C_ε=0.05055 MHz/με; however, it tends to overestimate the measured $\Delta\nu_B$, particularly at high strains. Consequently, using all $\Delta\nu_B$ values for all strained lengths above $L_{SR}/2$, a new best-fit correlation was obtained as C_ε=0.04607 MHz/με, the black dashed line in Figure 3-6b, along with its 95% confidence interval, the light grey dashed lines.

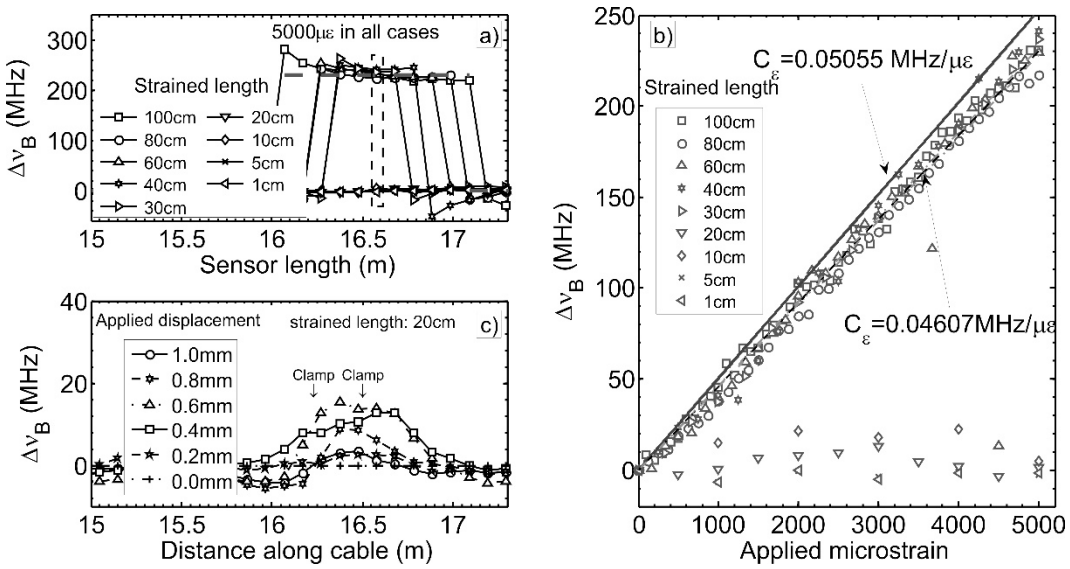

Figure 3-6 a) $\Delta\nu_B$ for application of 5000 με to various strained lengths b) best-fit correlation between applied strain and $\Delta\nu_B$ c) typical $\Delta\nu_B$ response applying incremental displacement to a 20 cm clamped length

3.3.2. Time-dependent behaviour

In addition to tests described in Section 3.3.1, a 60 cm length of the cable was strained under 3 mm displacement over 15 hrs to assess time-dependent behaviour. Figure 3-7a and b show the $\Delta\nu_B$ data against distance along cable and for the mid-point of the strained section. Measurements were quite repeatable during the straining period; they were confined within three standard deviation intervals of $\Delta\nu_B$ of only ±3.8 MHz, which is also consistent with the base noise level in the Section 3.2.2. This implies that the sensor in the strained section behaved independent of the time under strain, but this result contrasts with results from Valley et al. (Valley, M. Madjdabadi, Kaiser, & Dusseault, 2012) where a constant dead load was used for stretching the cable and induced time-dependent behaviour of $\Delta\nu_B$ over the test period. In this case a constant load boundary condition induced creep of the polyethylene cable, but in our case, with a constant displacement boundary condition, measurements are satisfactorily stable with time.

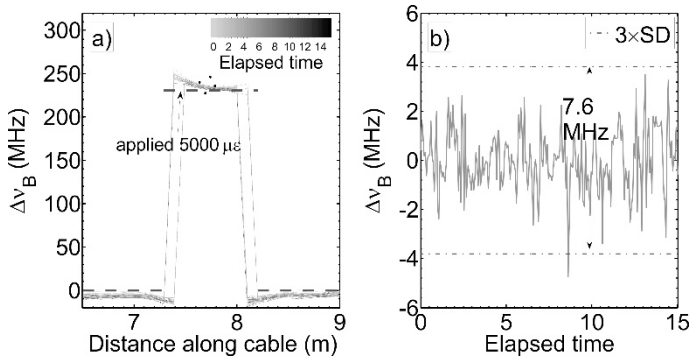

Figure 3-7 a) $\Delta\nu_B$ for application of 5000 με to a 60 cm strained length over 15 hrs, b) $\Delta\nu_B$ for the mid-point of the strained length over time

3.3.3. Short-length events

Section 3.3.1 showed that the frequency response over a strained length shorter than half the spatial resolution, $L_{SR}/2$, would not be detected by the system. Furthermore, the Brillouin frequency shift often shows a trough at points behind the clamps (Figure 3-7a). Such behavior is better understood when considering the Brillouin gain spectrum, BGS (Figure 2-6), as they can be attributed to the process of gain peak detection for strained lengths shorter than half the spatial resolution, hereafter called short-length events.

Figure 3-8 shows the $\Delta\nu_B$ profile against distance along cable where a 50 cm length was stretched by 0.5 and 2.5 mm inducing 1000 με and 5000 με, respectively. Six points, denoted by 1 to 6, were considered for more detailed study of their BG spectra. At each sampling point the spatial resolution window covers $\pm L_{SR}/2$ before and after the point, therefore the spatial resolution window at points 1 and 6 was completely located within and outside the strained section, respectively. During two applied displacement steps, especially at higher displacements, the largest difference was observed between points 3 and 4, which were located just before and behind the right clamp, respectively. At the low displacement of 0.5 mm, a frequency change of almost 21 MHz was registered at point 4, similar to 31 MHz read for the point 3. However, at the higher displacement of 2.5 mm, the measured frequency change dropped to about 7 MHz for point 4, a significant difference with the 219 MHz registered at point 3 at the same step. This difference in the frequency of these two points at low and high displacements resulted from the curve fitting procedure of the system to the gain spectrum at each point, discussed below.

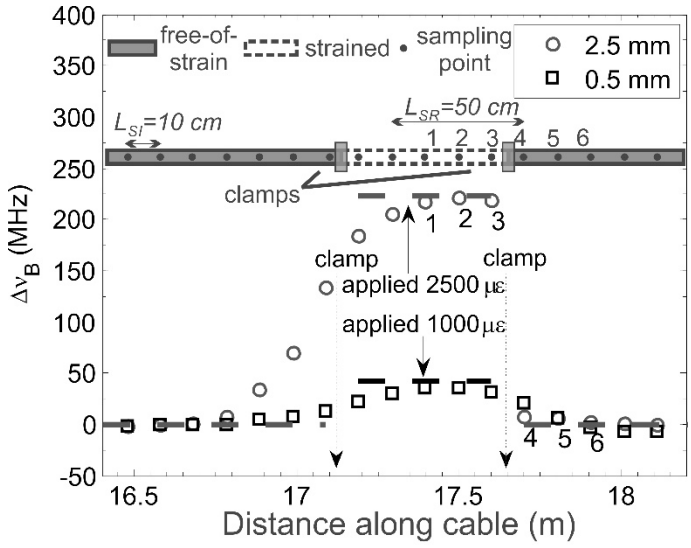

Figure 3-8 Two different strain levels applied to a 50 cm strained length of SMARTprofile™; $\Delta\nu_B$ at six points 1-6 was considered for their different behavior at registration of Brllouin frequency at these two strain levels through study of Brillouin gain spectra in Figure 3-9.

Brillouin gain spectrum is described by three components; the Brillouin frequency shift, ν_B, the full width at half maximum, *FWHM*, and the peak gain, g_B, i.e. Brillouin scattering coefficient (Figure 2-5). When a uniform strain is applied along cable, the gain spectrum can be obtained using a Lorentzian fit based on Eq. 3.1 (Murayama, Kageyama, Naruse, & Shimada, 2004).

$$g(\nu_B) = (FWHM/2)^2 \, g_B \Big/ \left((FWHM/2)^2 + (\nu - \nu_B)^2 \right) \qquad (3.1)$$

Figure 3-9 shows the gain spectrum, various shaped dots, for the four sampling points indicated in Figure 3-8 as points 1, 3, 4, and 6 for the two displacement steps as well as for the initial strain-free state of the cable. The Lorentzian fit for each gain spectrum at each point at the different displacements was drawn as a solid, and dashed-dotted curve in Figure 3-9 for these three strain states. The spectrum for point 6, Figure 3-9 g-h, for all three displacement states remained unchanged with a peak gain at the frequency of the unstrained cable at this point. However, the spectrum associated with point 1 showed (Figure 3-9 a-b), apart from the unstrained state, two clear peaks with shifts in the frequency domain corresponding to each displacement state. Therefore a Lorentzian fit to each spectrum can be applied to detect the frequency at which the gain was maximized.

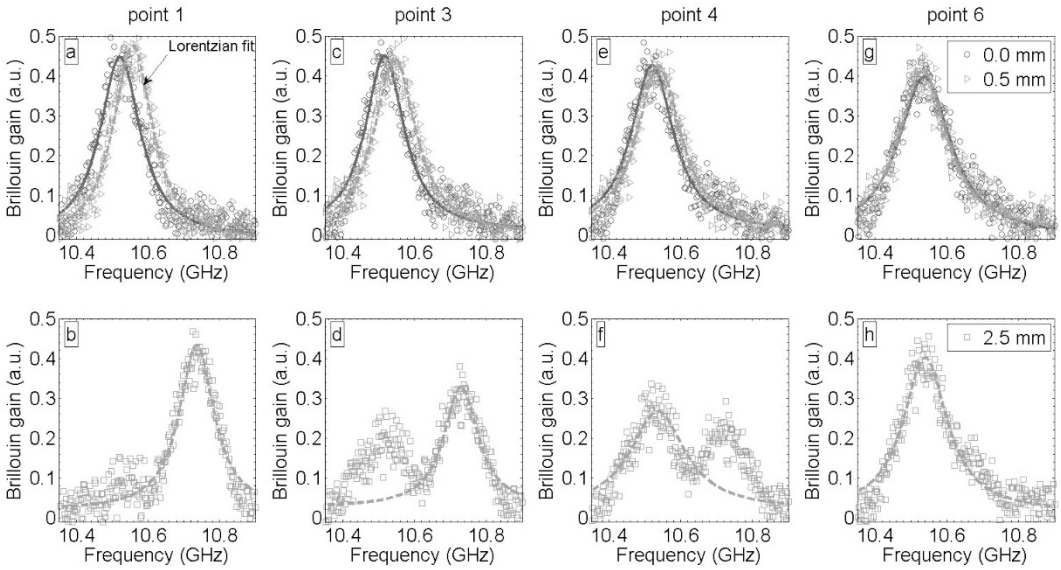

Figure 3-9 Brillouin gain spectra for the six points shown in Figure 3-8. Points 2-5 show two separate peaks at every displacement step corresponding to both strained and unstrained sections

At the points 2 to 5 indicated in Figure 3-8, the spatial resolution covered both unstrained and strained sections of the cable so that the gain spectrum for each displacement peaked at two locations, corresponding to the two sections. This gain spectrum can be considered as the sum of individual gain spectra of an unstrained and a strained length, $g_0(\nu)+g_\varepsilon(\nu)$, which are in the range of the spatial resolution (Figure 3-10). Therefore the gain peaks without any shift in frequency for the non-strained section, whereas there would be a shift in frequency of the strained section relative to the amount of applied strain. Also, the gain peak of the strained section varies depending on the strained length, i.e. the shorter the length the smaller the peak. This is evident from comparing points 5 to 2, where the strained length increases from 10 to 40 cm.

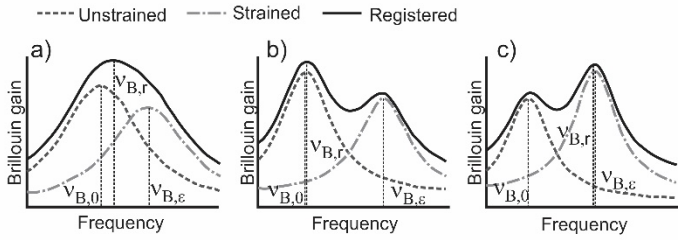

Figure 3-10 Brillouin spectrum for a strained section when the applied strain a) is lower than the critical strain, b) is higher than critical strain but the strained section is shorter than unstrained length, c) is higher than critical strain but the strained length is longer than unstrained section, modified from (H. Zhang & Wu, 2008)

Returning to points 3 and 4 in Figure 3-9 c-f, at low strains the peak gain of the strained section was hidden in the tail of the gain spectrum for the unstrained section. Therefore, a Lorentzian curve was fit to the spectrum which peaked at a frequency very close to the peak gain of the initial state. At higher applied strain, the peak gain in the strained section increased enough to be distinguished from the peak of the unstrained section, giving two individual peaks. However, the peak of the strained section decreased from point 3 to point 4 since the strained length decreased from 30 cm

to 20 cm between these two points. At point 4, this caused the peak at the strained section to drop to values smaller than over the strain-free section. This variation in the length of the strained section from point 3 to point 4 resulted in peak gain detection at the frequency of the unstrained section as the final frequency, similar to Figure 3-10b, whereas the largest of the two peaks at point 3 corresponded to the strained section, so the frequency of the strained section was estimated as the final measured frequency, as conceptually sketched in Figure 3-10c and observed in Figure 3-8.

An important finding is that the relative Brillouin frequency shift does not show measurable changes with different strained lengths less than L_{SR}, whereas the Brillouin gain factor shows such a dependency, i.e. it increases as the strained length increases up to the length of spatial resolution. In other words, in contrast to what Ohsaki et al. (Ohsaki et al., 2002) showed, $\Delta\nu_B$ behaves independently of the strained length, as seen in Figure 3-9, whereas $\Delta\nu_B$ remains constant for all points, although each point gives a spectrum peak of different magnitude. This explains why the system registered the $\Delta\nu_B$ profile for the lengths $L_{SR}/2<l<L_{SR}$ shown in Figure 3-6.

Another point worth noting is that at low strains, the amount of change in the Brillouin frequency shift is so limited that, particularly for short strained lengths, i.e. $<L_{SR}/2$, the peak gain of the strained portion of the cable becomes hidden in the peak gain related to the unstrained length (Figure 3-10a). Researchers have considered different values for this strain limit including 1000 με (H. Zhang & Wu, 2008) and 3000 με (Iten & Puzrin, 2009). In this experimental study, the strain limit was evaluated to be at 2500 με, i.e. 1.25 mm for a 50 cm strained length.

The strain limit explains why the frequency profile over the strained length of the cable varies in its shape from a ′bell curve′ at low strains to a ′boxcar′ at high strains, specifically with respect to the Brillouin spectra at points 3 and 4. Figure 3-11 shows such a transition for a 60 cm strained length of cable stretched up to 3 mm. The shape conversion occurred at about 1.2 mm displacement, corresponding to 2500 με, as obtained from the Brillouin spectra shown in Figure 3-9.

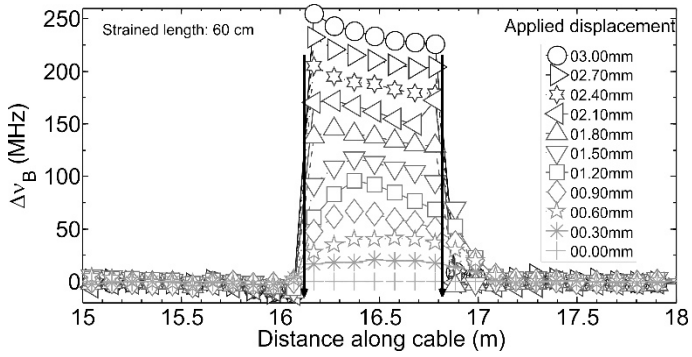

Figure 3-11 Transition of $\Delta\nu_B$ profile from a bell curve shape at low strains to a boxcar shape at high strains. Two arrows show the locations of clamps.

4. Experimentally evaluated optimum installation procedure of a DBS in an underground mining

4.1. Introduction

Based on records of distant events (>100 m) that occurred at the Creighton Mine in Sudbury, Ontario, Kaiser et al. (Kaiser et al., 2005) raised the possibility that the interdependence of widely-separated seismically active areas could be explained by a deformation-controlled process in the rock mass. They used a "train analogy" to describe the sequential movement of rock blocks from close to the mined boundary to remote distances. As soon as the train locomotive starts to move, all wagons begin to displace from the nearest attached to the last one at the end of the train, but with some retardations (Cole, 2006). Applying this analogy to a rock mass, understanding when and how much each individual block displaces provides important knowledge in displacement transfer rates and rock mass evolution. As shown in Figure 4-1, knowing the displacement field between two or more openings with high seismic activity (e.g.: along profile AA') is central to the estimation of the time, location, magnitude and probability of a remote seismic event. The train analogy raised by Kaiser et al (Kaiser et al., 2005) is similar to the slider block model proposed by Burridge and Knopoff (Burridge & Knopoff, 1967) to explain the temporal and spatial interrelations~~hip~~ between sequential earthquakes, showing how cumulative small events may trigger larger events.

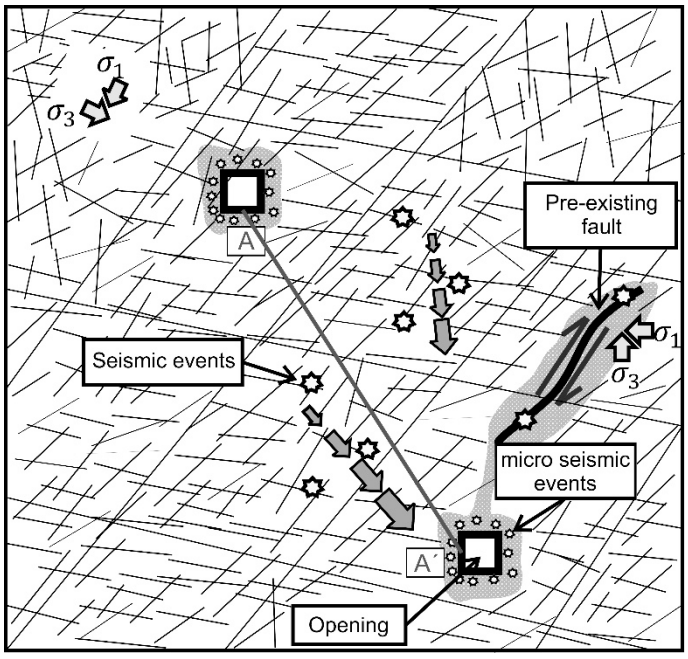

Figure 4-1. Large seismic events located away from active mining areas might be associated with the rock mass movement toward openings over time with increases in extraction ratio (Shaded areas are where the stress change might be

significant). Continuous rock block displacement measurements over large distances could help understand the distribution of remote seismic events

Conventionally, strain or displacement measurements in underground mining were implemented with point sensors. Multipoint extensometers allowed displacement monitoring with a limited number of anchors because of difficulties associated with borehole configuration, installation procedure, and so on. Therefore, to study if correlations exist between rock mass displacements and remote seismic events, new monitoring capability is required that could provide a more comprehensive insight about the displacement field around and away from openings.

Recently developed distributed Brillouin sensing (DBS) systems are strain monitoring devices that, in conjunction with purpose-built fiber optic sensors, can continuously provide a linear strain field over large distances. In this chapter a DBS has been adopted for laboratory-scale testing to evaluate its capability in mining application. The main objectives of this chapter include the DBS response to various deformation sequences and spatial configuration, the ability to detect joint opening with the sensing cable embedded in the borehole filler, the optimum installation method, and the effect of mechanical properties of the filler on the strain transfer process from host rock mass to the cable.

4.2. Test setup

The test setup used in this study consists of three moving and one fixed plates (Figure 4-2). Moving plates are equipped with two ball bearings to travel smoothly on shafts in both backward and forward directions independently from other plates. The SMARTprofile™ can be clamped to the plates to create different testing configurations; e.g. clamping to all four plates providing three cable sections with 50 cm strained length (L_G), to three plates to give two cable sections of 50 and 100 cm long, or tightened to only two plates to have one single section of the sensing cable with 150 cm strained length. The cable between every each two clamps were pre-tensioned to different levels (varying from unstrained to several hundred με) depending on the easiness of clamping of each section of the cable.

There are four blocks at the front and back of moving plates that each have a 10 cm long full-thread hexagonal bolt. These blocks are meant to either apply a driving force to the plates or preventing them from further movement. The plate movements were measured by accurate digital and dial gages. Also, temperature was read through a digital thermometer, although the temperature was constant in all tests presented in this chapter.

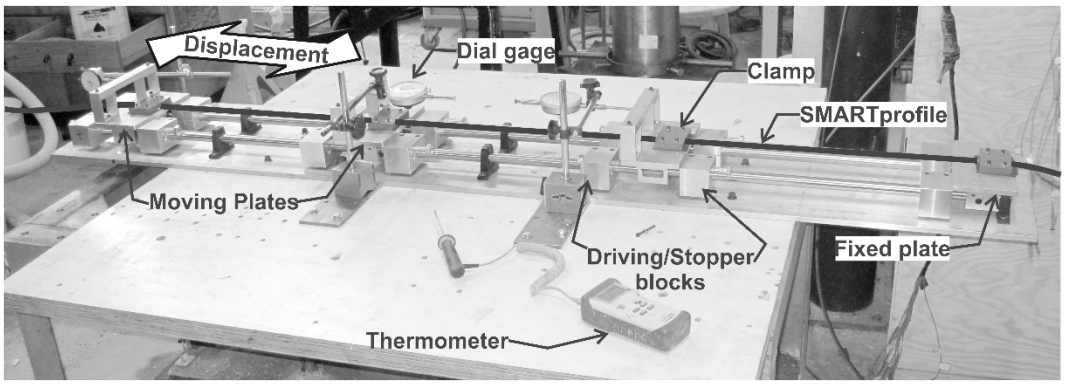

Figure 4-2. Test setup for evaluation of the DiTeSt™ for monitoring of various strained sections. The sensing cable is passing through the testing system and is clamped on plates at four locations. Three of the plates can move longitudinally in two directions independently while the fourth one is fixed. Independent measurement of the plates movements are obtained with micrometric dial gages. The driving/stopper blocks permit controlling the displacement of the plate using a full-thread hexagonal bolt. The overall length of the testing system is 150 cm permitting to strain independently the sensing cable over three sections of 50 cm.

4.3. Strained length selection

The reason that a length of 50 cm was considered for the strained length, L_G, i.e. the distance between two clamping point, was that this length is the minimum spatial resolution, L_{SR}, currently available in the DiTeSt™. So, according to the spatial resolution constraint, all strain events with a length larger than L_{SR} would be registered by the DiTeSt™ with full accuracy, although our experiments (Madjdabadi et al., 2016) showed that strain can be measured even for strained lengths less than L_{SR}, but larger than $L_{SR}/2$. From an initial evaluation of the DiTeSt™ the base noise level was characterized to be of ± 77 με; therefore, with 50 cm strained length, an elongation of at least 0.0385 mm is required to be detected univocally by the system.

4.4. DiTeSt™ evaluation under tension

In this section, the DiTeSt™ response was evaluated when SMARTprofile™ (the sensing cable) was clamped to the plates under different configurations and displacement scenarios. This section explains how the measurement system (DiTeSt™ and sensing cable SMARTprofile™) responded to different patterns of deformation in space and various sequence of the deformation events. In these tests the cable was directly put under strain by clamping it to the test setup plates presented in Figure 4-2. Such knowledge is required prior to evaluating the system response when the sensing cable is placed in a situation more representative of field installation in a borehole, e.g. with embedment of the sensing cable in a mortar filling material.

4.4.1. Spatial distribution of strained events

The strain pattern in a rock mass is likely heterogeneous with strain localization on planes of weakness like rock joints. Depending on the rock joints spacing relative to the spatial resolution of sensing system (in our case L_{SR} = 50 cm), various spatial pattern of deformation can be expected. If the joints are relatively widely spaced, the strain induced by each joint will generate a distinct response in the measurement record, while if the joint spacing gets relatively narrow compared to

the system resolution, the strain induced by multiple joints will interact and will be blended in a single combined response.

The results presented here then aim at investigating effects of spatial distribution of such strained events. For this purpose, the test setup of Figure 4-2 was used in the configurations presented in Figure 4-3. Two main cases were considered: 1) an interacting case with strained sections directly adjacent to each other and 2) a non-interacting case with strain free sections. In the first case with closely interacting deformations, a 170 cm length of cable was clamped at four locations (each clamp has a width of 5 cm), as shown in Figure 4-3a. For the second case with well separated, non-interacting deformations, strain free cable loops were added between the strained sections (Figure 4-3b). To insure non-interactions, strain-free loops of 150 cm (3 times the spatial resolution) were introduced. An intermediate situation, a third case, was also considered with short strain-free loop of only 30 cm (less than the spatial resolution). So in summary, the lengths of cable to be strained was always set at 50 cm, while the strain-free section would have three different lengths including 0 (interacting case Figure 4-3a), 30 cm (intermediate case), and 150 cm (non-interacting case with two loops shown in Figure 4-3b).

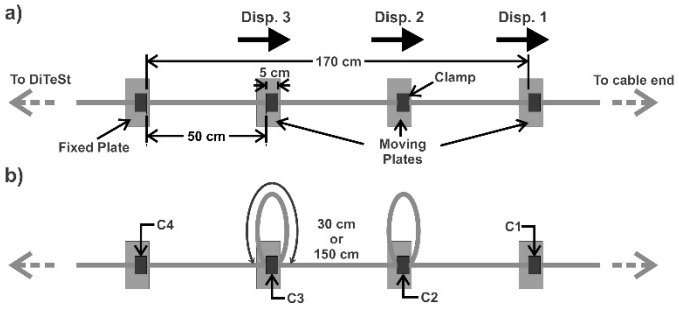

Figure 4-3. Sensing cable configuration to study the response of the DiTeSt™ to different spatial distribution of strained events where they are located adjacent to each other (a) and when they are spaced at distances longer (or shorter) than spatial resolution (b)

The displacement applied to each section was different from each other's; the first, the second, and the third plates were displaced in five straining steps to a maximum amount of 3.0, 1.5 mm, and 0.5 mm, respectively, resulting in 1.5 mm, 1.0 mm, and 0.5 mm relative displacements. With a constant 50 cm strained length, this displacement scenario induced a strain level in the first section which was one and half times the second section and three times the third section, i.e. $\varepsilon_1=1.5\times\varepsilon_2=3\times\varepsilon_3$. These ratios were always kept constant at each straining steps.

Figure 4-4 shows Brillouin frequency shift change ($\Delta\nu_B$) relative to the unstrained state of the cable along the sensing cable for all three configurations. In the figure, the location of clamps (C_1-C_4 in Figure 4-3) is indicated as well as the strain-free sections. From Figure 4-4a, the frequency (strain) profile shows a single continuous step-like strained section. So, the discrimination between three separate intervals might not be straightforward, depending on the applied displacement to each section. In other words, if equal displacement is applied to all three sections the final frequency profile will be a continuous flat interval where the discrimination between strained sections would be challenging. In contrast, from Figure 4-4c, the strain profile registered three

individual strained sections separated from each other with a 150 cm free-of-strain section. Finally, Figure 4-4b shows the intermediate situation, i.e. although there are clearly three strained sections, the free-of-strain section is not long enough to be uninfluenced by the straining. In the latter two cases, three individual strained intervals will always be recognized even if the same strain is applied over each strained length.

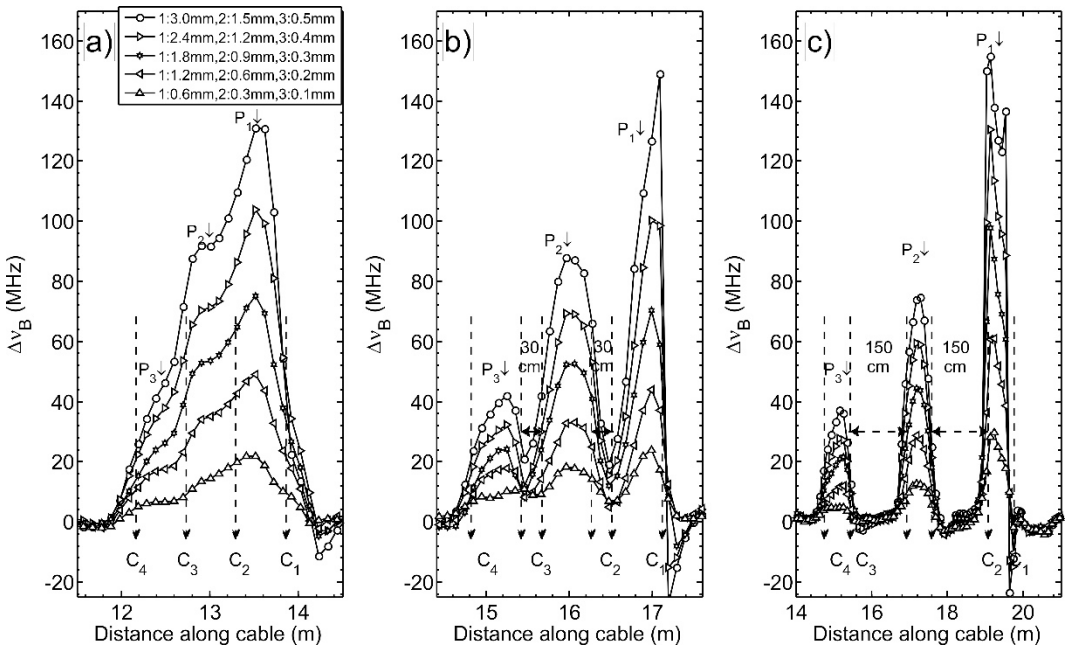

Figure 4-4. Brillouin frequency shift change, $\Delta\nu_B$, for tests containing a) zero, b) 30 cm, and c) 150 cm strain-free sections between three successive strained intervals shown in Figure 4-3. With a 50 cm spatial resolution, a frequency change was detected over strain-free lengths shorter than L_{SR}. C_1-C_4 and P_1-P_3 represent the clamps location as shown in Figure 4-3 and middle points along each strained interval

What is actually happening in the case with 30 cm strain-free section is schematically shown in Figure 4-5. The Brillouin frequency shift change, $\Delta\nu_B$, at each sampling point, e.g. point p in Figure 4-5a, is computed over the spatial resolution, L_{SR}. Therefore, according to the set L_{SR}=50 cm and the 10 cm sampling interval for the DiTeSt™, five points including two points ahead and two points behind the point p contribute to the $\Delta\nu_B$ at this point. This is better understood when looking into the Brillouin gain spectra (BGS) at this point, Figure 4-5b. $\Delta\nu_B$ at each point is estimated as the peak gain function over a frequency range. At point p, the final registered gain is a sum of three sub-gain functions associated with three different strained sections over the spatial resolution. The first gain spectrum peaked at ν_0 corresponds to three points including point p located in the strain-free section, resulting in the largest sub-gain peak. Two other gain spectra peaked at $\nu_{\varepsilon 1}$ and $\nu_{\varepsilon 2}$ are recorded at far left and right points located in the first and second strained sections, respectively. These functions peak at the same gain amplitude but at different frequencies; a higher frequency corresponds to a higher strain. Finally, the resultant gain spectrum obtained from summation of these gains peaked at a frequency (ν_{obs}) closer to the strain-free gain spectrum. A more comprehensive explanation of the estimation of measured BGS at various locations of the cable is given in section 0.

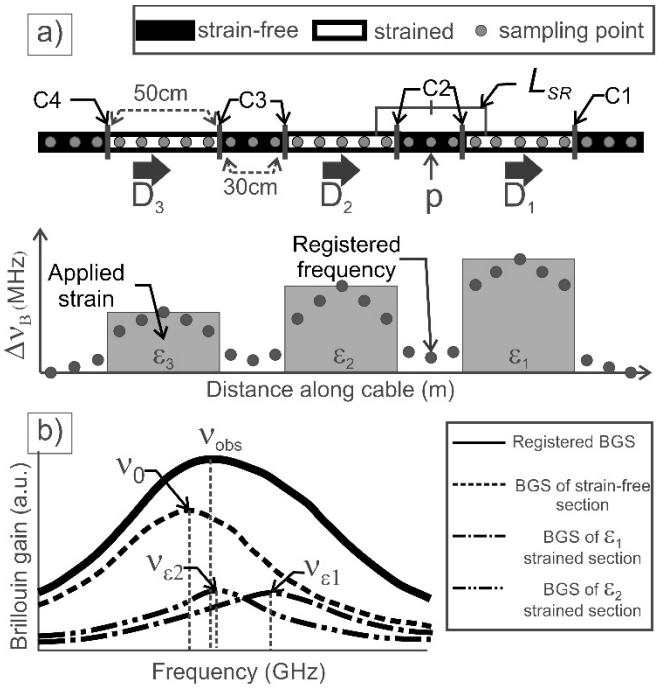

Figure 4-5. a) A schematic presentation of $\Delta\nu_B$ at each sampling point along the cable for the test with 30 cm strain-free section, b) a typical registered Brillouin gain spectrum (BGS) at sampling point *P* located in the strain-free section. Final BGS resulted from the contribution from all strained and unstrained sections at every sampling point like point *p*. ν_0, $\nu_{\varepsilon 1}$, $\nu_{\varepsilon 2}$, and ν_{obs} represent frequenciea at which unstrained, first and second strained section, and final BGS peaked.

Figure 4-6 graphs the $\Delta\nu_B$ against applied strain for the middle point of each interval, indicated by P_1, P_2, and P_3 in Figure 4-4, for three configurations. The solid black line is the system manufacturer's correlation between Brillouin frequency shift change and applied strain, while the dashed one is a newly determined relation based on the tests performed by Madjdabadi et al (Madjdabadi et al., 2016). The error bars above and below each point in the figure represent the noise level of ±3.8 MHz on $\Delta\nu_B$ typical for this system. The measurements here was in agreement with the Brillouin frequency shift change to strain relation derived by Madjdabadi et al (Madjdabadi et al., 2016).The proportion of the relative strain between each strained section, i.e. ε_1=1.5×ε_2=3×ε_3, were also accurately captured by the system. These results confirms the validity of the linear correlation between the Brillouin frequency shift change and applied strain independently of the exact strain pattern and configuration.

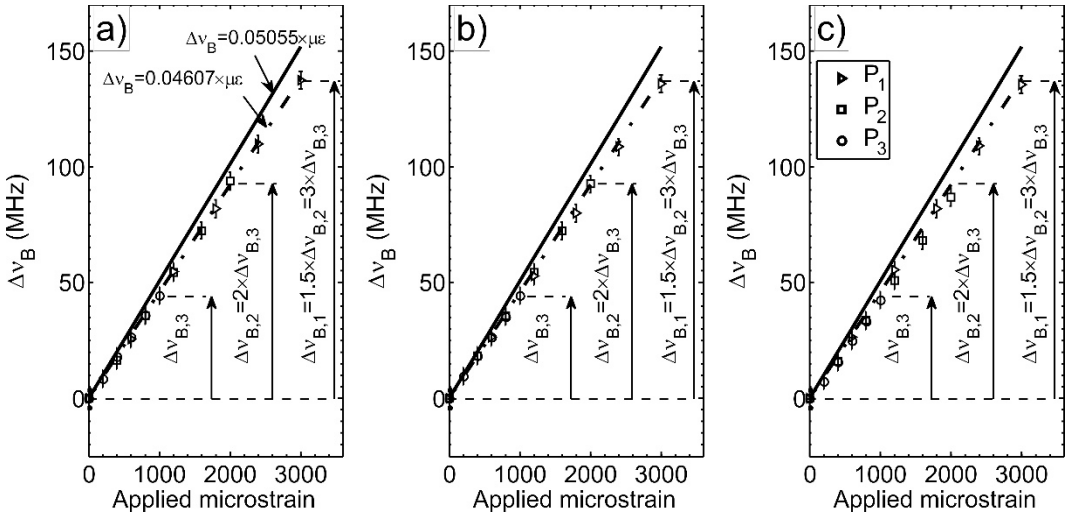

Figure 4-6. $\Delta\nu_B$ against applied strain at three points indicated in Figure 4-4 for tests containing a) zero, b) 30 cm, and c) 150 cm strain-free sections shows perfect agreement with best-fit correlation determined by Madjdabadi et al. (2015). It is shown that the application of the same displacement scenarios for three different spatially distributed strained events resulted in the same frequency-strain relationship

4.4.2. Effect of deformation sequence

In the previous section, the spatial response of the system was evaluated in a way that three individual adjacent sections were simultaneously strained. Another testing approach was followed to better study the effect of straining sequence, i.e. the loading path effect on the system response. To approach this objective, compared with the former test, in this test every section was moved to its final displacement before the next plate was moved. The first, second, and third plates were displaced to 3.0, 1.5, and 0.5 mm, respectively, similar to what was done in the spatial response test.

Figure 4-7 shows the same three configurations as in the previous test, but obtained through a new straining sequence. The figure displays the frequency profile at the final stage of each strained section; i.e. after moving the first plate to 3 mm, the second plate to 1.5 mm followed by displacing the third one to 0.5 mm. As expected, the frequency change response for the first (or the second) strained interval dropped almost as much as that of the second (or the third) strained interval increased.

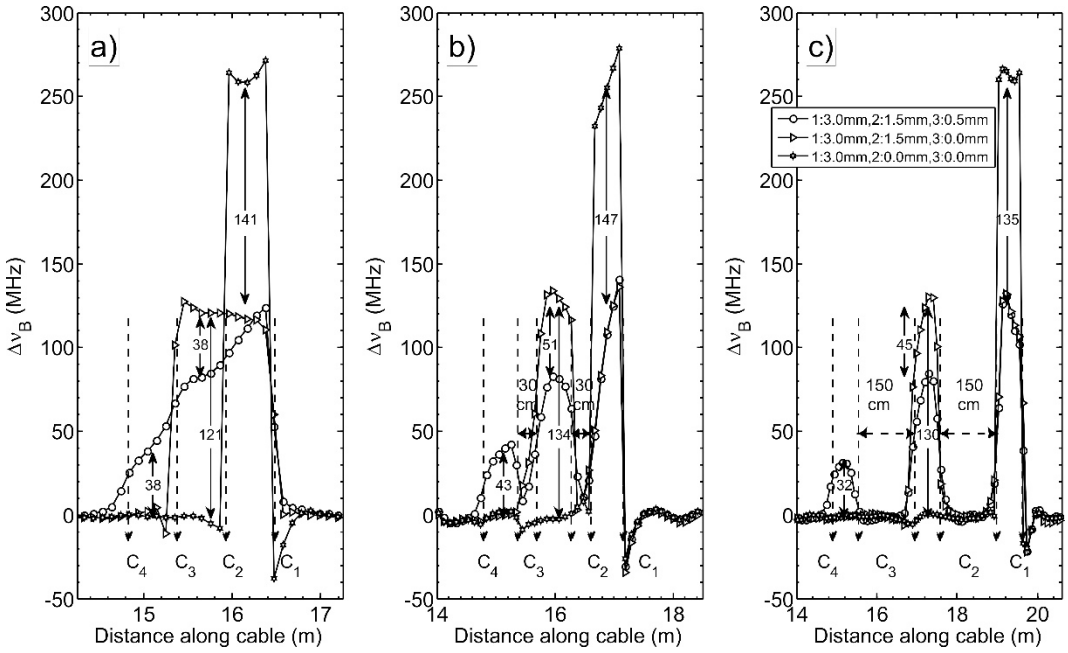

Figure 4-7. Sequential response of the DiTeSt™ for tests containing a) zero, b) 30 cm, and c) 150 cm strain-free sections. The final frequency change profiles for the spatial response test were obtained during this test using a different loading path (red graphs) simulating an opening and closing sequence of rock blocks

There were, however, slight differences between frequency changes during loading (*L*) with those recorded during unloading (*U*) steps that might be larger than the standard deviation of frequency change for repeated measurements of a constant strain over a strained length (error bars limits in Figure 4-6). For example in Figure 4-7c, straining the second section with a 1.5 mm displacement induced +130 MHz, while at the same time the first section was equally unstrained from 3 to 1.5 mm but a larger reduction of 135 MHz was observed. Similarly, applying 32 MHz strain-equivalent (0.5 mm displacement) in the third section resulted in a relaxation of 46 MHz strain-equivalent in the second section.

The major contributor to this difference was thought to be associated with the systematic difference in the frequency response between loading and unloading of the cable. To better explore this system's behavior, three different lengths of the sensing cable including 60, 80, and 100 cm were applied 4000 με and the strain was then released in a step-wise manner. When all measurements were referenced with respect to the first zero reading, as shown in Figure 4-8a for the 60 cm strained interval, the unloading associated graphs (triangles) showed less frequency compared with those from loading path (circles). Even the final measurement, i.e. zero displacement in unloading path, registered smaller frequency than the first reading (frequency change for this final measurement was negative). Note that the frequency differences between straining and relieving paths are larger than the base noise level (shown as error bars at each measurement point) of the system.

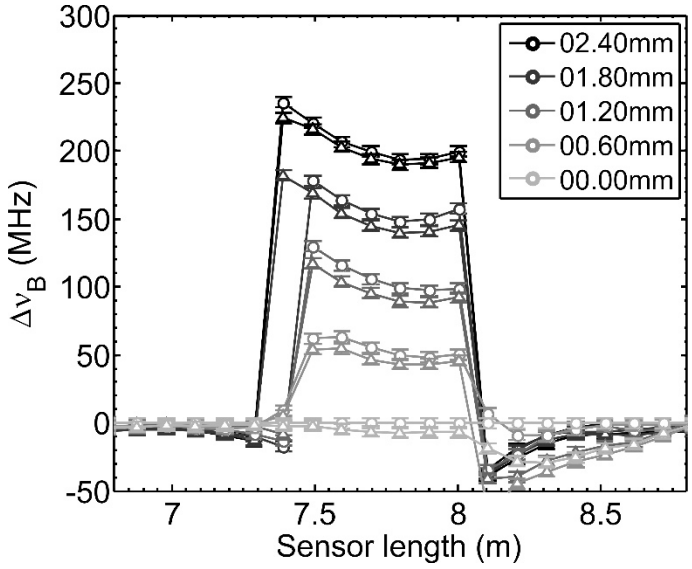

Figure 4-8. The frequency difference over a 60 cm strained interval in loading (circles) and unloading (triangles) paths when the measurements were referenced to the first measurement

When plotting the frequency change at each point along the strained length for each test, it was noticed that all unloading associated frequencies, unrelated to location along the length, was slightly lower than those related to the loading path. The reason for this small difference remains unexplained. However, since it is a systematic rather than random factor and the difference was quite close to the base noise level, such a response did not affect the overall findings of the testing program.

4.5. Mortar-cable interaction

So far, the straining pattern and the effect of the straining sequence have been studied while extensional displacements were directly applied to the sensing cable. However, to use this system for monitoring the displacement field around underground mines, the cable must be placed in a borehole filled with a proper grout mixture.

In the following sections, the installation method of the sensing cable was experimentally evaluated. The DiTeSt™ response was studied when the sensing cable was embedded in a mortar beam with the mix design given in Table 4-1. This study aimed at simulation of the cable-grout interaction when the cable is installed in the borehole. Tests included the embedment method within mortar, the effect of joint spacing, and the effect of mortar thickness and strength on the strain transfer process. All tests were implemented on 2 m long mortar beams.

Table 4-1. Mix design for mortar beams including strong and weak mortars. The two mortar types were only different in the cement portion

	Material	Cement	Lime	Sand	Water
Weight (kg)	Strong mortar	2.4	1.8	21.4	4.0-4.5
	Weak mortar	1.2	1.8	21.4	4.0

4.5.1. Embedment method

Distributed optical fiber sensors have been installed in different ways in civil and geotechnical projects. They have been fully glued to bridge steel girders (Glišić et al., 2007; Minardo et al., 2012), placed within soil embankments (Hiroyuki, 2001) with the sensing cable attached to an inclinometer casing grouted into a soil borehole (Roland Hoepffner, 2008) or attached by pins at a certain spacing along a tunnel wall or concrete lining (Hisham Mohamad, Bennett, Soga, Mair, et al., 2007; Naruse et al., 2006).

The method by which the sensing cable is installed is very important in order to achieve a high performance monitoring response. In this study, the goal is to install the cable in a long borehole in a jointed rockmass, followed by grouting of the borehole. Two different installation approaches of the SMARTprofile™ sensing cable, motivated by the monitoring program objectives and DiTeSt™ limitations, have been tested. In the first configuration, the bare cable was embedded in the filling material, i.e. the mortar beam, and its entire length covered with grout. The second method included the anchoring of the cable at a specific spacing, the debonding of the cable section between each anchor pair using a debonding agent, and the grouting of the cable system (including anchors and debonded sections) into the mortar beams. Both these installation methods were studied to understand the optimum installation method for strain transfer process in a mining situation.

4.5.2. Uncontrolled self-debonding for the fully embedded case

A 38.1 mm×38.1 mm×2 m (*width* × *height* × *length*) beam was cast with the strong mortar mix design given in Table 4-1. The bare cable was entirely embedded inside the mortar to be in direct contact with the mortar, and pre-tensioned at each end with 1 kg dead weight. After one week curing, the beam was placed on the moving table and clamped at three locations separated by 55 cm (Figure 4-9) to simulate a rock joint opening process by inducing cracks into the mortar beam. Also, in order to ensure that cracks would form, a small notch at each crack location was created in the beam.

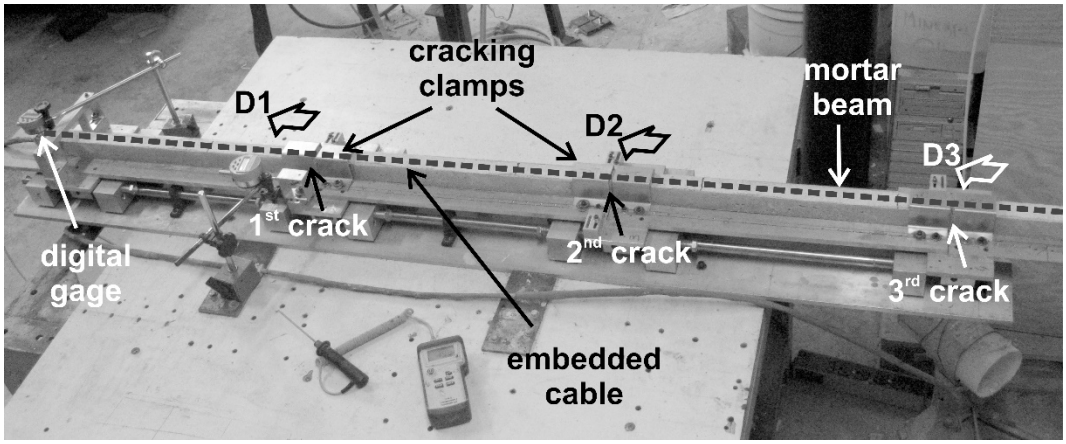

Figure 4-9. Photograph of the setup to test the deformation of the cable embedded in a mortar beam. Cracks were induced at three 55 cm separated locations where the beam was clamped and different displacements (D_1-D_3) applied

These three cracks were formed and opened based on a displacement sequence given in Table 4-2. The displacement scenario had one step for each moving plate. At each step, the plate of interest was moved to its final desired location (absolute displacements in Table 4-2). Then before the next plate was moved in the same manner, the first plate was fixed to the second plate in order to have a constant crack opening. The absolute displacement represents the amount of movement of each plate, whereas the relative displacement represents the corresponding crack opening for each plate. One measurement was recorded at every 0.1 mm displacement of each plate.

Table 4-2. Displacement sequence followed to induce three ongoing openinig cracks in the mortar beam

Displacement step	1st plate displacement (mm)		2nd plate displacement (mm)		3rd plate displacement (mm)	
	Absolute	Relative	Absolute	Relative	Absolute	Relative
1	3.0	3.0	0	0	0	0
2	4.5	3.0	1.5	1.5	0	0
3	5.0	3.0	2.0	1.5	0.5	0.5

The main objective of this test was to understand the ability of the DiTeSt™ in crack detection in the mortar beam as well as registration of strain localizations due to crack opening at different locations along the beam with a fully bonded and embedded cable inside.

Figure 4-10 shows the Δv_B relative to the initial state (i.e. with a pre-strained cable but an unstrained mortar beam) along the length of the sensing cable, where it enters and leaves the beam (indicated by *b.s.* and *b.e.* in Figure 4-10). At the first crack location, a visual inspection of the beam indicated that a crack was induced at displacements below 0.1 mm or so. However, the first detection of the crack opening at this location, point P_1 in Figure 4-10a, happened after 2.0 mm displacement. Before this movement no frequency response was observed that could be attributed to strain localization. At this displacement only two points close to the first crack location showed a clear frequency response. Increasing the crack opening from 2.0 mm to 3.0 mm caused a frequency profile response at two more points adjacent to the previous points.

After the first displacement step, the second plate was moved to 1.5 mm with a measurement every 0.1 mm. The second crack also formed at almost the same displacement as the first crack, but the frequency profile showed no change until 0.5 mm. From this displacement, the total number of points showing the frequency response increased gradually to seven as the relative opening of this crack reached 1.5 mm. At step 3, although the crack was formed at a small displacement of 0.1 mm, the frequency profile did not change at all over 0.5 mm displacement of this plate.

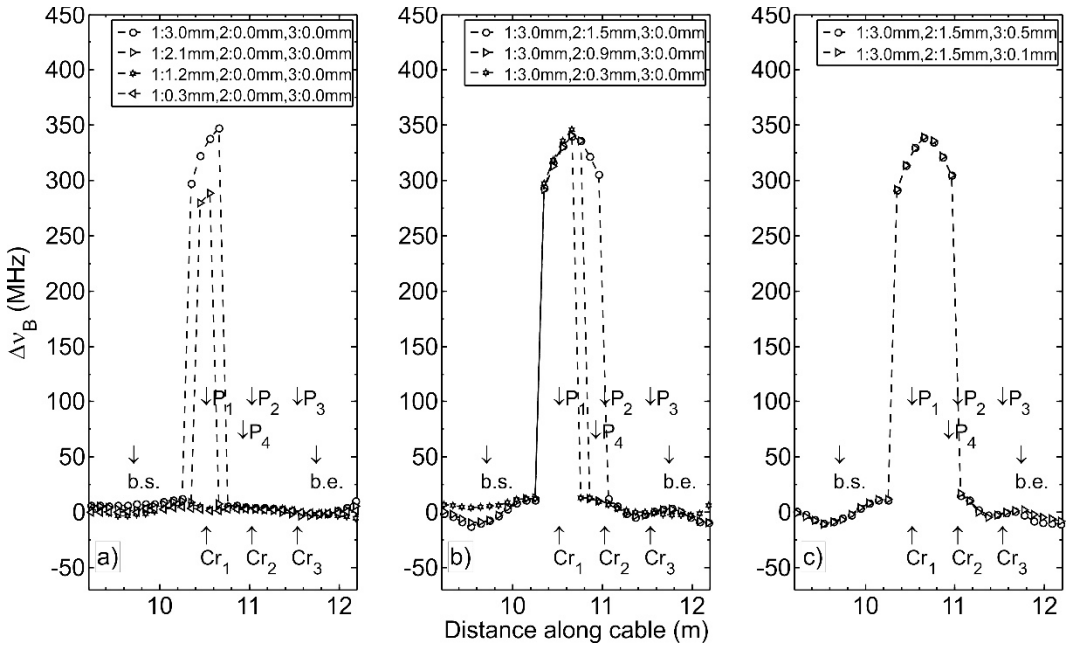

Figure 4-10. $\Delta\nu_B$ along the embedded cable in the mortar beam at the first (a), second (b), and third (c) displacement steps as three cracks were induced and opened. The most responsive step was when the first crack opened 2.0 mm, whereas the opening of the second crack only slightly affected the strained length of the cable. The frequency profile did not show any response upon opening of the third crack. P_1-P_3, Cr_1-Cr_3, b.s., b.e., and P_4 represents three points at the three cracks, beam start and end locations, as well as the point between Cr_1 and Cr_2 respectively.

The way DiTeSt™ responded to the applied displacement in this test was mainly controlled by the self-debonded length (the cable length that debonded from the mortar during displacement) of the sensing cable. Figure 4-11 plots $\Delta\nu_B$ against the applied displacement corresponding to each individual crack at three different points located at the three crack locations, as indicated by P_1, P_2, and P_3 in Figure 4-10. The six marked lines represent the best-fit linear correlation between $\Delta\nu_B$ and the applied displacement for six strained lengths obtained based on an extensional test on various lengths of SMARTprofile™ (Madjdabadi et al., 2016).

Since debonding occurs in an uncontrolled manner, the detailed interpretation of the measurements requires some guessing of the debonded length at any measurement time. Upon movement of the first plate at step 1 at the first crack location, the cable likely started to debond around this crack. Since the system was not able to register any $\Delta\nu_B$ before the 2.0 mm crack opening, we assume that the self-debonded length was less than $L_{SR}/2$. However, as shown in Figure 4-11a, this length became sufficiently large (varying from 40 to 50 cm since $\Delta\nu_B$ followed the best-fit correlation lines associated with these strained lengths) for displacements above 2 mm so that $\Delta\nu_B$ was detected by DiTeSt™.

Similarly at step 2, the cable was likely self-debonding during all displacements, but the system at this crack location became responsive only at crack openings above 1.4 mm when the self-debonded section increased to more than 25 cm. Note that the $\Delta\nu_B$ at the location of the first crack, i.e. point P_1, remained constant during application of the displacement to the second crack, Figure 4-11b. This was expected from the displacement sequence given in Table 4-2, where the

first crack opening was kept fixed during opening of the second crack. This also indicates that both self-debonded lengths did not coalesce. For the third crack, in contrast to the other two cracks, no $\Delta\nu_B$ was detected by DiTeSt™ and we assume that the self-debonded length never increased above $L_{SR}/2$ (Figure 4-11c).

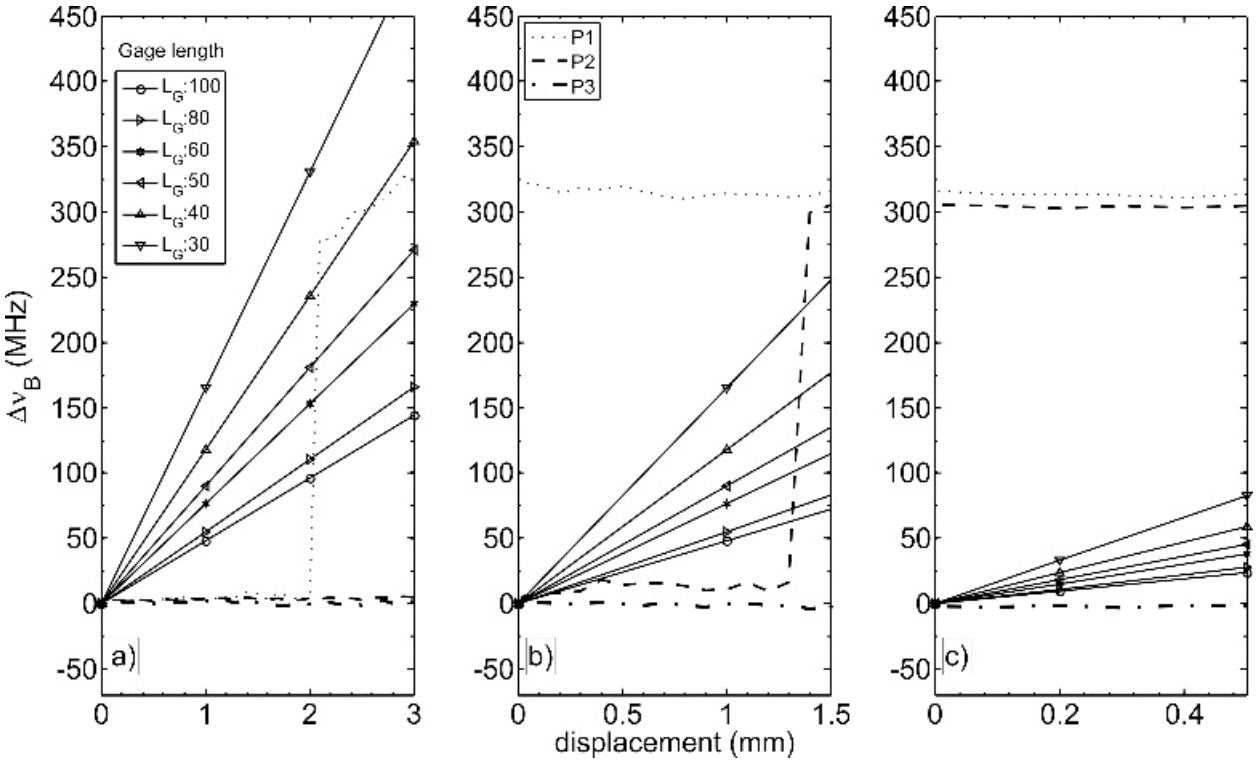

Figure 4-11. $\Delta\nu_B$ against applied displacement for the three sampling points indicated in Figure 4-10 at the first (a), second (b), and third (c) displacement steps. The cable debonding process could be followed at each displacement step. Markers represent the best-fit correlation between $\Delta\nu_B$ and displacement for various strained lengths.

The strained length in this test was not fixed since the cable was detached from mortar in an uncontrolled self-debonding process. Although from Figure 4-11 one can deduce the evolution of this length with applied displacement, the study of the Brillouin gain spectrum (BGS) at certain points along the sensing cable gives further insights in the behavior of DiTeSt™ specifically when some short strained lengths (here three self-debonded sections) are spaced with distances less than L_{SR}. Since the self-debonded length was shorter than L_{SR} during the initial opening phase of all cracks, the gain spectrum at points along this short length was different from a typical spectrum at points located along a strained length larger than L_{SR}. Where the spatial resolution covers points located in both strained and unstrained sections, two peaks would be registered in BGS at two different frequencies, one associated with the unstrained section and one related to the strained length. Actually, the final registered spectrum is a summation of the spectra of these two sections over the spatial resolution distance.

It has been noticed that the amplitude of BGS for both strained and unstrained sections for a strained length shorter than L_{SR} is dependent on the number of points within each section over spatial resolution interval. With a length ratio, r (varying from 0 to 1), defined as the self-debonded strained length, over the spatial resolution, two cases could happen.

Where $r \leq 0.5$, i.e. the spatial resolution window included mostly the unstrained section, the BGS amplitude of this section was higher than that of the strained section. When the strain was below a certain limit, the BGS peak for the strained section occurred at frequencies quite close to that for the unstrained section. Since at this low strain level the self-debonded length was smaller than $L_{SR}/2$, the BGS peak for the strained section became hidden in the shoulder of that for the unstrained section (Figure 4-12b). This resulted in a wider spectrum peaking at a frequency similar to that of the free-of-strain section, as shown in Figure 4-12a for point P_1 located at the first crack for 0.2 mm displacement. At this displacement, the self-debonded length approximately covered only one sampling point, i.e. 10 cm, as sketched in Figure 4-12c.

At higher strain levels, the BGS for two unstrained and strained sections peaked at two different frequencies so that the final registered BGS showed two separate peaks, Figure 4-12d. Since the final BGS has a higher amplitude at the frequency of the unstrained section, the DiTeSt™ internal signal processing algorithm selected this frequency as the Brillouin frequency shift for this point at this displacement. According to the BGS for 1.5 mm opening of the first crack in Figure 4-12a, the self-debonded length of the cable was estimated to be 20-25 cm, as sketched in Figure 4-12e.

On the other hand, with $0.5<r<1$ at high displacements, more sampling points over the spatial resolution length fell within the strained section, so the BGS associated with the strained section showed a higher amplitude in comparison with that for the unstrained section, as shown in Figure 4-12f. Therefore, for all displacements above 2 mm, as shown in Figure 4-12a for 3 mm opening of the first crack, DiTeSt™ detected a Brillouin frequency shift at the frequency of the strained section. In this case, the self-debonded length was found to have grown to 35-40 cm long, as sketched in Figure 4-12g.

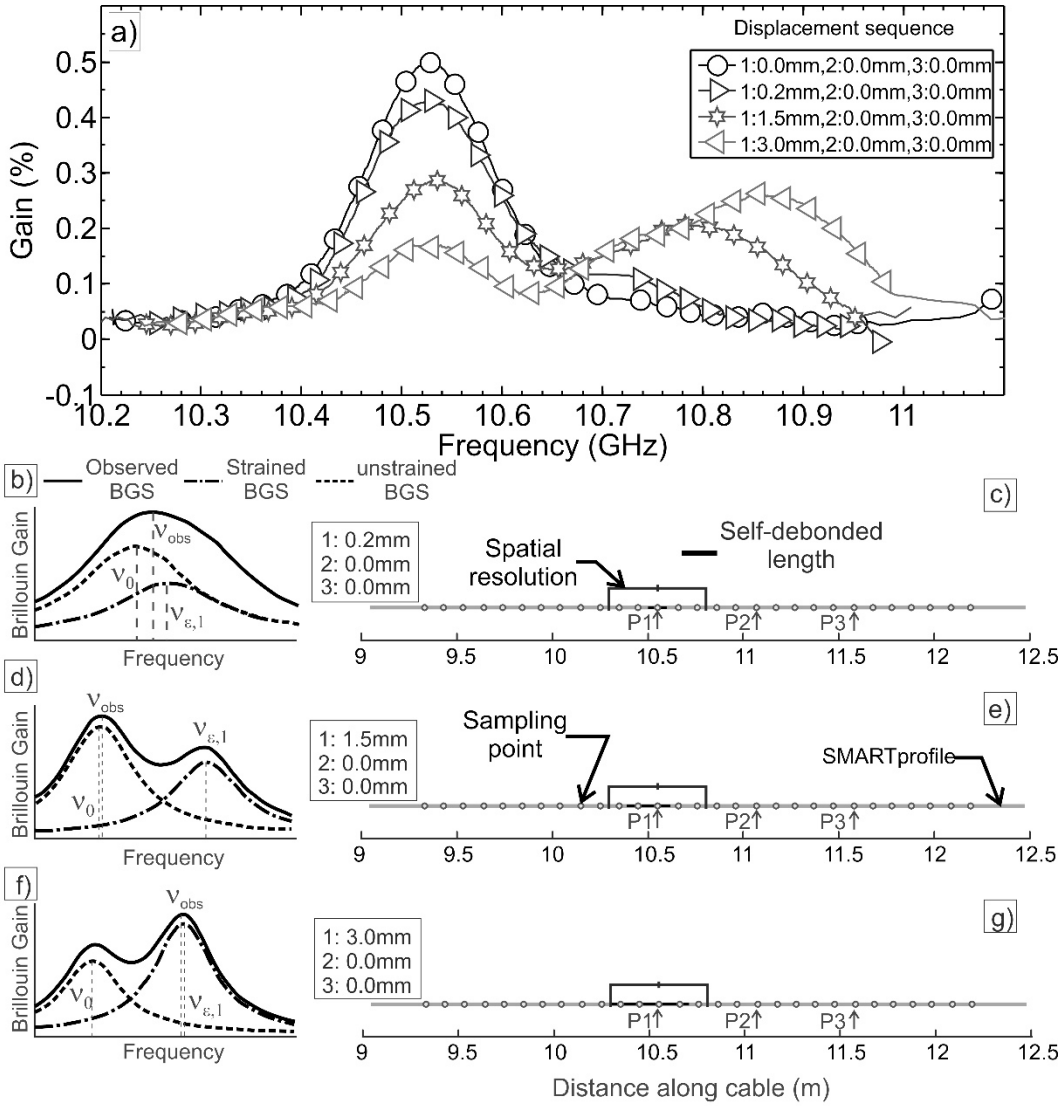

Figure 4-12. a) Brillouin gain spectra of the point P_1 loacted at the first crack location for three different displacement steps. The registered BGS at these displacement steps were schematically presented (b, d, f) where the contribution of various BGSs due to each strained section in the final BGS was noticed where the strained intervals had a spacing less than L_{SR}. Also, evolution of the self-debonded length during these displacement steps (c, e, g) were approximated using the BGS information. Curves in a have been smoothed using a moving average filter with a 5-point span for the sake of better presentation. ν_0, $\nu_{\varepsilon,1}$, and ν_{obs} represent the Brillouin frequency with the peak gain for unstrained, strained sections and observed measurement, respectively.

The BGS for those points between the first and second crack location became even more complex when the second crack opened. This complexity was due to the short spacing (i.e. one spatial resolution length) between these events, i.e. cracks. For an example, for any point between the two cracks there are three different BGSs associated with each strained length over the spatial resolution, including an unstrained section and two self-debonded strained lengths at the first and second crack locations. The final registered BGS is a combination of all these three spectra.

Figure 4-13a shows the BGS for a sampling point located between two cracks, as indicated with P_4 in Figure 4-13c. The registered BGS for this point already had two peaks even before starting

the displacement of the second plate (circles in Figure 4-13a). The higher peak belonged to the BGS for the unstrained section containing four sampling points, whereas the lower peak was due to one sampling point located in the self-debonded length of the first crack. During this test, the frequency at which BGS for the unstrained section and the first crack peaked remained constant during the formation of the second crack.

Upon the formation of the second crack, the self-debonded length at this crack was inferred to be about 10 cm, as shown in Figure 4-13c, where the third peak due to formation of the new crack was formed. However, at the early displacements with low strain levels the peak was hidden in the shoulder of the BGS for unstrained section, similar to the sketch shown in Figure 4-12b. At higher displacements above 0.4 cm, the amplitude of the observed BGS at frequencies about 10.66 GHZ increased, as shown in Figure 4-13a. This happened because at the current opening (i.e. 0.4 mm) the strain level was large enough so that the third peak moved away from that for the unstrained section, resulting in an almost flat spectrum between the peaks for unstrained section and first crack, as schematically shown in Figure 4-13b. Simultaneously, the peak amplitude for the unstrained section declined since one out of four points over the unstrained section was already strained due to the second crack. Nonetheless, since the BGS peak for unstrained section was still higher compared to the other two peaks, the Brillouin frequency shift was detected at a frequency close to this peak.

At the final displacement increment of the second crack, i.e. 1.5 mm, the observed BGS peaked at a frequency similar to the frequency of the BGS peak for the first crack, while the peak amplitude at frequency of the unstrained section decreased more (stars in Figure 4-13a). The reason the final BGS peaked almost at the first crack frequency was twofold. First, applying more strain (in this case for displacements above 1 mm) moved the BGS peak associated with the second crack to the right at a frequency close to that of the first crack, as shown in Figure 4-13d. Also, this strain increased the self-debonded length around the second crack to less than 25 cm, covering two sampling points (Figure 4-13e). Therefore the resultant BGS, as a summation of all BGSs, eventually peaked at a frequency close to those of both strained sections. It is interesting that although the second self-debonded length was less than $L_{SR}/2$ and from previous results no frequency response was expected, the presence of another strained section at a distance of $L_{SR}/2$ to the sampling point of interest, i.e. P_4, in the self-debonded length could increase the detectability of the system for the short length events.

With respect to the third crack, the applied displacement could finally induce a debonded length of around 10 cm covering only one sampling point. Such a small strained length was not able to create a high amplitude BGS so as to cause the registered BGS peaks at the frequency of the strained section.

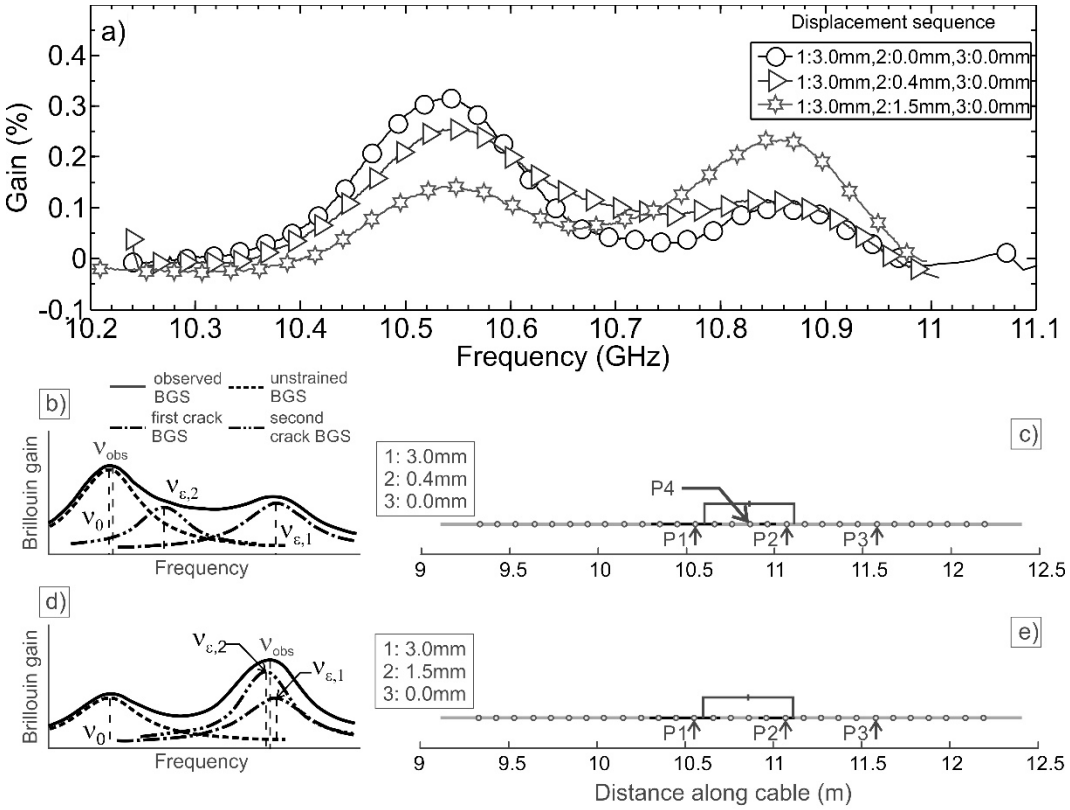

Figure 4-13. a) BGS for the point P4 between the first and second crack locations for three displacement steps. The schematic reconstruction of the final BGS showed the contribution from three BGS's associated with two strained interval and one unstrained section at low (b) and high (d) strain levels during which the self-debonded length grew from 10 cm (c) to less than 25 cm (e), respectively. Curves in a has been smoothed using a moving average filter with a 5-point span for the sake of better presentation. ν_0, $\nu_{\varepsilon,1}$, $\nu_{\varepsilon,2}$, and ν_{obs} represent the Brillouin frequency where the peak gain for unstrained, first and second strained sections, and observed measurement, respectively.

What is understood from this test is that if the strained length is larger than L_{SR} and the sampling point is at least $0.5\times L_{SR}$ away from each end of the strained section, then one spectrum would be present in the observed BGS. As the strained length decreases to lengths below L_{SR} or the spacing of events of different strain levels is less than L_{SR}, then more than one spectrum become involved in the formation of the final registered BGS, which makes identifying an appropriate precise frequency more difficult. This is important with a full embedment installation of the sensing cable because not only the strained length (self-debonded length) varies with more crack opening, but also with presence of more cracks over the spatial resolution, short self-debonded sections are created close to each other.

Note that with the self-debonding cable installation method the DiTeSt™ can detect frequency changes due to crack opening as long as the self-debonded length increases to values above $L_{SR}/2$. Furthermore, there would not be a loss in strain transfer, therefore not only a qualitative but also a rough quantitative estimation of the joint movement could be established. However, non-constant strained lengths due to uncontrolled debonding and the presence of various events at close distances could affect the estimation of the real applied strain. Moreover, since the frequency

change is linearly correlated with applied strain, in order to compute the crack opening the strained length should be fixed and known, thus with this installation method the relative block displacement assessment can include some uncertainties.

4.5.2. Pre-debonded cable embedment

From the primary evaluation of the DiTeSt™ (Madjdabadi et al., 2016), it was found that the minimum required strained length in order for the DiTeSt™ to be responsive was 30 cm, since the strained lengths below half the spatial resolution, i.e. $L_{SR}/2 = 25$ cm would not register any frequency change along the cable length. This was also confirmed in the test presented in section 5.5.1. These results and the difficulty in interpreting the result from measurement where uncontrolled self-debonding occurs suggest us to use an alternate installation method with which the debonded length is controlled and always kept above $L_{SR}/2$.

The idea of this alternative installation method is to have anchoring points along the cables with pre-debonded cable in between. For this purpose, a 2 m length of the cable was first coated with petroleum jelly and wrapped with a plastic film to ensure that the length in between anchors are pre-debonded from the mortar. Then anchors were placed every 50 cm along the cable. Anchors are aluminum blocks with a narrow slot just under 4 mm width (i.e. less than the cable thickness) that can be easily mounted on the cable and tightened. In total, four aluminum anchor blocks were along the test length of the cable, which was then cast with the strong mortar (Table 4-1). In this test, only one joint was present over every anchored interval, therefore the effect of combined movement of joints was not considered for the sake of simplicity and clarity.

The same displacement scenario was followed as given in Table 4-2. Figure 4-14 shows the results of the tension test on this beam after inducing three cracks at a spacing of 55 cm. All cracks were formed at a displacement below 0.1 mm. It was found that the DiTeSt™ could register a frequency change just at the onset of crack development at displacements as low as 0.1 mm. Furthermore, the frequency profile clearly shows three individual strained sections according to the applied displacement sequence corresponding to each joint opening over each interval. This is important in that since the strained length, i.e. pre-debonded anchored interval, is fixed the frequency change could be also related directly to the magnitude of joint opening or closure, not only the induced strain in the cable. This was not possible with the previous method of installation studied.

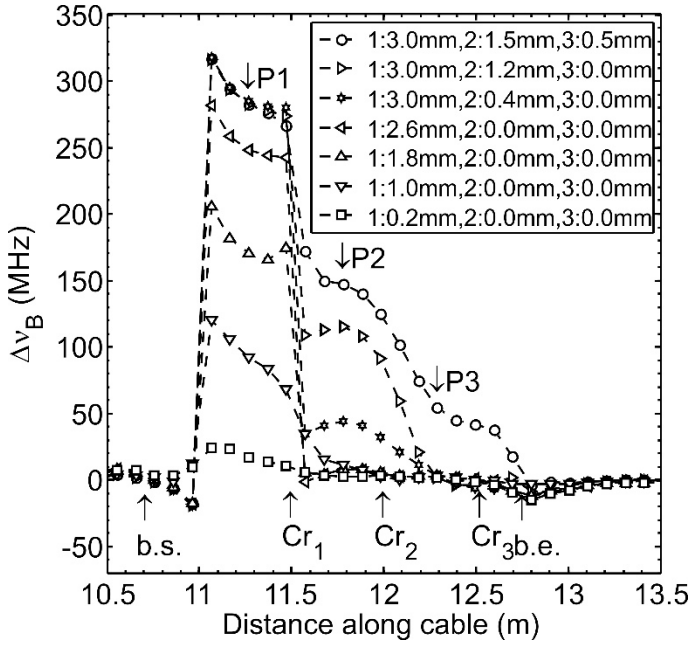

Figure 4-14. $\Delta\nu_B$ for the debonded cable embedment method. The full gage length is mobilized at the early displacement stage. P_1-P_3, Cr_1-Cr_3, and b.s., b.e. represent three points in the middle of each strained section, three cracks, beam start and end locations, respectively.

Figure 4-15 shows the BGS for a point located in the middle of the first interval, indicated as P_1 in Figure 4-14. This figure includes three displacement states associated with the unstrained beam (circles), 0.1 mm crack opening (triangles), and maximum applied opening (stars). In contrast to what Figure 4-12 showed with the self-debonding method, even at the minimum applied displacement of 0.1 mm where the crack was first formed the final gain spectrum showed a clear single peak. Therefore where the pre-debonded length in this cable embedment method is equal or longer than L_{SR}, the gain function is constructed with optimum accuracy.

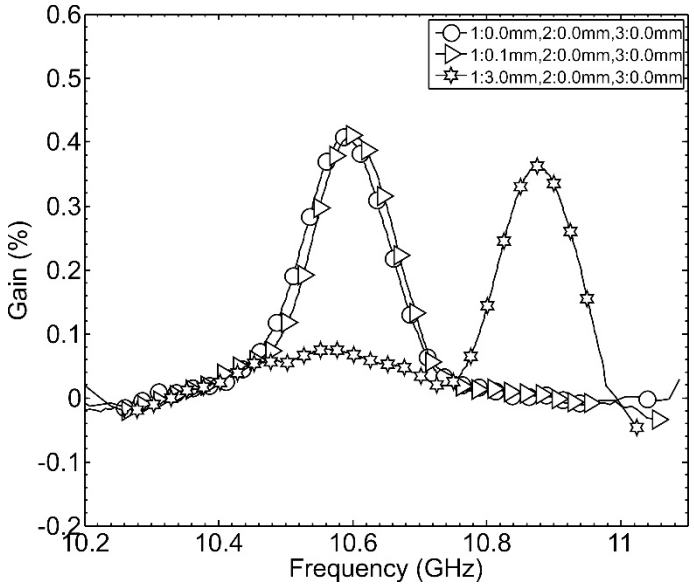

Figure 4-15. BGS for point P1 shown in Figure 4-14 peaked at its maximum amplitude whether at low or large crack opening. Curves in a has been smoothed for the sake of better presentation.

Figure 4-16 shows the $\Delta\nu_B$ with applied microstrain at three different points located in the middle of each interval, indicated as P_1, P_2, and P_3 in Figure 4-14. These graphs are different from their corresponding ones for the test shown in Section 4.5.1 with the self-debonding cable embedment method. For this figure, since the strained length was already known and constant, strain instead of displacement was considered against the frequency change. As shown in the figure, the frequency changes registered at all three points perfectly follow the linear best-fit from the beginning to the end of the applied strain.

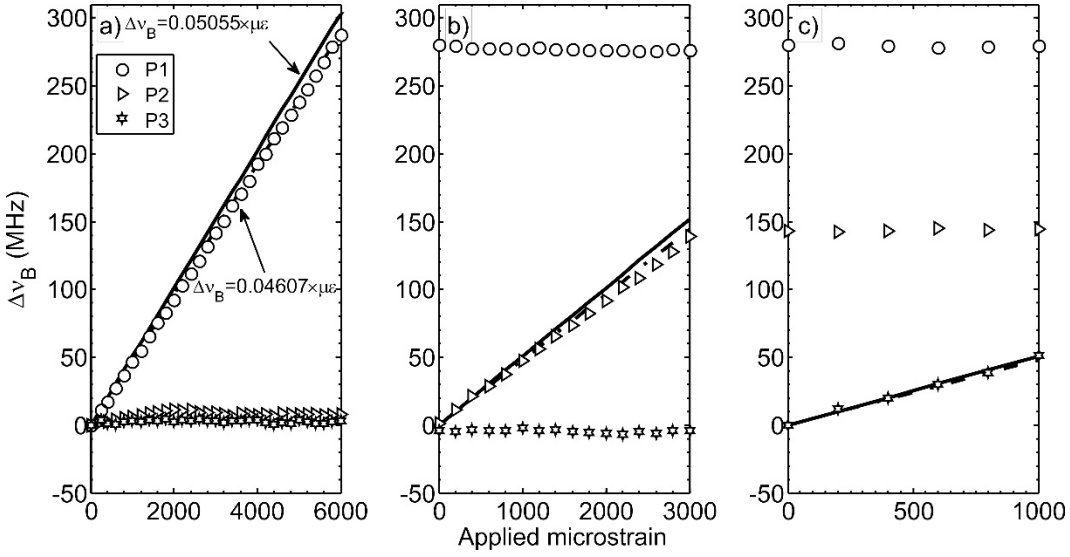

Figure 4-16. $\Delta\nu_B$ against applied strain for three points at the middle of each anchored interval at the first (a), second (b), and third (c) displacement steps showed good agreement with best-fit correlation lines

4.5.3. Anchor / joint spacing

In the test presented in Section 4.5.2, only one crack was induced and opened according to the displacement sequence over each anchored interval. So, the $\Delta\nu_B$ profile and its linear correlation with strain were purely influenced by this single crack. However, it is possible that there are several joints present within each interval, depending on either joint spacing or strained length (i.e. anchor spacing). For this reason, a beam with the high strength mortar mix was built and cured. The embedded sensing cable was anchored at two locations to ensure forming a strained length of 150 cm and it was coated with petroleum jelly before covering its entire length of the cable with a plastic heat shrink tube, similar to the debonding method used in Section 5.5.2.

Using the same setup, three cracks were induced within the beam every 55 cm over the pre-debonded anchored interval of 150 cm. For direct comparison, the same displacement sequence given in Table 4-2 for each moving plate was adopted. The main objective of this test was to understand how the DiTeSt™ would respond when strain localization occurred in terms of tensile cracking at several locations over a strained length (anchored interval) that was larger than the joint spacing.

A hairline crack was formed at each crack location at displacements below 0.1 mm. Figure 4-17a shows the $\Delta\nu_B$ relative to the initial unstrained beam along the length of the cable where it enters and leaves the beam. Solid horizontal lines show the expected frequency shift taking into account the actual applied strain based on a conversion factor of 0.4607 MHz/με - assuming the applied displacements are distributed over the entire debonded length. Upon movement of the first plate, even a 0.1 mm crack opening could be detected by the DiTeSt™ uniformly over the length of the anchored length. The profile over the strained length was almost uniformly flat with no localized peak at the crack locations.

Furthermore, Figure 4-17b-d give the variation of Brillouin frequency change with applied strain at the points indicated in Figure 4-17a, 50 cm separated from each other. The frequency variation at each of these three points followed quite closely the best-fit dashed line. It was noticed that where a perfect cable debonding from mortar occurs it would not matter how many joints exist over an anchored interval of the cable and in what order they open or close. The resulting profile would be an average of displacement at all joints over the strained length.

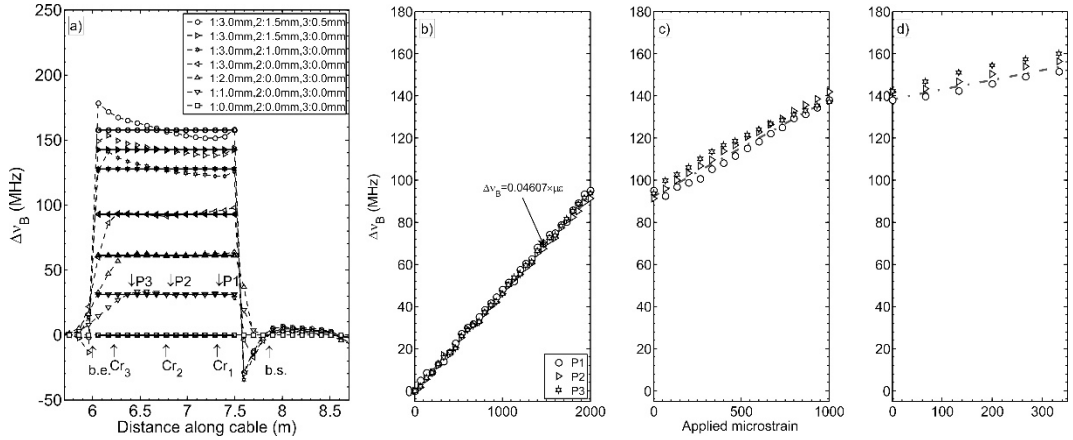

Figure 4-17. $\Delta\nu_B$ along the cable (a) and against the applied strain at three points (P_1-P_3) at the crack locations (Cr_1-Cr_3) at the first (a), second (b), and third (c) displacement steps for the 150 cm pre-debonded strained length of the cable. The strain profile is uniform and $\Delta\nu_B$ at all three points followed the best-fit with no preference. Solid horizontal lines in *a* correspond to the theoretical applied strain over the anchored length.

It is worth noting that the quality of the debonding was also an influential parameter on the DiTeSt™ efficiency, particularly in a case similar to this test when more than one joint meet the anchored interval. If a low quality cable-mortar debonding takes place, some strain localization would occur at crack locations resulting in a non-uniform frequency profile contrary to what is shown in Figure 4-17a.

4.5.4. Borehole diameter / filler thickness effect

In the context of structural health monitoring, fiber optic sensors have been attached to the surface of the structure using a protective coating. However, it has been found that the mechanical characteristics of the protective bonding component influences the strain transfer process from the host material to the fiber optic, since a portion of the strain would be absorbed by the coating layer (Ansari & Libo, 1998). Furthermore, Wan et al (K. T. K. Wan & Leung, 2007) showed that when a fiber optic sensor is bonded to the surface of a structure, the strain transfer process from the component of interest to the fiber optic sensor is influenced by additional factors such as bond length and thickness (K. T. Wan, Leung, & Olson, 2008).

Distributed optical fiber sensors in an underground mine with our monitoring objective (far-field small strain measurements and joint dilation) would be installed in a borehole. The borehole diameter is mostly controlled by the underground equipment availability and capability. The thickness of the filling material is a key factor in transfer of the rock blocks movement and joint opening to the sensing cable and should be assessed to see how, if at all, it affects the DiTeSt™ response.

To explore this, a mortar beam of 50.8 mm square cross section was built with the strong mix design (Table 4-1) and cured for one week. The cable was coated with petroleum jelly and was anchored at four points along 2 m of the cable to create three 50 cm pre-debonded intervals. The testing procedure remained the same as before. The displacement sequence given in Table 4-2 was followed and a tension crack was formed at each crack location at a displacement below 0.1 mm.

Figure 4-18a shows the Brillouin frequency change, $\Delta\nu_B$, profile along the cable length (the cracks and beam end points have been indicated). Generally, the profile shapes are identical to those obtained with the smaller diameter beam. Further details could be noticed by plotting $\Delta\nu_B$ against applied microstrain at each crack location at points P_1 to P_3, as shown in Figure 4-18b-d. It was found that the frequency change at these points at the middle of strained intervals perfectly followed the best-fit curve. The method used for cable embedment is certainly a key component in the cable response in this test, i.e. as long as the cable is debonded from the mortar, the thickness of the surrounding filler material in the borehole would not influence the sensing performance of the DiTeSt™.

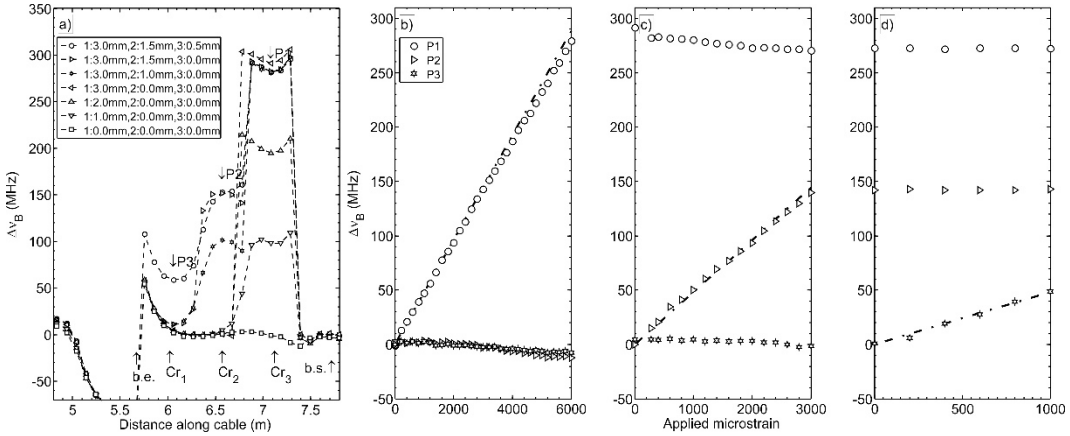

Figure 4-18. $\Delta\nu_B$ along the cable (a) and against the applied strain at three points at the crack locations at the first (a), second (b), and third (c) displacement steps for the thicker mortar beam did not show any difference with those with the smaller thickness beam

4.5.5. Filler material strength effect

In Section 4.5.4, it was explained that the mechanical characteristics of the bonding material could affect the strain transfer process. When backfilling the borehole with grout mix, its engineering properties should be accurately determined to confirm the conformance between the fiber and the surrounding rock (Dunnicliff, 1993). The mixing procedure plays an important role in the grout properties, and the ratio of water to cement is a key parameter for control of the grout strength.

It appears best to design a grout mixture for a borehole instrument to match its strength and deformation properties with the surrounding rock mass (Dunnicliff, 1993; Mikkelsen, 2002). For an extensometer installation, it is better to use a grout type less stiff than the surrounding rockmass. This is so because if the stiffness of the grout is much larger than the rock, the deformation is mostly absorbed by the grout and less axial displacement would occur in the grout than the rock. For an inclinometer measurement, it is recommended to use a stiffer grout than the nearby rock to provide enough lateral confinement (Mikkelsen, 2002).

To study the effect of the mortar strength on the measurement performance, the strength was reduced with decrease in the cement portion from 2.4 to 1.2 kg (weak mortar mix in Table 4-2).

One beam was cast with the cable anchored with 50 cm spacing and pre-debonded from mortar, and the same displacement steps for previous tests were adopted to induce three cracks over each anchored interval.

From Figure 4-19a, it was noticed that the frequency profile shape was identical to that in the test with stronger mortar beam. Furthermore, from Figure 4-19b-d, the Brillouin frequency shift change at three points in the middle of three anchored intervals closely followed the best-fit correlation. The results shown in this figure imply that with this method of cable embedment in the mortar, the mortar strength has no noticeable effect on the strain transfer process because the cable is fully debonded from the mortar along its length. With this installation method, the more important characteristics of the filling are the tensile strength as well as its placement performance in the borehole to fully cover the anchors.

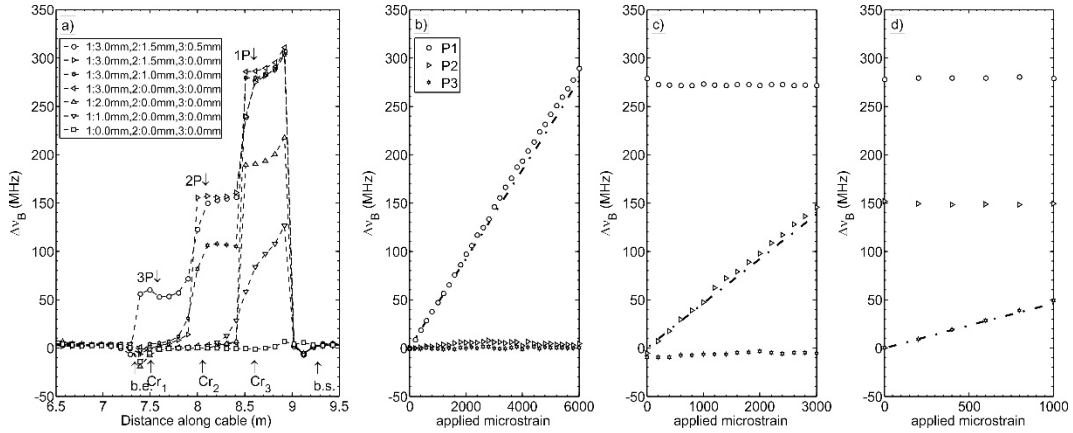

Figure 4-19. $\Delta\nu_B$ along the cable (a) and against the applied strain at three points at the crack locations at the first (b), second (c), and third (d) displacement steps for the weak mortar beam with the 50 cm spaced anchored cable showed the same performance as was noticed with the stronger mortar beam

5. DBS response under shear displacement

5.1. Introduction

In Chapters 3 and 4, DiTeSt™ was evaluated for its repeatability, base noise level, the system response to simple stretching, and the ability of the system to discriminate successive strained intervals in both time and space domains. Since such sensors are to be installed in a borehole, an optimum borehole installation was established; accounting for filling strength and thickness, strained length, and joint spacing, as they might impact strain transfer processes from the rock mass to the sensor. These studies focused on the system response when the cable was under direct tension, a condition which cannot be always true in the field. In many circumstances they might experience shear displacement from joint displacement. A sensing cable installed in a borehole might also be strained under direct tension, direct shear, or a combination depending on the joint-cable orientation, driving stresses, block interlocking degree, and dominant deformation mechanism.

A comprehensive laboratory testing program for the DiTeSt™ response permitted assessment when the sensing cable (SMARTprofile™) was under shear displacement. Tests were designed to understand different aspects including the difference in response of DiTeSt™ in tension and shear displacement, effect of kink length and strained length, and the response when SMARTprofile™ experienced shortening rather than elongation during shear displacement. The effects of two joints moving in shear over a strained length and of shear displacement directionality on the recorded response were studied. Finally, the effect of a combined displacement mode including tension and shear was considered when the sensing cable passed a fracture obliquely rather than at right angle. This article presents shear test results as the last component of a comprehensive laboratory testing program on the DiTeSt™ system.

5.2. Methodology

5.2.1. Cable installation

For underground mining applications, since the displacement field evolution far from excavation is of concern, the sensing cable has to be installed in a borehole filled with appropriate grout.

To develop an appropriate installation procedure, tests were performed in two configurations. The cable was first fully embedded in a mortar that naturally debonded as a result of strain localization; then the cable was anchored at given spacing and pre-debonded over its length between each two anchors before embedment in the mortar. This procedure was developed based on results obtained with direct tension tests, as described in Chapter 4. The first method proved unsatisfactory because uncontrolled cable debonding occurred during deformation, making it difficult to interpret the DiTeSt™ responses.

An anchoring-debonding installation provides the flexibility to decrease the anchoring spacing to increase the sensitivity of the system in small displacement conditions or to increase it to distribute a large displacement over a longer sensing cable section to reduce the risk of cable breakage. Furthermore, since the anchor spacing is known, the registered frequency by the system can quantitatively be correlated to the joint movement. This method was adopted as the main installation method and is the basis for all experiments presented herein. It is worth noting that the minimum length that any localization event was detected by the DiTeSt™ was found to be half the spatial resolution (L_{SR}=50 cm, Table 2-1), i.e. 25 cm. Although it would have been possible to choose any length ranging from 25 to 50 cm for the anchoring spacing, we used primarily a 50 cm anchoring length (L_{SR}) to obtain good data.

5.2.2. Test procedure

A setup composed of three 50 cm square aluminum plates was built so that the setup has a length of 150 cm, three times longer than the spatial resolution (L_{SR}). The setup can accommodate movements over different cable lengths ranging from 1 mm to 140 cm. In addition to simulate the effect of single joint movement on the DiTeSt™, the setup has the capability to include two joints moving independently in the same or opposite directions. Furthermore, using the same test setup evaluation of shear displacements on the cable crossing at a relative inclination of 75° with joint trace was possible, apart from the test with cable normal to the joint. An inclined cable alignment allows study of mixed joint deformation mechanisms that result in both shear and tension on the cable.

For most tests the strained length was set at 50 cm, although tests on two more lengths including 100 and 140 cm were performed for cases where two joints are present over the strained length. One plate was permanently fixed (left plate in Figure 5-1), the others could move individually and were monitored using digital displacement gages.

In Figure 5-1, components named “kink guide” can be seen at each side of the joint surfaces (i.e. the border of each plate); these were added to the setup to study the effect of kink length on the behavior of the DiTeSt™ readings under shear displacement. The maximum shear displacement was different for various tests according to the kink length adopted for each test. The application of displacement to the cable was done mechanically using 10 cm long bolts (moving/stopping blocks in Figure 5-1), to apply movements as small as 0.001 mm. The sign convention for displacement direction is shown by black arrows in Figure 5-1: “+” corresponds to elongation and “–“ represents shortening due to shear displacement. The temperature was stable throughout testing.

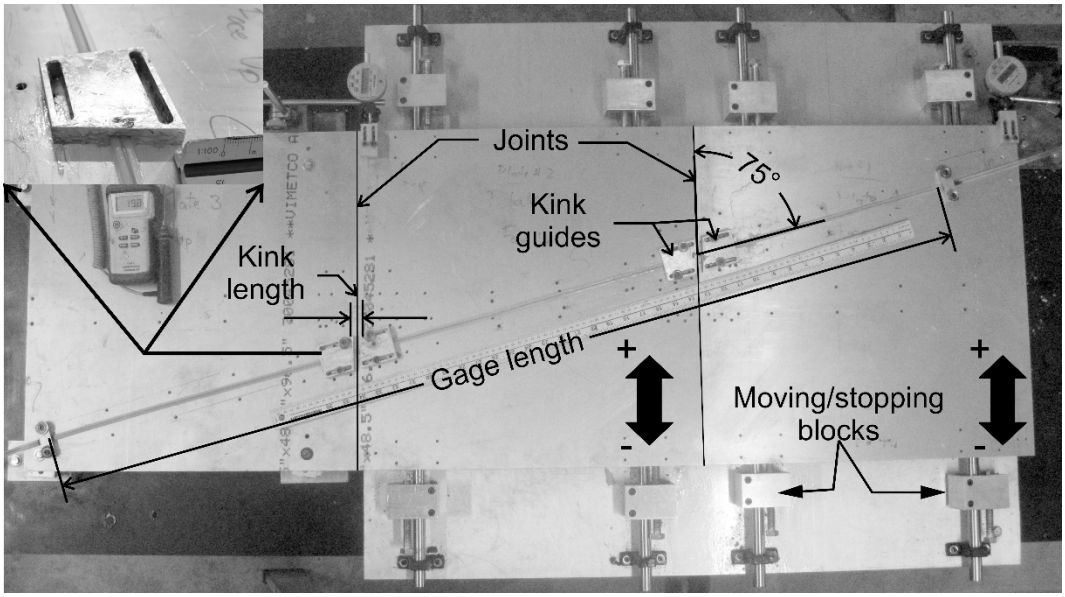

Figure 5-1. Test setup for shear displacement composed of two moving (middle and right) and one fixed plate (left). The setup allows for direct shear (sensing cable perpendicular to the shear movement) and combined shear-tension (oblique cable as shown) as well as the consideration of the effect of the kink length. The inset on the top left shows a magnified view of the kink guide used to simulate kink length. It has a slot with a dimension slightly larger than that of the cable.

5.3. Tests involving a single joint

Tests involving a single joint were performed first and are presented in the following Sections.

5.3.1. Effect of strained length

Tests on the SMARTprofile™ under shear displacement were realized by clamping a certain length of the sensing cable at both ends to the linear moving plates at right angles to the joint trace. The whole length of the clamped section, referred to as strained length (l), is involved when shear displacement is applied. The strained length was varied from 100 cm to 1 cm. Figure 5-2 shows the Brillouin frequency shift change, $\Delta\nu_B$, along the sensing cable length when the applied shear displacements to each strained length induced a $\Delta\nu_B$ equivalent to 0.5% axial strain, i.e. $\Delta\nu_B$=0.04607(MHZ/με)×5000(με), where 0.04607 is C_ε obtained from direct tension test results on the cable. All strained lengths ≥ 40 cm showed a frequency change equal to 5000με. Although the 30 cm strained length showed a clear frequency response, occasionally this strained length did not yield any response to shear displacement, making it an unreliably small strained length for applications. Furthermore, the system never showed any response for the lengths $l<L_{SR}/2$. This is consistent with the results from extensional tests on the cable (Madjdabadi et al., 2016).

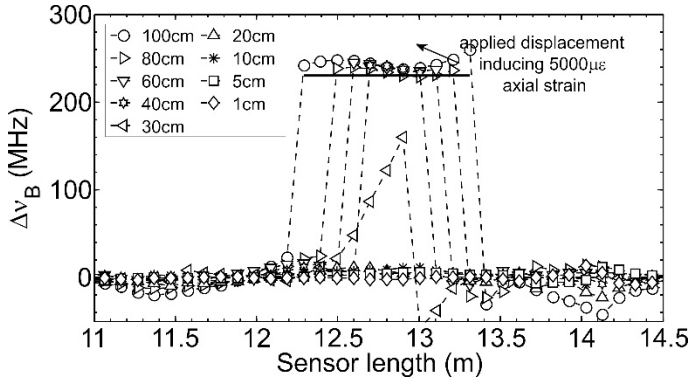

Figure 5-2. $\Delta\nu_B$ profile along the sensing cable for 9 different strained lengths when various displacements equivalent to 5000με axial strain are applied to clamped sections. All lengths above 30 cm registered frequency change.

Figure 5-3a shows $\Delta\nu_B$ averaged over the strained length against applied shear displacement for all the strained lengths tried in this test. Also, $\Delta\nu_B$ results from direct tension on the same strained lengths of the cable are shown in Figure 5-3a indicated by "Direct tension". An important feature of these plots is a parabolic relation between $\Delta\nu_B$ and shear displacement for each strained length. This is in contrast with the linear correlation between $\Delta\nu_B$ and extensional displacement during direct tension tests on the cable (Madjdabadi et al., 2016). For a given strained length in a perpendicular shear displacement configuration, 20-40 times more displacement than in direct tension is required to induce a certain $\Delta\nu_B$ in the system. It is intuitively understood that the displacement mechanism and slip magnitude of all individual fractures are not actually known. However, where a rough estimate of dominant displacement is feasible the different system response in applied displacement can be used to discriminate between direct shear, direct tension, and combined displacement modes. The relationship between $\Delta\nu_B$ and displacement will be explained in Section 6.3.6.

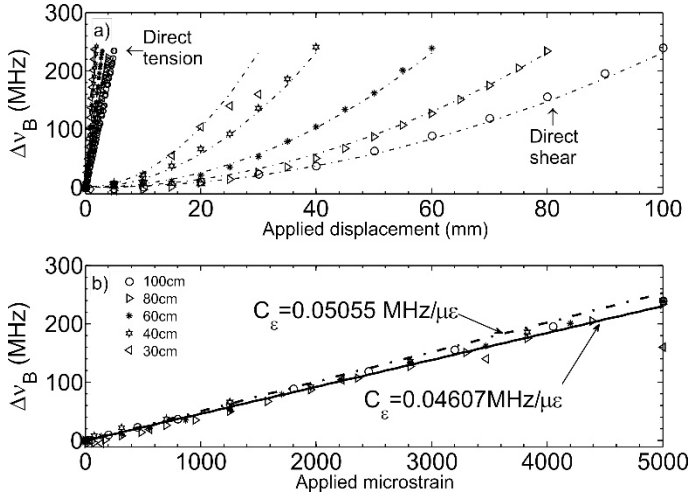

Figure 5-3. a) $\Delta\nu_B$ changes in parabolic trend with shear displacement in comparison with the linear correlation from direct tension tests, b) $\Delta\nu_B$ shows linear dependency with the displacement-converted strains as compared with manufacturer's data (0.05055 MHz/με) and we propose (0.04607 MHz/με) best-fit correlation coefficients

While the above statement is true, Δv_B is directly correlated to the applied strain, not displacement. Only if the strained length is known can it be linked to the displacement (if the cable is uncontrolledly self-debonding from grout the strained length would not be known). Accordingly, Δv_B due to shear displacement was plotted against induced strain in the cable, as shown in Figure 5-3b. The average strain in the cable under lateral movement was computed with Eq. 6.1, proposed by Newmark and Hall (Newmark & Hall, 1975) for soil-buried pipelines intersected with a right lateral strike-slip fault at an angle α≤90° in which tensile strain is induced in the pipe, as shown in Figure 5-4. In their solution the pipe is assumed to be strongly bonded to the soil, i.e. no relative displacement between pipe and soil. They also did not consider the lateral interactions at soil-pipe interfaces. In the formula, the total elongation of the pipe includes two components; one is due to longitudinal fault movement ($D_s \cos\alpha$), the other to the arc-length effect induced by the lateral fault movement ($D_s \sin\alpha$):

$$\bar{\varepsilon} = D_s \cos\alpha / 2L_a + \left(D_s \sin\alpha / 2L_a\right)^2 / 2 \qquad (3.2)$$

L_a (L_a=l/2) is the distance between the fault trace and the anchor point shown in Figure 5-4. In this equation, it is assumed that both the axial and transverse effects influence the same horizontal distance La from the fault. Since the distance over which bending strains is significant is usually smaller than that for axial strains caused by longitudinal components of fault movement, this assumption is not conservative. In the case with the sensing cable running perpendicularly to the joint (α = 90°), the equation reduces to Eq. 5.2:

$$\bar{\varepsilon} = \left(D_s / 2L_a\right)^2 / 2 \qquad (3.3)$$

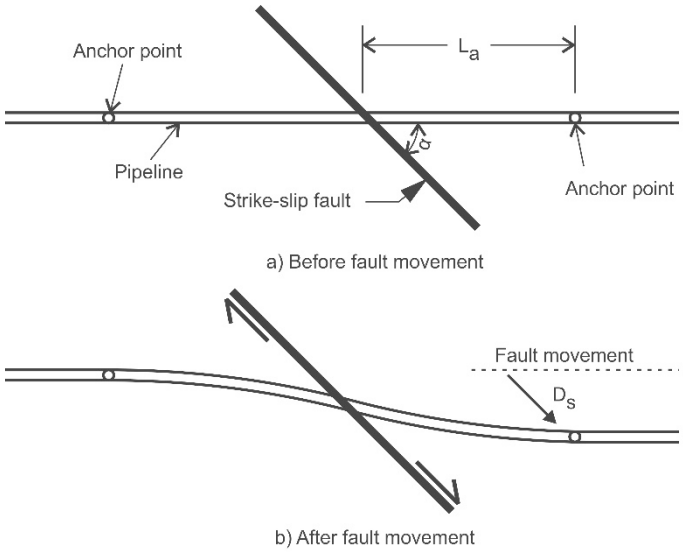

Figure 5-4. Plan view of Newmark-Hall model for a pipeline crossing a right lateral strike-slip fault at angle α≤90° where a tensile strain is induced over the anchored length (2L_a). they assumed that both longitudinal and transverse component of the fault movement occurs over the same length, a non--conservative assumption (modified from (Newmark & Hall, 1975)**))**

Figure 5-3b shows that the Δv_B plotted against induced axial strain for all strained lengths in the cable follows a linear trend. Their linear relationship closely corresponds to the best-fit correlation line obtained for the direct tension (solid line). This testing configuration would not represent a

cable placed in a borehole filled with stiff grout, but the case when the cable is attached to the surface of rock mass or when it is embedded in the soil to detect a potential shear surface movement. In the case of stiff grout, grout will break at the fracture location whether in tension or shear. Therefore the cable cannot freely and laterally move in the grout in the case of shear displacement, but will experience a kink at the immediate distance of the crack in the grout. In the next section, the system response is discussed when a kink in the cable occurs.

5.3.2. Kink length

The cable embedded in the relatively stiff grout will deform in a kink shape at a fracture location moving in shear. This kink creates an S-shaped distortion with two breaking points at each side of the fracture where the cable lateral displacement is restricted. The distance between these two points may vary depending on the grout strength and cracking mechanism. When the grout strength is high enough and it breaks at a single crack aligned with the pre-existing fracture, similar to the sketch shown in Figure 5-5a, these two points will be located at the immediate vicinity of the crack resulting in the shortest possible kink length and probable damage to the sensing fiber. When the grout strength or cracking mechanism causes disintegration of the grout in the vicinity of the fracture, then the cable will kink at two more distant points, shown in Figure 5-5b.

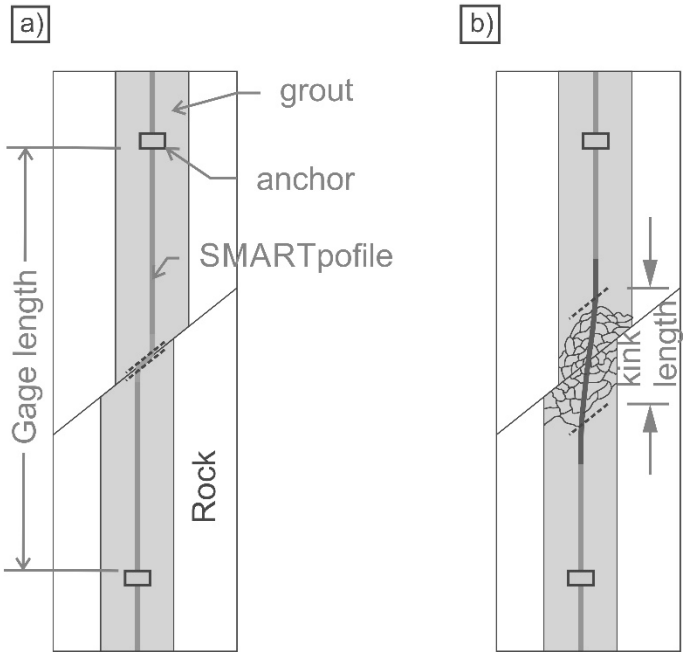

Figure 5-5. A schematic sketch where the sensing cable at a joint location crossing a borhole under shear displacement might experience very short (a) or longer (b) kink length depending on the grout strength and deformation mechanism

While the strained length, l, at both cases shown in Figure 5-5, is fixed and equal, only the kink length varies. It is expected that variation of the kink length (L_K) for a fixed strained length would influence the strain sensed in the cable. Shear tests were therefore performed on the sensing cable using the same setup with additional components as kink guides. These guides (Figure 5-1) have a slot slightly larger (~0.65 mm) than the cable cross-sectional area to serve as a guiding path.

Lubricant gel was applied at the cable and guide locations to ensure that the cable can freely slide in the guides. Apart from the strained lengths, six kink lengths including 1, 5, 10, 20, 50, 100 mm, were considered. The shear displacement was then applied as much as feasible in order not to break the cable with respect to the smaller radius of curvature for the shorter kink lengths (based on the manufacturer's recommendations).

Figure 5-6 presents $\Delta\nu_B$ for three kink lengths including 1, 10, and 20 mm and for two different strained lengths of 50 and 140 cm. Also, the location of the clamps and kink guides along the cable for each test is shown in the figure. A 3 mm shear displacement for given kink lengths was used for the sake of comparison. This displacement was actually the maximum permitted shear displacement applied to the cable with 1 mm kink length. For both strained lengths, it is noticed that the presence of shortest kink length, i.e. 1 mm, could result in a slightly higher $\Delta\nu_B$ over the strained length, although this was more noticeable at higher displacements. Moreover, the same shear displacement induced less $\Delta\nu_B$ along the strained cable when the kink length increased. This was more prominent at the kink guide locations, where the registered frequency along the strained length was slightly higher.

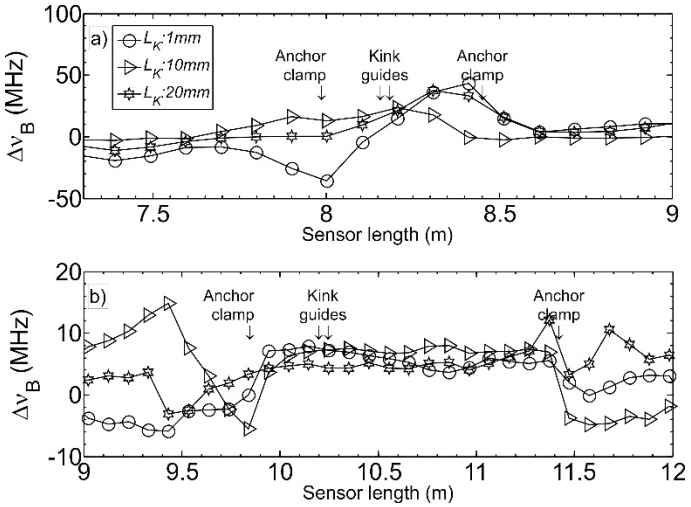

Figure 5-6. $\Delta\nu_B$ along sensor length for 50 cm (a) and 140 cm (b) strained lengths for three different kink lengths after 3 mm shear displacement. Although the same D_S applied to all test configurations, registered $\Delta\nu_B$ are slightly different among the results from all kink lengths

The frequency change averaged over the strained length for all kink lengths is plotted against applied shear displacement for the same strained lengths (Figure 5-7). Error bars represent the range of measurement variability (3 std. dev.) due to instrumental noise (Madjdabadi et al., 2016). It was also found that $\Delta\nu_B$ for this test series followed the parabolic trend with shear displacements for each kink length similar to those shown in Figure 5-3, although more variability in the data is noticeable. Due to this parabolic behavior, it would be challenging to differentiate DiTeSt™ frequency response among all kink lengths at low shear displacement, but this issue was alleviated as shear displacement increased, where $\Delta\nu_B$ for various L_K diverged from each other.

An inclined solid line in each sub figure, which shows the frequency change with axial displacement obtained from direct tension tests for the same strained length, was added to the figure for the sake of comparison. It can be seen that for the given kink lengths, the required shear displacement to induce a certain $\Delta\nu_B$ in the sensing system ranges between 10-40 times more than the axial displacement. According to Figure 5-7, therefore, the Brillouin frequency change varies not only with strain, but also with kink lengths. The dashed curves in Figure 5-7 represent best mathematical fits to all data sets, to be discussed later.

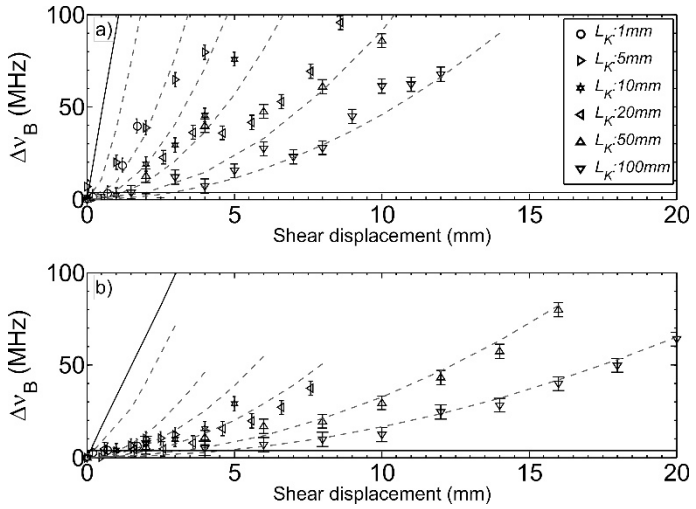

Figure 5-7. $\Delta\nu_B$ against 50 cm (a) and 140 cm (a) strained lengths. The $\Delta\nu_B$ for each kink length varies in a parabolic trend. The smaller the kink length, the higher the $\Delta\nu_B$. Dashed curves are the theoretical fits based on a triangle approximation. The horizontal solid line and error bars represent the base noise level of the system. The solid inclined line in both a and b correspond to the theoretical correlation between $\Delta\nu_B$ and extensional displacements for each strained length

Furthermore, the cable experiencing a shorter kink length showed a higher frequency change at smaller shear displacement, but the maximum shear displacement was restricted in accordance with the kink length, i.e. smaller displacement for shorter kink length. This is because with a shorter kink length a shorter radius of curvature is applied to the cable so that the cable will break at a certain displacement. Considering tests with 50 cm strained length, any frequency change induced by shear displacements ranging from 1 to 2 mm was detected for all kink lengths according to the base noise level (the horizontal black solid line in Figure 5-7), whereas for the 140 cm strained length, the detection occurred at displacements between 2 and 3 mm. This implies that in the case of longer strained lengths, a cable crossing a joint under shear movement causing shorter kink lengths might be broken even before DiTeSt™ could register any response; a result that may affect the selection of anchor spacing along the cable.

5.3.3. Relative inclination of the cable

With the borehole installation, the sensing cable can meet joints at any inclination depending on the borehole and joint orientations. Depending on the rock block displacement mechanism including separation or shear on joints surface, the cable might experience direct tension, direct shear, or a combination of both. Therefore, the relative orientation between sensing cable and joints should be taken into consideration when interpreting the results from DiTeSt™. The relative

inclination was explored using the same setup as in the direct shear displacement test where the cable crossed a discontinuity at 75°, as shown in Figure 5-1. The strained length was set at 50 cm with kink lengths ranging from 1 to 50 mm. The displacement, varying from 3 to 6 mm according to each L_K, was applied in the positive direction as indicated in Figure 5-1.

Figure 5-8a shows the Brillouin frequency shift change along the cable length after application of 3 mm displacement when the kink length increased from 1 mm to 50 mm as well as the case with no kink guides, i.e. L_K=l=500 mm. The profile shape shows a tendency of higher frequency to the left, where the kink guides were more closely located. As also noticed from the direct shear test, the shorter kink lengths in inclined shear testing caused higher frequency responses.

Figure 5-8b presents $\Delta\nu_B$ plotted against the applied shear displacement for all kink lengths. Dashed lines represent the theoretical fits to frequencies obtained similar to those in Figure 5-7, to be discussed later. There is a clear difference between frequency response from direct and inclined shear tests: DiTeSt™ in the current cable-joint configuration could register frequency responses above base noise level at much lower displacements compared to the 90° direct shear test.

It should be noted that even the slight rotation of 15° from the direct shear condition caused a significant difference in DiTeSt™ response. Results from Figure 5-8b showed that with the inclined cable sheared with a kink length equal to the strained length, i.e. L_K=l=50 cm, a higher $\Delta\nu_B$ (axial strain) was registered in comparison with the cable in direct shear configuration even with the smallest kink length, i.e. 1 mm. Although the frequency values still followed a parabolic trend, a linear trend was also noticed over the course of displacement. This was because the longitudinal component contribution to the displacement in axial strain increased with introduction of the relative inclination. The DiTeSt™ response showed a steady transition from direct shear toward direct tension tests. Comparing Figure 5-8b and Figure 5-7, it can be seen that the frequency response in the current test for all kink lengths showed less discrepancy, specifically at higher displacement, whereas frequencies became more divergent with shear displacement in direct shear. This is as a result of the arc-length effect having less influence on the axial strain.

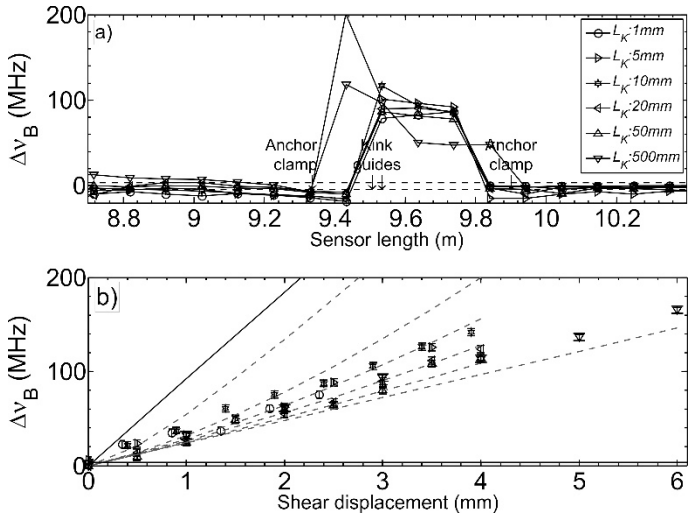

Figure 5-8. $\Delta\nu_B$ along sensor length (a) and versus shear displacement for inclined shear displacement tests (b). Longitudinal component of the shear displacement became more prominent and brought the parabolic trend observed in direct shear test to a more linear trend

5.3.4. Sensor directionality

SMARTprofile™ fiber optic sensing cable has a rectangular cross-section (Figure 5-9-a). There are two points that should be noted considering this geometry with respect to the direction of shear displacement.

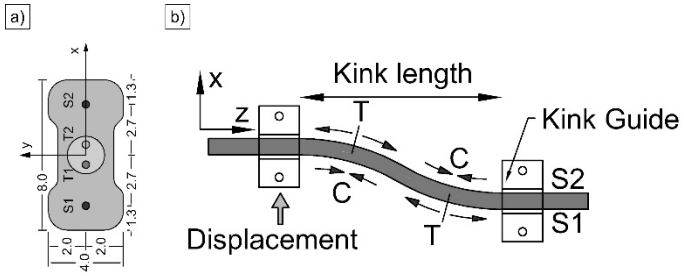

Figure 5-9. a) Dimensions of SMARTprofile™ (in mm) and b) different strain types applied to sensors S1 and S2 at the kink location; C: compression, T: tensile

The two strain sensors S_1 and S_2 are laid out in the y=0 plane symmetrically at the same distance from the y axis. It was thought that when the cable experiences shear displacement in a way that it bends about the y axis (Figure 5-9-a) sensor S_1 might show higher frequency response at sampling points closer to the right kink guide in Figure 5-9-b where the S_1 is more under tension, while this was the same for S_2 at locations closer to the left kink guide. On the other hand, it was expected that both strain sensors would register similar responses when the cable was bent about x axis at the kink location during shear displacement.

Figure 5-10 presents the frequency response along the length of the cable for both sensors S_1 and S_2 where 140 cm of the cable experienced lateral displacement about y and x axes. According to this figure, there was no significant difference between the frequency profile shapes of both S_1 and S_2 sensors whether the cable is bent about y or x axes at the kink location Therefore, the

frequency profile shape from both strain sensors could not be used to identify the shear direction at the joint location.

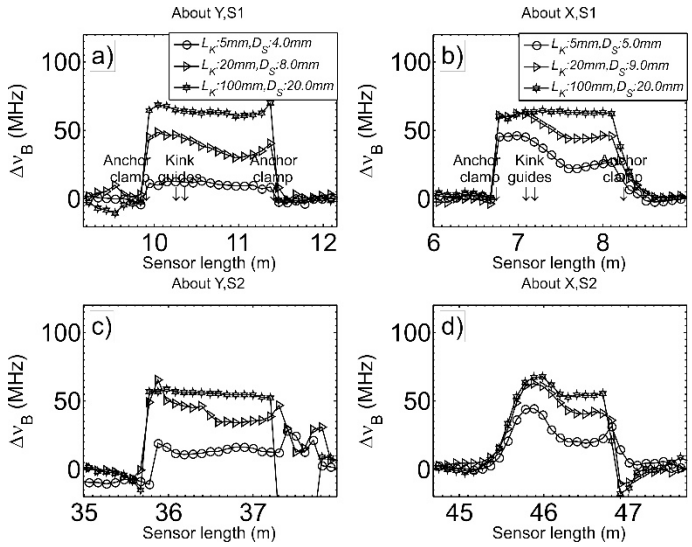

Figure 5-10. $\Delta\nu_B$ along both S1 (a and b) and S2 (c and d) sensors of SMARTprofile™ when it is bent about x and y axes (Figure 5-9) due to shear displacement. Shear about each axis resulted in similar frequency profiles along S1 and S2 sensors.

In addition, it was expected that DiTeSt™ might register lower a frequency change when the cable was sheared about the *x* axis rather than the *y* axis because the flexural stiffness (*EI*, where *I* is the second moment of area and *E* is young's modulus of the PE jacket) of the cable bent about the *y* axis is four times that about the *x* axis (Figure 5-9).

Figure 5-11 shows the average registered frequency over the strained length (Figure 5-10) for both cable configurations bending about *y* (white solid markers) and *x* (black solid markers) axes. It was found that the system response was generally quite repeatable with either cable configuration under shear displacement. However, the statistical comparison of results from both cable configurations showed that there was a relative mean difference of 5%, which is within the base noise level of the system and consequently can be ignored. Such a small difference might be due to the relatively short kink length compared to the minimum spatial resolution, L_{SR}=50 cm, of the DiTeSt™. The arc section of the sheared cable located within the kink length could contain only one or at most two sampling points (sampling interval, L_{SI}=10 cm). Since all sampling points over the L_{SR} contribute to the final registered profile at a given point, any difference in the frequency response of the system over the kink length from these two cable configurations would not cause a noticeable difference, i.e. the cable cross section-shear direction has minimal effect on the average frequency over the strained length.

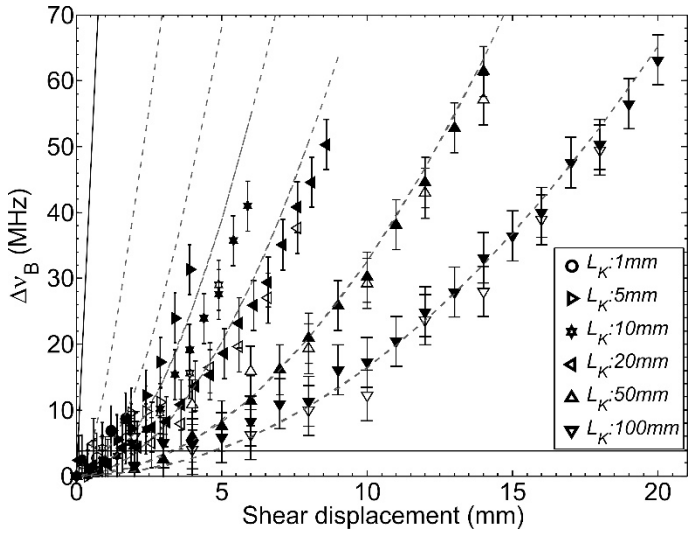

Figure 5-11. $\Delta\nu_B$ against shear displacement for the sensing cable under shear displacement about y (white markers) and x (black markers) axes for various kink length showed less than 5% difference

5.3.5. Theoretical fits

The dashed curves in Figure 5-3a were fitted to data through the Newmark and Hall formulation (Newmark & Hall, 1975). The results from the tests without adding kink guides, whether in direct or at inclined shear tests, showed good agreement with the Newmark-Hall relation, since in the test the anchored cable could freely displace laterally. This testing condition actually corresponded to their assumption in computation of the equation where the pipe could have significant lateral displacement away from the fault trace.

Furthermore, they neglected the effect of interaction of soil-pipe interface, so with their formulation the arc-length effect occurred over the same length as the longitudinal component of the strain, whereas in a real case the former length is much shorter. In the case of a cable embedded in grout the lateral displacement at each side of the fracture is considerably constrained resulting in a kink shape formed in the cable (Figure 5-5). Therefore, their approximation of average longitudinal strain cannot take the effect of kink length into consideration.

Before deriving the exact solution for the axial strain where the arc-length effect has a length much shorter than the longitudinal component, it is worth describing the exact relation from which the Newmark-Hall formulation was approximated. Their formulation is based on a simple triangle approximation, as shown in Figure 5-12-a, so the average elongation of the cable can be computed through the Eq. 5.3:

$$\overline{\varepsilon} = \sqrt{D_S^2 + L_G^2 + 2L_G \cos\alpha} - L_G \Big/ L_G \qquad (3.4)$$

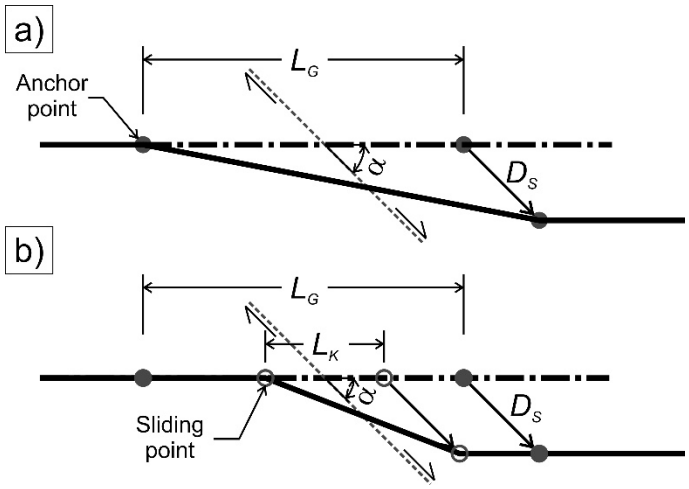

Figure 5-12. Triangle approximation of the elongation of a cable under shear displacement where the transverse component of the displacement is effective over the strained length (a) and over the kink length (b)

Considering that the transverse component of the axial strain occurs over a shorter length, i.e. L_K in Figure 5-12b, the exact solution for average strain in the cable can be obtained through Eq. 5.4:

$$\bar{\varepsilon} = \sqrt{D_S^2 + L_K^2 + 2L_K D_S \cos\alpha} - L_K \Big/ L_G \qquad (3.5)$$

It should be noted as L_K increases to equal l, Eq. 6.4 reverts Eq. 6.3. Therefore, the DiTeSt™ response will be a function of shear displacement (D_S), strained length (l), relative inclination (α), and kink length (L_K), i.e. $\Delta\nu_B = C_\varepsilon \times f(D_S, l, L_K, \alpha)$. The dashed curves shown in $\Delta\nu_B$-D_s figures are then according to Eq. 5.4.

5.3.6. $\Delta\nu_B$ - displacement

The importance of these fitted curves to the registered $\Delta\nu_B$-displacement is explained through Figure 5-13. In the field, when a single fracture meets an anchored interval of the cable (Figure 5-13b), upon movement of the fracture the only available data would be the Brillouin frequency shift change over time with respect to the first measurement gained after the system installation, as shown in Figure 5-13a. Therefore the $\Delta\nu_B$ data along the cable will provide the first symptoms of any change over an anchored interval. The frequency change data can then be used to build knowledge about strain localization occurring at any anchored interval. It is known (Luc Thévenaz, 2010) and also verified from the tension test on the cable (Madjdabadi et al., 2016) that the Brillouin frequency shift change varies linearly with strain ($\Delta\varepsilon$) and temperature (ΔT) changes. So, one can plot $\Delta\nu_B$ at the middle of the interval (or average of strain over strained length) for all measurements, Figure 5-13a, on the pre-established linear fit for $\Delta\nu_B$-microstrain. The variation of strain over time for any anchored interval can be followed using this plot to better study the distribution of strain localizations and their variation, as shown in Figure 5-13c.

This level of knowledge can be further enhanced where the amount and type of displacement can be evaluated but this is more challenging than strain determination. Whereas in the strain graph

(Figure 5-13c) there is a one-to-one correspondence between frequency and strain, the registered frequencies are required to be aligned with any of the theoretical fit curves established between $\Delta\nu_B$ and tension or shear displacement according to the strained length, kink length, and the relative angle between fracture and cable (Figure 5-13d). Therefore, it is necessary to reduce the number of unknowns (i.e. l, L_K, and α) to better approximate the displacement field. Using a fixed anchoring spacing along the cable, the strained length, l, would be known. Furthermore, from structural geology mapping along with borehole camera logging the inclination of the fracture could be determined. Knowing these two parameters, where the displacement field is extensional, i.e. fracture opening dominates, the strain localization at the joint location can be translated to its opening or closing. On the other hand, where deformation mechanism will involve a shear movement on the joint, the kink length, L_K, will remain unknown. Assigning an accurate value to kink length would be impossible; however, the kink length depending on the grout strength and cracking mechanisms (brittle or disintegrated) would likely vary on the order of a few millimeters to centimeters. Therefore, the displacement of a fracture could be roughly confined to a range according to theoretical fits established between $\Delta\nu_B$ and displacement for those kink lengths.

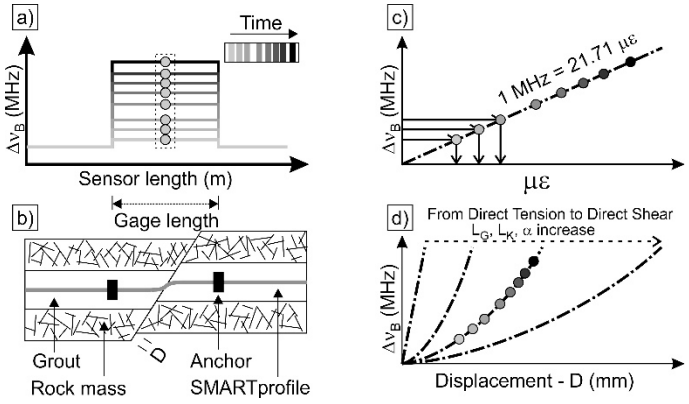

Figure 5-13. The Brillouin frequency shift change along the cable over time (a) for an anchored interval (b) can be used to understand the strain field variation (c). Where there are more data regarding strained and kink lengths, and relative joint-cable inclination is available, the displacement field evolution can be estimated (d).

5.3.7. Shortening vs. elongation

During previous tests described in earlier sections, the shear displacement was applied in a way that it induced extensional strain to the sensing cable in the cable-joint layout. This is also consistent with the assumption in the Newmark-Hall model (Newmark & Hall, 1975), where the strike-slip fault would cause axial tensile strain in the pipe for $\alpha \leq 90°$. However, in a rock mass there are situations where $\alpha > 90°$ (α is the relative inclination between joint trace and the cable) so that movement on the joint surface the cable might experience a compressive strain rather than elongation. Under these conditions, the cable would initially undergo a shortening phase followed by a stretching process, as in the case of the right joint in Figure 5-19a.

The response of the DiTeSt™ when shear displacement direction has resulted in a compressional strain was evaluated with the same cable configuration shown in Figure 5-1 with one exception; the displacement was applied in the negative direction. A 50 cm long section of the

cable was pre-strained to almost 3000 με and displaced to various amounts for three kink lengths of 5, 10, and 50 mm. If the pre-strain was not initially applied the cable would slip back through the guides and bend upward between each kink guide and clamp upon the movement of the setup plates because the guides did not cover the total strained length. This amount of pre-tension was high enough so that the cable did not reach an unstrained condition after applying the final displacement considered for each kink length.

In general, at a certain displacement before which the cable was experiencing shortening, the straining processes switches to elongation depending on the kink length and the joint-cable relative inclination and according to $D_{C\text{-}T}=2\times L_K/\tan\beta$, where $\beta=90-\alpha$, as shown in Figure 5-14. For the current test with three aforementioned kink lengths where $\beta=15°$, the simplified triangle approximation for displacement would be almost 2.7, 5.4, and 26.8 mm). These displacements are large enough to induce a break in the cable with the corresponding kink length. For example, once during the tests the cable with a 10 mm kink length broke at a displacement between 5 and 6 mm. So, displacements are kept small for the sake of cable integrity, and consequently the cable never entered an elongation phase following the shortening mode.

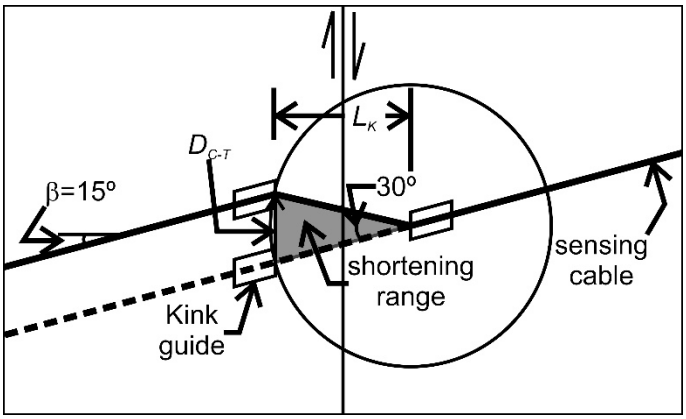

Figure 5-14. A schematic sketch of the test setup with the cable inclined at α=75° relative to the joint trace when shear displacement direction causes a shortening followed by an elongation in the anchored interval. The maximum shear displacement, $D_{C\text{-}T}$, required for transition from shortening to elongation phase varies depending on the kink length and joint-cable orientation

Figure 5-15a shows $\Delta\nu_B$ along the length of the sensor for these three kink lengths under different shear displacements when the cable was experiencing the shortening phase. In Figure 5-15a and similar figures, there are sometimes frequencies highly different from those in the middle of strained sections. These frequencies are located within $\pm L_{SR}/2$ (where L_{SR} is spatial resolution) of each clamp and are associated with short length events described in Madjdabadi et al (Madjdabadi et al., 2016). It is noticed that the frequency response with displacement showed a progressive decrease from the initial reading moving toward the negative side of the vertical axis. This response, as expected, was due to the relief of strain that was induced in the cable during pre-tensioning.

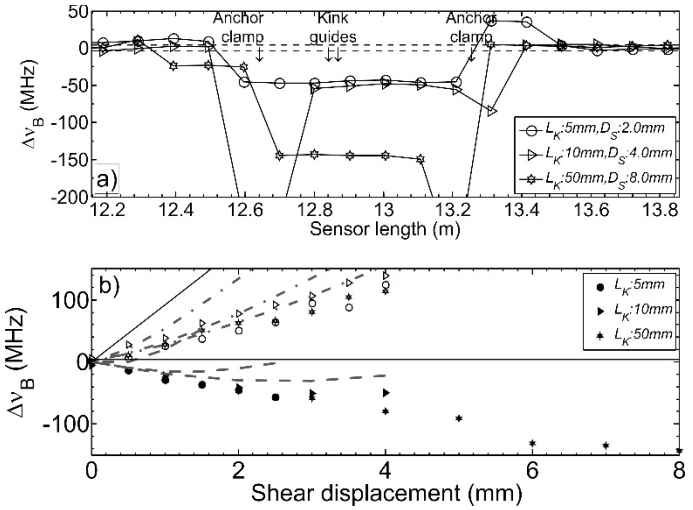

Figure 5-15. $\Delta\nu_B$ along sensor (a) and against shear displacement (b) for the shear test in which the cable undergoes elongation (white markers in b) and shortening (black markers in b). Pre-tensioned cable in a shortening shear displacement showed decrease in $\Delta\nu_B$ with respect to initial readings, but at a slower rate compared to an elongating shear test

Figure 5-15b presents the frequencies averaged over the strained length for the three kink lengths against shear displacement for test results with cable elongation (white markers) and shortening (black markers). It should be noted that the results for cable elongation tests under shear displacement are the same as those presented in Section 5.3.3 for comparison purposes. Similar to the results from the elongation-shear test where the frequencies increased with shear displacement in a parabolic trend, frequencies in the shortening-shear test seemed to follow the same trend with displacement, although slightly different from the former test. In this test, the parabola vertex shifted toward some positive displacements depending on a particular kink length. Although the frequencies up to some displacements after beginning showed a decrease, the negative slope of the graph gradually approached a plateau. It is expected that if more displacement were applied, the slope would finally become positive with $\Delta\nu_B$ increasing. This slope change was actually expected from Figure 5-14, where the maximum cable shortening occurred at $D_{C\text{-}T}/2$ and the cable returned to its original length at $D_{C\text{-}T}$ after which the cable enters its elongation phase.

In a strain-relieving process with the cable under direct tension, it is expected that loading and unloading paths correspond. However, since in the current testing configurations the applied displacement contained both longitudinal and transverse components, only the longitudinal component of the strain was relieved upon movement of the joint surface. While this component decreased, the strain due to the arc-length effect increased with displacement. This is the reason why the parabola vertex has shifted to positive displacements.

The dashed-dotted curves in Figure 5-15-b are graphed according to Eq. 6.4 for the elongation-shear test results. For the shortening-shear test, the dashed curves obtained through applying a small modification to Eq. 5.4 is as follows:

$$\overline{\varepsilon} = \sqrt{D_S^2 + L_K^2 - 2L_K D_S \cos\alpha} - L_K \Big/ L_G \qquad (3.6)$$

It can be seen that data do not show a strong agreement with the theoretical fit. Such a weak fit implies a more complicated behavior of the cable in compression, as stated by O'Rourke & Liu (O'Rourke & Liu, 2012) in the case of a pipeline under nominal compression by fault movement. However, it should be noted that a more accurate fit to the frequency results from shortening-shear test might not be even required since the sensing cable will definitely break at higher shear displacement, particularly with shorter kink lengths and in a shortening mode.

5.4. Deformation involving multiple joints

The DiTeSt™ response under shear displacement now has been evaluated when only one joint is present over the anchored interval, but it is likely that the strained length covers more than one joint depending on the jointing density of the rock mass and the anchor spacing. The anchored interval can contain at least one complete rock block with two joints over its length, so it would be expected that DiTeSt™ registers a Brillouin frequency shift profile which is the average of shear displacement of any of the rock blocks over the strained length. The sensing cable was anchored to the setup to explore this, such that the strained interval contained two joints, and the shear displacement was applied in two layout configurations: one with the cable under direct shear displacement and one with the cable under inclined shear.

5.4.1. Direct shear test

For the first test with the cable perpendicular to the joint trace, a 140 cm of the sensing cable was anchored to the setup plates and the lateral movement of the cable was restricted at two joint locations 50 cm separated from each other, as shown in Figure 5-16. The kink length at both joints was set at 10 mm to remove the effect of the kink length variation on the registered response.

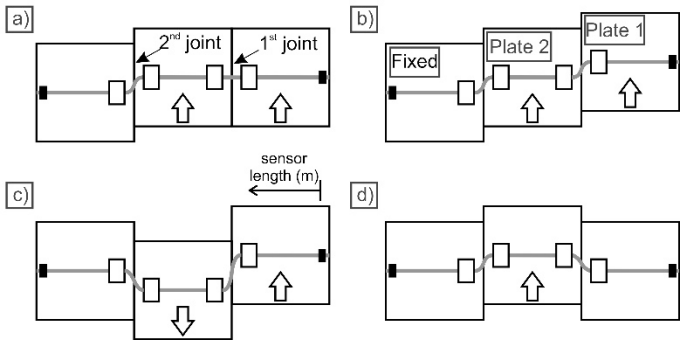

Figure 5-16. Four displacement scenarios adopted for movement of each of the two joints present along the anchored interval according to Table 5-1 . Kink lengths at both joints were set the same and kept constant during tests.

Since two joints existed over the anchored interval, there were four possibilities for shear displacement scenario. The first one was when the first plate was applied a certain shear displacement, then fixed, and followed by the same amount and direction of displacement to the second plate, Figure 5-16a. The second situation was considered when the two plates were displaced in the same direction with a certain linear gradient, Figure 5-16b. Next, a scenario was considered where each plate was applied equal amounts of displacement but in the opposite directions, Figure 5-16c. Finally, the first plate was kept fixed while the second plate displaced to

a certain amount, Figure 5-16d. The displacement sequence for each plate for all scenarios is summarized in Table 5-1.

Table 5-1. Four displacement scenarios and sequences applied to two moving plates

Scenario	Disp. sequence	1st plate	2nd plate
a	1	+6 mm	Fixed
	2	Fixed	+6 mm
b	1	+10 mm	+5 mm
c	1	+3 mm	-3 mm
d	1	Fixed	+5 mm

Figure 5-17 shows the Brillouin frequency shift change, $\Delta\nu_B$, along the sensor length for each scenario in Table 5-1. An interesting point about this figure is that various joint displacement paths could result in similar $\Delta\nu_B$, for example the 2 mm of shear displacement of each plate in the opposite directions in the third scenario (Figure 5-17c, triangles) provided almost the same $\Delta\nu_B$ as 4 mm shear movement of only the second plate in the last scenario (Figure 5-17d, triangles).

The Brillouin frequency profile shape for all scenarios over the course of displacement application was almost uniform along the strained length. However, there was a difference in the first scenario and the rest of scenarios due to the inherently different straining mechanisms. For all scenarios except the first one, the cable was progressively straining over the anchored length during movement of any of the two setup plates. On the other hand, with the first scenario the cable was not strained any more after movement of the first plate, but the strain was redistributed when the second plate started moving. This displacement sequence resulted in a strain relief at the first joint and strain buildup at the second joint. According to this displacement sequence, upon moving the second plate strain relief at the first joint reduced the frequency response until the redistributed strain at the second joint became high enough so that the frequency resumed its increasing trend, Figure 5-17a.

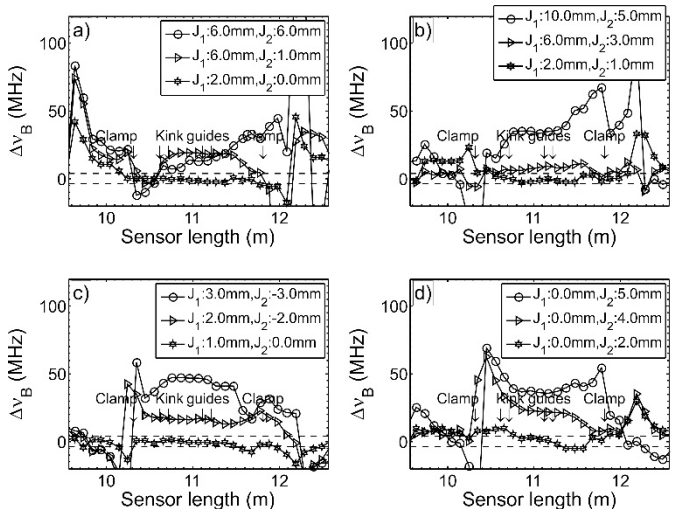

Figure 5-17. $\Delta\nu_B$ profiles for four shear displacement scenarios given in Table 5-1. It is noted that the same $\Delta\nu_B$ can be obtained from different displacement scenarios.

Test data were further analyzed by plotting the average $\Delta\nu_B$ over the strained length against the applied shear displacement. However, this case is different from the test with one joint intersecting the strained interval. While the average frequency change obtained from the one joint case test was simply drawn against shear displacement, it is necessary to understand which joint displacement should be used or how the contribution from each joint displacement should be considered in the current test configuration.

For the first scenario, the total shear displacement was the shear displacement at either first or second joints, i.e. 6 mm. In the second scenario, the relative displacement at first joint, i.e. 5 mm, should be added to that of the second joint, i.e. 5 mm, to obtain 10 mm total displacement. In the third scenario, the displacement at the first joint is not only from the first plate movement, i.e. +3 mm, but also the second plate movement, i.e. -3 mm, contributes to this joint displacement, which brings the total displacement at this joint to 6 mm. The total displacement for this scenario is then the summation of displacement at both joints, i.e. 9 mm (6 mm+3 mm). For the last scenario, since the first moving plate was kept constant, the total shear displacement is twice the displacement at the second joint, i.e. 10 mm (2×5 mm). After computation of the total shear displacement for each scenario, it is now possible to plot the $\Delta\nu_B$ against this parameter, as shown in Figure 5-18a.

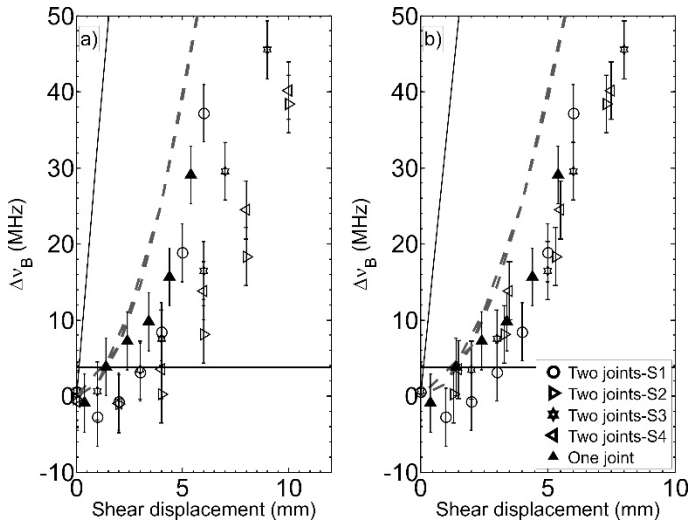

Figure 5-18. $\Delta\nu_B$ against applied shear displacement for four displacement scenarios of two joints (white marker) as well as one joint (black marker) before (a) and after (b) correcting displacement for larger dimension of kink guide in comparison with that of the SMARTprofile™

For comparison the result for the test where the same strained and kink lengths met only one joint is shown in Figure 5-18a (black triangles). In general, there is a good agreement between the results of two-joint and one-joint tests. However, there were small differences in the frequency changes among two-joint tests with particularly one-joint test results. The difference appeared as a delay in frequency buildup with shear displacement. The reason was thought to be a result of differences between cross-sectional areas of the kink guides and the sensing cable (inset in Figure 5-1); the kink slot was 0.65 mm wider than width of SMARTprofile™. Depending on how accurately every two kink guides are aligned, the sensing cable could have a free lateral displacement of 0.65-1.30 mm before it actually started straining in shear mode. The shear displacement value should be corrected for this amount since the sensing cable up to this movement has not yet become strained. Furthermore, since the current testing configuration included two joints, the free lateral movement for the cable at the kink guides was doubled, so the total shear displacement should be accordingly modified from 0.65 to 2.6 mm. Upon applying such a correction, the frequency results from two joint experiments showed even more agreement with that of one joint test (Figure 5-18-b). Furthermore, no frequency change profile for any of displacement scenarios increased to values above the base noise level for shear displacements below almost 4 mm (as shown in Figure 5-17), whereas after correcting the measurements for the free lateral movement, the frequency change could be first detected at a lowest 1.4 mm displacement.

5.4.2. Inclined shear test

Similar to the previous test, a section of 140 cm of the sensing cable was laid out on the same test setup so that it made a 75° angle with the joint trace, as shown in Figure 5-1, restricting the lateral cable movement with a 10 mm kink length at two joints. The last displacement scenario used in Section 5.4.1 was adopted for this test. However, the displacement sequence was slightly

different from what was done in the direct shear test. While the first plate was kept fixed, the second plate was moved first in the positive direction, Figure 5-19a, then returned to zero displacement followed by movement in the negative direction, Figure 5-19b. During positive shear displacement the cable at the second joint would be under tension (*T* in Figure 5-19a), whereas it would experience initially a shortening phase followed by an elongation period at the first joint (indicated as *C*-*T* in Figure 5-19a). When the movement direction changed to negative, it was expected to have a reverse response in each joint, i.e. the first joint under tension and the second joint face a compression then extension.

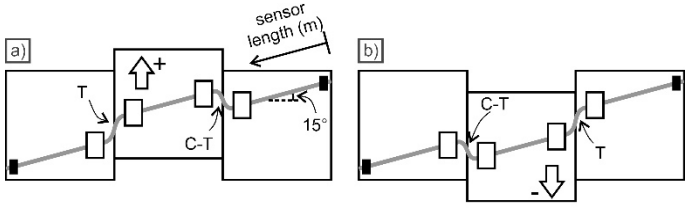

Figure 5-19. Schematic description of the inclined shear displacement with two joints over the strained length for the effect of shortening and elongation of the cable on the total registered frequency. If the second joint is under tension while the first joint experiences shortening, then elongation. This is in reverse order in b when the middle plate moves in the negative direction.

Figure 5-20 a and b presents the results for the test with shear displacement applied at positive and negative directions, respectively. According to the base noise level indicated by the horizontal dashed lines, the Brillouin frequency change could be detected at shear displacement as low as 1 mm. Although the kink guides used in this test had the same slot size as those used in the direct 90° test, less displacement was required in order for DiTeSt™ to recognize a frequency change along the sensor length. This was due to the effect of relative inclination of the cable with respect to the joint trace, since even small shear displacement in this configuration has a longitudinal component along the sensor axis.

The $\Delta\nu_B$ profiles also showed a tendency toward the joint which was always under tension during the entire displacement path. Therefore, the profile showed higher frequency around the second joint when moving the plate in positive direction (Figure 5-20a), while the frequency was higher close to the first joint during negative displacements (Figure 5-20b). Such a response to shear displacement direction resulted in almost mirror profiles when comparing the shear test results in both directions. Actually, as explained above and shown in Figure 5-19, the cable at the first joint in the positive displacement case became shorter in early stages of the displacement sequence. This shortening relieved a part of the total strain over the entire strained length.

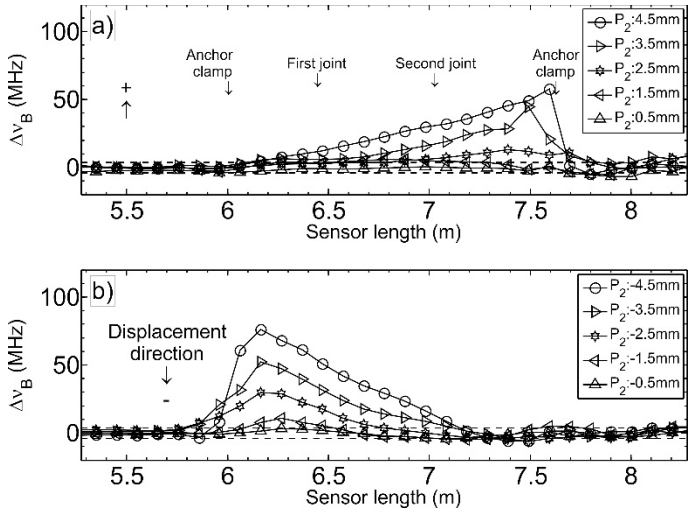

Figure 5-20. $\Delta\nu_B$ profiles for the effect of displacement direction on the cable when inclined at an angle with respect to joint strike and with two joints present over the strained length. The frequency profile when the middle plate in Figure 5-19 moves in + direction (a) shows a mirrored effect when it moves in – direction (b).

6. Conclusion and Recommendations

This research was motivated by a key hypothesis by which remote triggered seismicity in underground mining could be justified. The hypothesis suggests that while the stress changes resulted from mining openings are negligible at far distances from them, gravity-driven deformations with related changes in local boundary conditions facilitate remote seismicity. For this it is not necessary to break discrete rock blocks or to mobilize block boundaries between two mining blocks. It is sufficient to displace a jointed rock mass without newly formed blocks as a result of rock bridge breakage. Deformations from one mining block to and other can be transferred over large distances when a chimney like subsidence cone can develop. Unless this deformation transfer process is disrupted by stable arching, stress changes are encountered at remote locations. The gravity-induced translation displacements therefore cause a remote seismicity event.

To examine our hypothesis in reality, a new deformation measurement system was experimentally tested to evaluate the feasibility of such a system in bridging the gap in mine-scale deformation monitoring and seismicity.

In the future, it will be possible to conduct field measurements to conclusively prove the gravity-driven remote seismicity model. Unfortunately, this was not possible during the research period for this thesis.

6.1. Conclusions

The following sections present a summary of results associated with each chapter of this thesis.

6.1.1. Primary evaluation of DiTeSt™

Continuous interrogation of an unstrained SMARTprofile™ cable was performed to characterise the noise level below which no changes in temperature or deformation could be detected. Also, a spatial shift along the optical cable was noticed from various overlain strain profiles, and this was partially corrected using a comparative algorithm. The results show that the system can provide high performance in strain sensing with a minimum noise level of ±75 με.

Extensional tests on various strained lengths show that the strain could be accurately detected down to a strained length above half the claimed spatial resolution, i.e. 25 cm. Below this length the registered response is unreliable, highlighting a system limitation for the measurement of short strained length sections. This limit also dictates the base requirement for future test designs and field installations (e.g. clamping points spacing). During these tests the frequency-strain conversion factor was re-evaluated and refined.

The behaviour of deformation events over a strained length shorter than $L_{SR}/2$ is better understood when considering Brillouin gain spectra. It was found that $\Delta\nu_B$ changes are not linked to the strained length, but the peak gain can be correlated with the strained length.

6.1.3. Sensor installation procedure

A sensing cable was clamped at a particular length to moving and fixed plates of a test apparatus purposely built for these tests to create various strained section configurations to explore the spatial resolution of the system. The cable clamping configurations included three consecutive 50 cm sections with 0 cm, 30 cm, and 150 cm strain-free sections in between former sections. The applied displacement sequence chosen was applied through two different loading paths; in one experiment the displacements for each 50 cm section were simultaneously applied, whereas in the other scenario each section was strained when the previous one had already been strained to its maximum level. The DiTeSt™ could precisely show the spatial distribution of the strained sections. Furthermore, the frequency change response of the system was found to be independent of the loading path.

The installation method for the current objective of DiTeSt™ usage is borehole placement with grout filling. A major part of the experiments was to study the interaction between an embedded cable and the mortar beams (i.e. grout) and the effect of mortar properties on the strain transfer process.

When the cable was fully embedded in and bonded to the mortar beam, the DiTeSt™ response was different at each of three 55 cm spaced induced crack locations. This was found to be significantly influenced by the self-debonding length evolution with applied displacement. Apart from the positive point that the system could register frequency changes during cable debonding, the amount of crack opening could not be estimated with high accuracy since the strained length was not constant. The same test implemented with weaker mortar showed that the debonding process then became more uncontrolled.

The cable was then anchored at 50 cm spacing and pre-debonded from the mortar between anchors. Inducing one crack over each anchored interval resulted in a totally different frequency compared to that in the fully bonded cable test. The frequency change registered over each interval was quite repeatable and consistent with the applied displacement since the strained length was constant.

The DiTeSt™ response was also evaluated with the presence of three cracks in the mortar beam over the strained length. With an imperfect debonded installation, one could actually approximate the number of the cracks in the interval and their opening sequence from the non-uniform frequency profiles, but this is not recommended because of other factors such as consistency in installation. On the other hand, a highly effective debonding method provides quite uniform profiles, but individual crack movements within an anchored interval could not be tracked.

Finally, the effect of filling thickness and strength on the strain measurement effectiveness were evaluated using a larger diameter beam and a beam formed with weaker strength mix, respectively. In both tests, DiTeSt™ showed exactly the same performance as with a smaller beam and stronger mortar. This is related directly to the cable embedment method in the mortar. Therefore, the most

important characteristics of the filling material should be a low tensile strength so that it breaks at the joint locations as soon as they start moving.

The best method of installation based on the experimental studies on the sensing cable under pure tension should be the anchoring-debonding method with minimum 50 cm anchor spacing and a method to give high quality and complete debonding between anchors.

6.1.4. Shear displacement response of DiTeSt™

The test involving various strained lengths (l) from 1 to 100 cm showed that all lengths above 30 cm could show a frequency response over the strained length, although sometimes no response was observed for $L_{SR}/2 \leq l \leq 40$ cm (L_{SR} is spatial resolution of the DiTeSt™). Furthermore, it was noticed that the Brillouin frequency shift change ($\Delta\nu_B$) varied in a parabolic trend with shear displacement, contrary to axial tests where a clear linear correlation was established. Apart from the strained length, another important factor was taken into account for its effect on the shear displacement response of the system. Reducing the kink length (L_K), a length over which the transverse effect of the shear displacement occurs, showed a significant increase in the frequency response. The frequency profile also showed a slightly higher response where the kink guides were located along the strained length, particularly noticeable for shorter kink and longer strained lengths. Due to effect of the arc-length, 10-40 time more displacement was required to induce a given $\Delta\nu_B$ in comparison with to direct tension tests. In addition, because of the rectangular cross-section of SMARTprofile™ the effect of bending about its shorter and longer sides when under shear displacement was studied. The $\Delta\nu_B$-D_S results showed their difference was within 5% for various stained lengths.

Another influential parameter on the system behavior was the relative joint-cable inclination. A section of SMARTprofile™ was laid out on the test setup at 75° from the joint trace and sheared in a way to induce elongation in the sensor. The $\Delta\nu_B$-D_S showed that the frequency still followed the parabolic trend observed in direct shear (90°) but with less intensity in curvature and a clear linear trend. The linear trend was due to the longitudinal component of the shear displacement that caused an axial strain in the sensing cable. Furthermore, $\Delta\nu_B$ from all kink lengths showed less divergence with shear displacement relative to large differences for the same kink lengths in direct 90° shear. On the other hand, the same test was repeated when displacement direction created a shortening in the sensing cable upon shear movement, and the frequency profile showed that the system could register negative values representing occurrence of compression. Although continuation of displacement in the same direction would eventually cause an elongation, the displacement was kept within the recommended shortening range of the cable since the cable was prone to damage at a short radius of curvature.

The effect of the presence of more than one joint over the strained length on the system response was tested whether the cable crossed the joints at 90° or with an inclination. From the 90° shear test results it was found that a given $\Delta\nu_B$ profile could be obtained through various displacement paths. Also, it was found that the displacement at each joint should be individually incorporated

into total displacement in order to understand Δv_B-D_S response. For the shear with an inclined cable with respect to the joint trace, it was notice that frequency profile became non-uniform when the cable at one joint was under elongation and at the other joint was under shortening during shear displacement. The frequency profile showed higher values in elongation, and dropped to smaller values at locations closer to shortening displacement.

Extending the Newmark and Hall equation for pipelines under lateral movement by a strike-slip fault, a new theoretical relation was established based on a triangle approximation. The equation accounts for all parameters influencing the shear response of the system including shear displacement (D_S), strained length (l), kink length (L_K), and the joint-cable orientation (α). The formulation best works for the situation when the cable is elongated under shear displacement rather than shortening, since it becomes more complicated for the latter case.

6.2. Recommendations

There are a number of ideas or issues for possible future work as follows:

6.2.1. DBS measurement

- It is recommended that a temperature correction of strain measurement using temperature sensor data is studied in a separate research.
- The next step for this work is to install a single sensing cable, i.e. SMARTprofile™, in an underground mine site near a stope under extraction and measuring the deformation for a period of one month for the purpose of evaluating the proposed installation procedure and troubleshooting.
- To help interpret the results, it is considered essential that a high resolution borehole wall image be obtained in order to identify the location of joints and sheared bands where shear displacement may be likely to occur as mining continues.
- After completion of the previous step when the installation procedure is approved, it is recommended that a real case monitoring is designed and performed. In this case, a mining panel or block can be instrumented at different pre-determined locations and the rock mass deformation is then monitored for a period of 6-12 months or more. This will provide a mine-scale deformation pattern for evaluation of actual practicality of the system and correlating the evolution of deformation of the rock mass over time with distant seismic events, if any.

6.2.2. Modeling

- Before installing the DiTeSt™ in an underground mine site for mine-scale deformation monitoring, it is best to do an experimental design for a real mine using a numerical modeling to understand the optimum locations for installation of the SMARTprofile according to the current mine geometry and stoping sequences.

- Later when deformation measurements from the field trail are available, it is worth using such data in order to calibrate an existing elastic stress model through back-analysis for refinement of input data.

Bibliography

Adachi, S. (2008). Distributed optical fiber sensors and their applications. In *SICE Annual Conference 2008* (pp. 329–333). Tokyo, Japan. doi:10.1109/SICE.2008.4654674

Ansari, B. F., & Libo, Y. (1998). Mechanics of bond and interface shear transfer in optical. *Journal of Engineering Mechanics*, *124*(4), 385–394.

Bao, X., & Chen, L. (2012). Recent progress in distributed fiber optic sensors. *Sensors*, *12*(7), 8601–39. doi:10.3390/s120708601

Bao, X., Demerchant, M., Brown, A., & Bremner, T. (2001). Strain measurement of the steel beam with the distributed Brillouin scattering sensor. In *6th Annual International Symposium on NDE for Health Monitoring and Diagnostics* (Vol. 4337, pp. 223–233).

Bao, X. Y., Ravet, F., & Zou, L. F. (2005). Nonlinear strain response of the concrete column to detect the debonding and cracks using distributed Brillouin sensor. In *Proceedings of the ISHMII-2* (pp. 235–242).

Bao, X., Zhang, C., Li, W., Eisa, M., El-Gamal, S., & Benmokrane, B. (2008). Monitoring the distributed impact wave on a concrete slab due to the traffic based on polarization dependence on stimulated Brillouin scattering. *Smart Materials and Structures*, *17*(1), 015003. doi:10.1088/0964-1726/17/01/015003

Bao, Y., Meng, W., Chen, Y., Chen, G., & Khayat, K. H. (2015). Measuring mortar shrinkage and cracking by pulse pre-pump Brillouin optical time domain analysis with a single optical fiber. *Materials Letters*, *145*, 344–346. doi:10.1016/j.matlet.2015.01.140

Barnoski, M. K., Rourke, M. D., Jensen, S. M., & Melville, R. T. (1977). Optical time domain reflectometer. *Appl. Opt.*, *16*(9), 2375–2379. doi:10.1364/AO.16.002375

Barton, N., & Bandis, S. (1982). Effects of block size on the shear behavior of jointed rock. In *The 23rd U.S Symposium on Rock Mechanics (USRMS)* (p. 22). American Rock Mechanics Association. Retrieved from http://www.onepetro.org/mslib/servlet/onepetropreview?id=ARMA-82-739

Bastianini, F., Rizzo, A., Galati, N., Deza, U., & Nanni, A. (2005). Discontinuous Brillouin strain monitoring of small concrete bridges: comparison between near-to-surface and “smart” FRP fiber installation techniques, *5765*, 612–623. doi:10.1117/12.594760

Bernini, R., Fraldi, M., Minardo, A., Minutolo, V., Carannante, F., Nunziante, L., & Zeni, L. (2006). Identification of defects and strain error estimation for bending steel beams using time domain Brillouin distributed optical fiber sensors. *Smart Materials and Structures*, *15*(2), 612–622. doi:10.1088/0964-1726/15/2/045

Bhalla, S., Yang, Y. W., Zhao, J., & Soh, C. K. (2005). Structural health monitoring of underground facilities – Technological issues and challenges. *Tunnelling and Underground Space Technology*, *20*(5), 487–500. doi:10.1016/j.tust.2005.03.003

Brady, B. H. G., & Brown, E. T. (2004). *Rock mechanics for underground mining* (Third edit.). London: Chapman & Hall.

Burridge, R., & Knopoff, L. (1967). Model and theoretical seismicity. *Bulletin of the Seismological Society of America*, *57*(3), 341–371.

Cai, M., Kaiser, P. K., & Martin, C. D. (1998). A Tensile Model for the Interpretation of Microseismic Events near Underground Openings. *Pure and Applied Geophysics*, *153*(1), 67–92. doi:10.1007/s000240050185

Cai, M., Kaiser, P. K., & Martin, C. D. (2001). Quantification of rock mass damage in underground excavations from microseismic event monitoring. *International Journal of Rock Mechanics and Mining Sciences*, *38*(8), 1135–1145. Retrieved from http://www.sciencedirect.com/science/article/pii/S1365160901000685

Cappa, F., Guglielmi, Y., Gaffet, S., Lançon, H., & Lamarque, I. (2006). Use of in situ fiber optic sensors to characterize highly heterogeneous elastic displacement fields in fractured rocks. *International Journal of Rock Mechanics and Mining Sciences*, *43*(4), 647–654. doi:10.1016/j.ijrmms.2005.09.016

Chai, J., Liu, J., Qiu, B., Li, Y., Zhu, L., Wei, S., … Yang, J. (2011). Detecting deformations in uncompacted strata by fiber Bragg grating sensors incorporated into GFRP. *Tunnelling and Underground Space Technology*, *26*(1), 92–99. doi:10.1016/j.tust.2010.06.009

Chen, C.-H., Shen, Y.-L., & Shin, C.-S. (2011). Using Distributed Brillouin Fiber Sensor to Detect the Strain and Cracks of Steel Structures. *Journal of Mechanics*, *26*(04), 547–551. doi:10.1017/S1727719100004743

Cole, C. (2006). Longitudinal Train Dynamics. In *Handbook of Railway Vehicle Dynamics* (pp. 239–277). CRC Press. doi:doi:10.1201/9781420004892.ch9

Cook, N. (1976). Seismicity associated with mining. *Engineering Geology*, *10*(2-4), 99–122. Retrieved from http://www.sciencedirect.com/science/article/pii/0013795276900156

Deif, a, Martín-Pérez, B., Cousin, B., Zhang, C., Bao, X., & Li, W. (2010). Detection of cracks in a reinforced concrete beam using distributed Brillouin fibre sensors. *Smart Materials and Structures*, *19*(5), 055014. doi:10.1088/0964-1726/19/5/055014

Dietz, K., Habel, W., & Feddersen, I. (2001). Eder Dam, stabilisation by permanent rock anchors-Monitoring and long term performance. In J. Bertram (Ed.), *ICOLD – 69th ANNUAL MEETING: Symposium Benefits and Concerns about Dams*. Dresden.

Dunnicliff, J. (1993). *Geotechnical instrumentation for monitoring field performance*. New York, NY: John Wiley & Sons.

Dupin, J., Sassi, W., & Angelier, J. (1993). Homogeneous stress hypothesis and actual fault slip: a distinct element analysis. *Journal of Structural Geology*, *15*(8), 1033–1043.

Enckell, M., Glišić, B., Myrvoll, F., & Bergstrand, B. (2011). Evaluation of a large-scale bridge strain, temperature and crack monitoring with distributed fibre optic sensors. *Journal of Civil Structural Health Monitoring*, *1*(1-2), 37–46. doi:10.1007/s13349-011-0004-x

Ferdinand, P., Ferragu, O., Lechien, J. L., Lescop, B., Magne, S., Marty, V., … Toscano, D. (1995). Mine operating accurate stability control with optical fiber sensing and Bragg grating technology: the European BRITE/EURAM STABILOS project. *Journal of Lightwave Technology*, *13*(7), 1303–1313. doi:10.1109/50.400683

Ferdinand, P., Rougeault, S., Roussel, N., Pinabiau, M., Canepa, C., Da Rocha, J.-C., … Finck, C. (2012). Brillouin sensing for perimetric detection: the SmartFence project. In Y. Liao, W. Jin, D. D. Sampson, R. Yamauchi, Y. Chung, K. Nakamura, & Y. Rao (Eds.), *22nd International Conference on Optical Fiber Sensors* (Vol. 8421, pp. 84219X1–4). doi:10.1117/12.974960

Fidanboylu, K., & Efendioglu, H. (2009). Fiber optic sensors and their applications. In M. Acarer, H. İ. Demirci, & C. Göloğlu (Eds.), *5th International Advanced Technologies Symposium (IATS'09)* (pp. 13–15). Karabük, Turkey: Karabük University.

Gay, N. C., Spencer, D., Wyk, J. Van, Heever, P. Van der, Van Wyk, J. J., & Van Der Heever, P. K. (1984). The control of geological and mining parameters in the Klerksdorp gold mining district. In *Rockbursts and Seismicity in Mines* (pp. 107–120).

Glišić, B., Chen, J., & Hubbell, D. (2011). Streicker Bridge: A comparison between Bragg-grating long-gauge strain and temperature sensors and Brillouin scattering-based distributed strain and temperature sensors. In M. Tomizuka (Ed.), *Proc. SPIE 7981, Sensors and Smart Structures Technologies for Civil, Mechanical, and Aerospace Systems* (Vol. 7981, p. 79812C–79812C–10). doi:10.1117/12.881818

Glišić, B., Posenato, D., & Inaudi, D. (2007). Integrity monitoring of old steel bridge using fiber optic distributed sensors based on Brillouin scattering. In H. F. Wu, A. A. Diaz, & P. J. Shull (Eds.), *The 14th International Symposium on: Smart Structures and Materials & Nondestructive Evaluation and Health Monitoring* (Vol. 6531, p. 65310P–65310P–8). doi:10.1117/12.716055

Glišić, B., & Yao, Y. (2012). Fiber optic method for health assessment of pipelines subjected to earthquake-induced ground movement. *Structural Health Monitoring*, *11*(6), 696–711. doi:10.1177/1475921712455683

Guzik, A., Yokoyama, M., Matsuda, K., & Kishida, K. (2013). Monitoring of the ground settlement during a tunnel excavation using 4D optical fiber sensing system. In L. R. Jaroszewicz (Ed.), *Proc. of SPIE Vol. 8794: Fifth*

European Workshop on Optical Fibre Sensors (Vol. 8794, p. 87943H). doi:10.1117/12.2026148

Hasegawa, H. S., Wetmiller, R. J., & Gendzwill, D. J. (1989). Induced Seismicity in Mines in Canada--An Overview. *Pure and Applied Geophysics*, *129*(3), 423–453.

He, J., Wu, H., & Zhou, Z. (2007). Long-term Monitoring of a Civil Defensive Structure based on Distributed Brillouin Optical Fiber Sensor. *Pacific Science Review*, *9*(1), 97–102.

He, J., Zhou, Z., & Jinping, O. (2012). Optic fiber sensor-based smart bridge cable with functionality of self-sensing. *Mechanical Systems and Signal Processing*, *35*(1-2), 84–94. doi:10.1016/j.ymssp.2012.08.022

Heasley, K., Dubaniewicz, T., & DiMartino, M. (1997). Development of a fiber optic stress sensor. *International Journal of Rock Mechanics and Mining Sciences*, *34*(3), 66–e1.

Hiroyuki, S. (2001). *Landslide Monitoring by Optical Fiber Sensor*. Japan.

Hoepffner, R. (2008). *Distributed fiber optic strain sensing in hydraulic concrete and earth structures : measuring theory and field investigations on dams and landslides*. Technische Universität München, Munich.

Hoepffner, R., Singer, J., Thuro, K., & Aufleger, M. (2008). Development of an integral system for dam and landslide monitoring based on distributed fibre optic technology. In *15th Biennial Conference on "Ensuring Reservoir Safety into the Future"* (p. 12).

Homuth, F., Chen, J., & VanEeckhout, E. (1998). Fiber optics - A new method for monitoring stress changes in the Earth. *Potentials, IEEE*, *17*(4), 15–18. doi:10.1109/45.721727

Horiguchi, T., Shimizu, K., Kurashima, T., Tateda, M., & Koyamada, Y. (1995). Development of a distributed sensing technique using Brillouin scattering. *Journal of Lightwave Technology*, *13*(7), 1296–1302. doi:10.1109/50.400684

Horiguchi, T., & Tateda, M. (1989). Optical-fiber-attenuation investigation using stimulated Brillouin scattering between a pulse and a continuous wave. *Optics Letters*, *14*(8), 408–410. doi:10.1364/OL.14.000408

Horner, R., & Hasegawa, H. (1978). The seismotectonics of southern Saskatchewan. *Canadian Journal of Earth Sciences*, *15*(8), 1341–1355.

Huntley, D., Bobrowsky, P., Qing, Z., Sladen, W., Bunce, C., Edwards, T., … Choi, E. (2014). Fiber Optic Strain Monitoring and Evaluation of a Slow-Moving Landslide Near Ashcroft, British Columbia, Canada. In *Landslide Science for a Safer Geoenvironment* (Vol. 1, pp. 415–421). doi:10.1007/978-3-319-05050-8

Imai, M., & Feng, M. (2012). Sensing optical fiber installation study for crack identification using a stimulated Brillouin-based strain sensor. *Structural Health Monitoring*, *11*(5), 501–509. doi:10.1177/1475921712442440

Inaudi, D. (2003). Application of Fiber Optic Sensors to Structural Monitoring. In B. Culshaw (Ed.), *Proceedings of SPIE Vol. 4763: European Workshop on Smart Structures in Engineering and Technology* (Vol. 4763, pp. 31–38). doi:10.1117/12.508669

Inaudi, D., Belli, R., & Walder, R. (2008). Detection and localization of micro-leakages using distributed fiber optic sensing. In *Proceedings of IPC2008 -7th International Pipeline Conference* (pp. 1–7). doi:10.1115/IPC2008-64280

Inaudi, D., & Glišić, B. (2006a). Distributed fiber optic strain and temperature sensing for structural health monitoring. In *IABMAS'06 The 3rd Int'l Conference on Bridge Maintenance, Safety and Management* (p. 8). Porto, Portugal.

Inaudi, D., & Glišić, B. (2006b). Integration of distributed strain and temperature sensors in composite coiled tubing. In D. Inaudi, W. Ecke, B. Culshaw, K. J. Peters, & E. Udd (Eds.), *SPIE Proceedings Vol. 6167 Smart Structures and Materials 2006: Smart Sensor Monitoring Systems and Applications* (p. 10). San Diego, CA: SPIE. doi:10.1117/12.661086

Iten, M. (2011). *Novel applications of distributed fiber-optic sensing in geotechnical engineering*. PhD thesis, ETH Zurich.

Iten, M., Hauswirth, D., & Puzrin, A. M. (2011). Distributed fiber optic sensor development, testing and evaluation for geotechnical monitoring applications. In W. Ecke, K. J. Peters, & T. E. Matikas (Eds.), *Proc. of SPIE Vol.*

7982 Smart Sensor Phenomena, Technology, Networks, and Systems 2011 (Vol. 7982, pp. 798207–798207–15). San Diego, California, USA. doi:10.1117/12.881228

Iten, M., & Puzrin, A. M. (2009). BOTDA road-embedded strain sensing system for landslide boundary localization. In N. G. Meyendorf;, K. J. Peters;, & W. Ecke (Eds.), *Proc. SPIE 7293, Smart Sensor Phenomena, Technology, Networks, and Systems 2009* (Vol. 7293, pp. 729316–729316–12). San Diego, California, USA. doi:10.1117/12.815266

Johansson, S., & Watley, D. (2007). *Dam safety experiences from distributed strain measurements in five embankment dams*. Stockholm, Sweden.

Juarez, J. C., Maier, E. W., & Taylor, H. F. (2005). Distributed fiber-optic intrusion sensor system. *Journal of Lightwave Technology*, *23*(6), 2081–2087. doi:10.1109/JLT.2005.849924

Kaiser, P. K., Vasak, P., Suorineni, F. T., & Thibodeau, D. (2005). New dimensions in seismic data interpretation with 3-D virtual reality visualization for burst-prone mines. In Y. Potvin & M. Hudyma (Eds.), *6th Int. Symp. on Rockburst and Seismicity in Mines (RaSiM6)* (pp. 33–45). Perth, Australia: Australian Centre for Geomechanics.

Kim, S.-H., Lee, J.-J., & Kwon, I.-B. (2002). Structural monitoring of a bending beam using Brillouin distributed optical fiber sensors. *Smart Materials and Structures*, *11*(3), 396–403. doi:10.1088/0964-1726/11/3/310

Klar, A., Bennett, P., Soga, K., Mair, R. J., Tester, P., Fernie, R., … Torp-Peterson, G. (2006). Distributed strain measurement for pile foundations. *Proceedings of the ICE - Geotechnical Engineering*, *159*(3), 135–144.

Klar, A., & Linker, R. (2010). Feasibility study of automated detection of tunnel excavation by Brillouin optical time domain reflectometry. *Tunnelling and Underground Space Technology*, *25*(5), 575–586. doi:10.1016/j.tust.2010.04.003

Koutsabeloulis, N. C., & Griffiths, D. V. (1989). Numerical modelling of the trap door problem. *Géotechnique*, *39*(1), 77–89. doi:10.1680/geot.1989.39.1.77

Krebber, K., Lenke, P., Liehr, S., Noether, N., Wendt, M., & Wosniok, A. (2010). Distributed fiber optic sensors embedded in technical textiles for structural health monitoring. In J. L. Santos, B. Culshaw, J. M. López-Higuera, & W. N. MacPherson (Eds.), *Fourth European Workshop on Optical Fibre Sensors* (Vol. 7653, p. 76530A–76530A–12). doi:10.1117/12.868052

Lan, C., Zhou, Z., & Ou, J. (2014). Monitoring of structural prestress loss in RC beams by inner distributed Brillouin and fiber Bragg grating sensors on a single optical fibe. *Structural Control and Health Monitoring*, *21*(May 2011), 317–330. doi:10.1002/stc

Lanticq, V., Bourgeois, E., Magnien, P., Dieleman, L., Vinceslas, G., Sang, A., & Delepine-Lesoille, S. (2009). Soil-embedded optical fiber sensing cable interrogated by Brillouin optical time-domain reflectometry (B-OTDR) and optical frequency-domain reflectometry (OFDR) for embedded cavity detection and sinkhole warning system. *Measurement Science and Technology*, *20*(3), 034018. doi:10.1088/0957-0233/20/3/034018

Li, X., America, B. P., Parker, T., Farhadiroushan, M., & Blacklaw, D. (2004). Evaluating a Concept of Using Distributed Optical Fiber Temperature and Strain Sensor for Continuous Monitoring of Casing and Completion Mechanical Deformation. In *Offshore Technology Conference* (pp. 1–17).

Liehr, S., Lenke, P., Krebber, K., Seeger, M., Thiele, E., Metschies, H., … Stempniewski, L. (2008). Distributed strain measurement with polymer optical fibers integrated into multifunctional geotextiles, *7003*, 700302–700302–15. doi:10.1117/12.780508

Liu, T., Wang, C., Wei, Y., Zhao, Y., Huo, D., Shang, Y., … Ning, Y. (2009). Hazard monitoring in mines using fibre optic sensors. In J. Jones, B. Culshaw, W. Ecke, J. M. López-Higuera, & R. Willsch (Eds.), *20th International Conference on Optical Fibre Sensors. Proceedings of SPIE* (Vol. 7503, p. 75030H–75030H–5). SPIE. doi:10.1117/12.837611

Lourence, B., Jung, S. J., & Sprenke, K. F. (1993). Source mechanisms at the Lucky Friday Mine: Initial results from the North Idaho Seismic Network. In *Rockbursts and Seismicity in Mines 93: Proceedings of the 3rd international symposium, Kingston, Ontario, 16-18 August 1993* (pp. 217–222). Taylor & Francis.

Lu, L., Liang, Y., Li, B., Guo, J., Zhang, H., & Zhang, X. (2014). Health monitoring of electric power

communication line using a distributed optical fiber sensor, *9274*, 92740W. doi:10.1117/12.2072870

Lu, Y., Shi, B., Wei, G. Q., Chen, S. E., & Zhang, D. (2012). Application of a distributed optical fiber sensing technique in monitoring the stress of precast piles. *Smart Materials and Structures*, *21*, 115011(9pp). doi:10.1088/0964-1726/21/11/115011

Madjdabadi, B., Valley, B., Dusseault, M. B., & Kaiser, P. K. (2016). Experimental evaluation of a distributed Brillouin sensing system for measuring extensional and shear deformation in rock. *Measurement*, *77*, 54–66. doi:10.1016/j.measurement.2015.08.040

Martín-Pérez, B., Deif, A., Cousin, B., Zhang, C., Bao, X., & Li, W. (2010). Strain monitoring in a reinforced concrete slab sustaining service loads by distributed Brillouin fibre optic sensors. *Canadian Journal of Civil Engineering*, *37*(10), 1341–1349. doi:10.1139/L10-080

McGarr, A. (1971). Violent deformation of rock near deep-level, tabular excavations--seismic events. *Bulletin of the Seismological Society of America*, *61*(5), 1453–1466.

McGarr, A. (2000). Energy budgets of mining-induced earthquakes and their interactions with nearby stopes. *International Journal of Rock Mechanics and Mining Sciences*, *37*(1-2), 437–443.

McGarr, A., & Green, R. W. E. (1975). Measurement of tilt in a deep-level gold mine and its relationship to mining and seismicity. *Geophysical Journal of the Royal*, *43*(2), 327–345.

Mikkelsen, P. (2002). Cement-bentonite grout backfill for borehole instruments. *Geotechnical Instrumentation News*, *20*(4), 38–42. Retrieved from http://slopeindicator.com/pdf/papers/grout-backfill.pdf

Milev, A. M., & Spottiswoode, S. M. (2002). Effect of the rock properties on mining-induced seismicity around the Ventersdorp Contact Reef, Witwatersrand Basin, South Africa. *Pure and Applied Geophysics*, *159*(1), 165–177. doi:10.1007/PL00001249

Minardo, A., Bernini, R., Amato, L., & Zeni, L. (2012). Bridge Monitoring Using Brillouin Fiber-Optic Sensors. *IEEE Sensors Journal*, *12*(1), 145–150. doi:10.1109/JSEN.2011.2141985

Minardo, A., Porcaro, G., Giannetta, D., Bernini, R., & Zeni, L. (2013). Real-time monitoring of railway traffic using slope-assisted Brillouin distributed sensors. *Applied Optics*, *52*(16), 3770–6. Retrieved from http://www.ncbi.nlm.nih.gov/pubmed/23736333

Moffat, R., Sotomayor, J., & Beltrán, J. F. (2015). Estimating tunnel wall displacements using a simple sensor based on a Brillouin optical time domain reflectometer apparatus. *International Journal of Rock Mechanics and Mining Sciences*, *75*, 233–243. doi:10.1016/j.ijrmms.2014.10.013

Mohamad, H., Bennett, P. J., Soga, K., Klar, A., & Pellow, A. (2007). Distributed Optical Fiber Strain Sensing in a Secant Piled Wall. In *7th FMGM 2007: Field Measurements in Geomechanics* (pp. 1–12). Reston, VA: American Society of Civil Engineers. doi:10.1061/40940(307)81

Mohamad, H., Bennett, P. J., Soga, K., Mair, R. J., & Bowers, K. (2010). Behaviour of an old masonry tunnel due to tunnelling-induced ground settlement. *Géotechnique*, *60*(12), 927–938. doi:10.1680/geot.8.P.074

Mohamad, H., Bennett, P. J., Soga, K., Mair, R. J., Lim, C.-S., Knight-Hassell, C. K., & Ow, C. N. (2007). Monitoring Tunnel Deformation Induced by Close-Proximity Bored Tunneling Using Distributed Optical Fiber Strain Measurements. In J. DiMaggio & P. Osborn (Eds.), *7th FMGM 2007: Field Measurements in Geomechanics* (Vol. 175, pp. 1–13). Boston, Massachusetts, United States: American Society of Civil Engineers. doi:doi:10.1061/40940(307)84

Momand, F. A. (2010). *Monitoring Slope Stability Problems Utilizing Electrical and Optical TDR*. *Engineering and Technology*. Russ College of Engineering and Technology of Ohio University. Retrieved from http://etd.ohiolink.edu/send-pdf.cgi/Momand Farid.pdf?ohiou1289317906

Moore, J., Gischig, V., Button, E., & Loew, S. (2010). Rockslide deformation monitoring with fiber optic strain sensors. *Natural Hazards and Earth System Science*, *10*(2), 191–201.

Mufti, a., Thomson, D., Inaudi, D., Vogel, H. M., & McMahon, D. (2011). Crack detection of steel girders using Brillouin optical time domain analysis. *Journal of Civil Structural Health Monitoring*, *1*(3-4), 61–68. doi:10.1007/s13349-011-0006-8

Murayama, H., & Kageyama, K. (2003). Application of fiber-optic distributed sensors to health monitoring for full-scale composite structures. *Journal of Intelligent Material Systems and Structures*, *14*(1), 3–13. doi:10.1177/104538903032738

Murayama, H., Kageyama, K., Naruse, H., & Shimada, A. (2004). Distributed Strain Sensing from Damaged Composite Materials Based on Shape Variation of the Brillouin Spectrum. *Journal of Intelligent Materials Systems and Structures*, *15*(1), 17–25. doi:10.1177/1045389X04039263

Nan, S., & Gao, Q. (2011). Application of Distributed Optical Fiber Sensor Technology Based on BOTDR in Similar Model Test of Backfill Mining. *Procedia Earth and Planetary Science*, *2*, 34–39. doi:10.1016/j.proeps.2011.09.006

Naruse, H., Uehara, H., Deguchi, T., Fujihashi, K., Ishikura, Y., Onishi, M., … Galvez, F. (2006). Underground Mine Monitoring Using Distributed Fiber Optic Strain Sensing System. In *Optical Fiber Sensors*. Optical Society of America.

Naruse, H., Uehara, H., Deguchi, T., Fujihashi, K., Onishi, M., Espinoza, R., … Pinto, M. (2007). Application of a distributed fibre optic strain sensing system to monitoring changes in the state of an underground mine. *Measurement Science and Technology*, *18*(10), 3202–3210. doi:10.1088/0957-0233/18/10/S23

Nellen, P. M., Frank, A., Brönnimann, R., Sennhauser, U. J., & Broennimann, R. (2000). Optical Fiber Bragg Gratings for tunnel surveillance. In R. O. Claus; & W. B. Spillman (Eds.), *Proc. SPIE 3986, Smart Structures and Materials 2000: Sensory Phenomena and Measurement Instrumentation for Smart Structures and Materials* (Vol. 3986, pp. 263–270). Newport Beach, CA.

Newmark, N. M., & Hall, W. J. (1975). Pipeline design to resist large fault displacement. In *Proceedings, 1s US National Conference on Earthquake Engineering* (pp. 416–425). Ann Arbor, Michigan: Earthquake Eng Res Inst.

Noni, MacLaughlin, M. M., & Wang, H. F. (2011). Validation of Fiber-Optic Strain-Sensing Cable for Deep Underground Installation. In *45th US Rock Mechanics / Geomechanics Symposium* (p. 10).

O'Rourke, M. J., & Liu, J. X. (2012). *Seismic Design of Buried and Offshore Pipelines*. MCEER University at Buffalo, State University of New York.

Ohsaki, M., Tateda, M., & Omatsu, T. (2002). Spatial resolution enhancement of distributed strain measurement using BOTDR by partially gluing optical fiber. *IEICE Transactions on Communications*, *85*(8), 1636–1639.

Posenato, D., Kripakaran, P., Inaudi, D., & Smith, I. F. C. C. (2010). Methodologies for model-free data interpretation of civil engineering structures. *Computers & Structures*, *88*(7–8), 467–482. doi:10.1016/j.compstruc.2010.01.001

Rochat, E., & Nikles, M. (2012). Fiber optic asset integrity monitoring using Brillouin-based distributed sensing for the oil and gas and energy industries: challenges and achievements. In Y. Liao, W. Jin, D. D. Sampson, R. Yamauchi, Y. Chung, K. Nakamura, & Y. Rao (Eds.), *OFS2012 22nd International Conference on Optical Fiber Sensors* (Vol. 8421, pp. 84210N1–4). doi:10.1117/12.2008250

Schmidt-Hattenberger, C., & Borm, G. (1998). Bragg grating extensometer rods (BGX) for geotechnical strain measurements. In B. Culshaw; & J. D. Jones (Eds.), *Proceedings of SPIE: European Workshop on Optical Fibre Sensors* (Vol. 3483, pp. 214 –217).

Schmidt-Hattenberger, C., Borm, G., & Amberg, F. (1999). Bragg grating seismic monitoring system. In M. A. Marcus; & B. Culshaw (Eds.), *Proceedings of SPIE: Fiber Optic Sensor Technology and Applications* (Vol. 3860, pp. 417–424). Boston, MA: SPIE.

Shi, B., SUI, H., LIU, J., & ZHANG, D. (2006). The BOTDR-based distributed monitoring system for slope engineering. In *IAEG2006* (pp. 1–5). The Geological Society of London.

Shi, B., Xu, H., Chen, B., Zhang, D., Ding, Y., Cui, H., & Gao, J. (2003). A Feasibility Study on the Application of Fiber-Optic Distributed Sensors for Strain Measurement in the Taiwan Strait Tunnel Project. *Marine Georesources & Geotechnology*, *21*(3-4), 333–343. doi:10.1080/713773406

Soga, K., Amatya, B., Wright, P., Bennett, P. J., Kobayashi, Y., & Cheung, L. L. K. (2010). Optical fibre strain measurement for tunnel lining monitoring. *Proceedings of the ICE - Geotechnical Engineering*, *163*(3), 119–

130. doi:10.1680/geng.2010.163.3.119

Spottiswoode, S., Linzer, L., & Majiet, S. (2008). Energy and stiffness of mine models and seismicity. In Y. Potvin, J. Carter, A. Dyskin, & R. Jeffrey (Eds.), *1th Southern Hemisphere International Rock Mechanics Symposium SHIRMS 2008* (Vol. 1, pp. 693–707). Perth.

Terzaghi, K. V. (1936). Stress distribution in dry and in saturated sand above a yielding trap-door. In *Proceedings of the First International Conference on Soil Mechanics and Foundation Engineering* (pp. 307–311).

Thévenaz, L. (2006). Review and Progress on Distributed Fibre Sensing. In *Optical Fiber Sensors* (p. ThC1). doi:10.1364/OFS.2006.ThC1

Thévenaz, L. (2010). Brillouin distributed time-domain sensing in optical fibers: state of the art and perspectives. *Frontiers of Optoelectronics in China*, *3*(1), 13–21. doi:10.1007/s12200-009-0086-9

Thévenaz, L., Facchini, M., Fellay, A., Nikles, M., & Robert, P. (2001). Field tests of distributed temperature and strain measurement for smart structures. In *The 4th Pacific Rim Conference on Lasers and Electro-Optics, 2001. CLEO/Pacific Rim 2001.* (Vol. 1, pp. 490–491). Chiba, Japan: IEEE. doi:10.1109/CLEOPR.2001.967938

Thévenaz, L., Nikles, M., Fellay, A., Facchini, M., & Robert, P. A. (1998). Applications of distributed Brillouin fiber sensing. In P. K. Rastogi; & F. Gyimesi (Eds.), *Proc. SPIE 3407, International Conference on Applied Optical Metrology, 374* (Vol. 3407, pp. 374–381). Balatonfured, Hungary: International Society for Optics and Photonics. doi:10.1117/12.323342

Urbancic, T. I., & Trifu, C. I. (1995). Remote Triggering of Large Seismic Events in Mines: Evidence Based on the Spatial and Temporal Migration of Microseismic Events Along Increasing Stress Gradients. In R. Console & A. Nikolaev (Eds.), *Earthquakes Induced by Underground Nuclear Explosions: Environmental and Ecological Problems* (Vol. 4, pp. 353–374). Springer in cooperation with NATO Scientific Affairs Division.

Valley, B., M. Madjdabadi, B., Kaiser, P. K., & Dusseault, M. B. (2012). Monitoring mining-induced rock mass deformation using distributed strain monitoring based on fiber optics. In *European Rock Mechanics Symposium-EUROCK 2012* (p. 14). Stockholm, Sweden: International Society for Rock Mechanics.

Vorster, T. E. B., Soga, K., Mair, R. J., Bennett, P. J., Klar, A., & Choy, C. K. (2006). The Use of Fibre Optic Sensors to Monitor Pipeline Response to Tunnelling. In *GeoCongress 2006* (pp. 1–6). Reston, VA: American Society of Civil Engineers. doi:10.1061/40803(187)33

Wan, K. T. K., & Leung, C. K. Y. C. (2007). Applications of a distributed fiber optic crack sensor for concrete structures. *Sensors and Actuators A: Physical*, *135*(2), 458–464. doi:10.1016/j.sna.2006.09.004

Wan, K. T., Leung, C. K. Y., & Olson, N. G. (2008). Investigation of the strain transfer for surface-attached optical fiber strain sensors. *Smart Materials and Structures*, *17*(3), 035037. doi:10.1088/0964-1726/17/3/035037

Wang, B., Li, K., Shi, B., & Wei, G. (2008). Test on application of distributed fiber optic sensing technique into soil slope monitoring. *Landslides*, *6*(1), 61–68. doi:10.1007/s10346-008-0139-y

Wang, H. F., Gage, J. R., Fratta, D., Maclaughlin, M., Murdoch, L. C., & Tokunaga, T. (2010). Deep underground instrumentation and monitoring. In K. G. Sharma (Ed.), *ISRM International Symposium 2010 and 6th Asian Rock Mechanics Symposium - Advances in Rock Engineering* (pp. 46–57). New Delhi, India.

Wu, Z., Xu, B., Hayashi, K., & Machida, A. (2006). Distributed optic fiber sensing for a full-scale PC girder strengthened with prestressed PBO sheets. *Engineering Structures*, *28*(7), 1049–1059. doi:10.1016/j.engstruct.2005.11.012

Yang, Y., Annamdas, V., Wang, C., & Zhou, Y. (2008). Application of multiplexed FBG and PZT impedance sensors for health monitoring of rocks. *Sensors*, *8*(1), 271–289.

Yang, Y. W., Bhalla, S., Wang, C., Soh, C. K., & Zhao, J. (2007). Monitoring of rocks using smart sensors. *Tunnelling and Underground Space Technology*, *22*(2), 206–221. doi:10.1016/j.tust.2006.04.004

Yehia, S., Landolsi, T., Hassan, M., & Hallal, M. (2014). Monitoring of Strain induced by Heat of Hydration, Cyclic and Dynamic Loads in Concrete Structures using Fiber-Optics Sensors. *Measurement*, *52*, 33–46. doi:10.1016/j.measurement.2014.02.030

Yoon, H.-J., Song, K.-Y., Kim, J.-S., & Kim, D.-S. (2011). Longitudinal strain monitoring of rail using a distributed fiber sensor based on Brillouin optical correlation domain analysis. *NDT & E International*, *44*(7), 637–644. doi:10.1016/j.ndteint.2011.07.004

Zeng, X., Bao, X., Chhoa, C. Y., Bremner, T. W., Brown, A. W., DeMerchant, M. D., … Georgiades, A. V. (2002). Strain measurement in a concrete beam by use of the Brillouin-scattering-based distributed fiber sensor with single-mode fibers embedded in glass fiber reinforced polymer rods and bonded to steel reinforcing bars. *Applied Optics*, *41*(24), 5105–14.

Zhang, H., & Wu, Z. (2008). Performance Evaluation of BOTDR-based Distributed Fiber Optic Sensors for Crack Monitoring. *Structural Health Monitoring*, *7*(2), 143–156. doi:10.1177/1475921708089745

Zhang, W., Shi, B., Zhang, Y.-F., Liu, J., & Zhu, Y.-Q. (2007). The strain field method for structural damage identification using Brillouin optical fiber sensing. *Smart Materials and Structures*, *16*(3), 843–850. doi:10.1088/0964-1726/16/3/034

Zhao, X., Gong, P., Qiao, G., Lu, J., Lv, X., & Ou, J. (2011). Brillouin corrosion expansion sensors for steel reinforced concrete structures using a fiber optic coil winding method. *Sensors (Basel, Switzerland)*, *11*(11), 10798–819. doi:10.3390/s111110798

Zhao, X.-F., Li, L., Ba, Q., & Ou, J.-P. (2012). Scour monitoring system of subsea pipeline using distributed Brillouin optical sensors based on active thermometry. *Optics & Laser Technology*, *44*(7), 2125–2129. doi:10.1016/j.optlastec.2012.03.015

Zou, L., Bao, X., Ravet, F., & Chen, L. (2006). Distributed Brillouin fiber sensor for detecting pipeline buckling in an energy pipe under internal pressure. *Applied Optics*, *45*(14), 3372–7.

Zou, L., & Feng, M. Q. (2008). Detection of micrometer crack by Brillouin-scattering-based distributed strain and temperature sensor, *7004*, 700419–700419–4. doi:10.1117/12.785694

Zou, L., Ferrier, G. a, Afshar, S., Yu, Q., Chen, L., & Bao, X. (2004). Distributed brillouin scattering sensor for discrimination of wall-thinning defects in steel pipe under internal pressure. *Applied Optics*, *43*(7), 1583–8.

Appendix A: Conceptual modeling of gravity-driven displacement field around deep mines and related remote seismicity

A.1. Gravity-driven deformation

Stress changes due to creating an opening drops to small values (less than 5%) of far-field stress state at distances greater than five times the radius of the opening, although the details depend on the excavation shape, pre-mining stress state, and the presence of discontinuities (Brady & Brown, 2004), a region known as the excavation disturbed zone (EdZ). The stress change that could cause damage to the rock mass is even more closely confined to near the opening boundary, typically within one diameter of the excavation, known as excavation damage zone (EDZ). Therefore, the stress changes within the disturbed zone cannot contribute to damaging processes of the rock mass located at remote areas. However, when the stress transfer hypothesis, assumed to be responsible for such a phenomenon, is replaced by the deformation transfer process, remote events might be justified as the immediate rock mass around the opening moves toward the open space causing parts of the more distant rock mass to move in a domino-type process.

Rigid block movements and block deformation and failure will be combined in order to contribute to the overall rock mass deformation. The initial structure (fabric) of the rock mass, the properties of the joints and the nature of the perturbation induced by mining will dictate what will be the dominant rock mass response and how far from the mining perturbation displacement can propagate. Where rigid rock displacements are completely prevented, intact rock straining would be dominant. However, where movement is possible, Barton and Bandis (Barton & Bandis, 1982) explained that the deformation field is mostly controlled by the joint sets and individual joints.

A.2. Deformation transfer modeling

The main objective here is to understand various characteristics of the rock mass, including the block geometry and interlocking degree defined by joint set spacing, orientation, persistency, and joint stiffness, that influence displacement transfer. In turn, this will also help assess under which conditions intact rock damage or slip along a joint at far distances away from mining boundary can occur.

The deformation transfer pattern away from mining is simulated using UDEC™ considering a variety of parameter combinations. Apart from the effect of continuous joint set spacing and orientation, the persistency of joint sets, joint stiffnesses, presence of an old mine or highly stressed zones at higher level of current mining, and high extraction ratio are all considered in terms of how they might influence the displacement pattern and far-field shear slip events. UDEC™ has been selected for this study since it has the ability to explicitly deal with a large number of block in an assembly of block contacts.

A.2.1. Model setup

The general model geometry considers a 1000 m wide cross-section of the rock mass extending from 1000 to 2000 m depth, Figure 0-1. The lateral model displacement is constrained in the horizontal direction, while the bottom of the model is fixed in the vertical direction. A stress boundary, $\sigma_v = 27$ MPa and $\sigma_h = 50$ MPa, is also applied at the top of the model as if the model top is located at a depth 1000 m below the surface. Vertical and horizontal stresses increase linearly over the height of the model, so that the stresses at the bottom of the model become σ_v=54 MPa and σ_h=100 MPa.

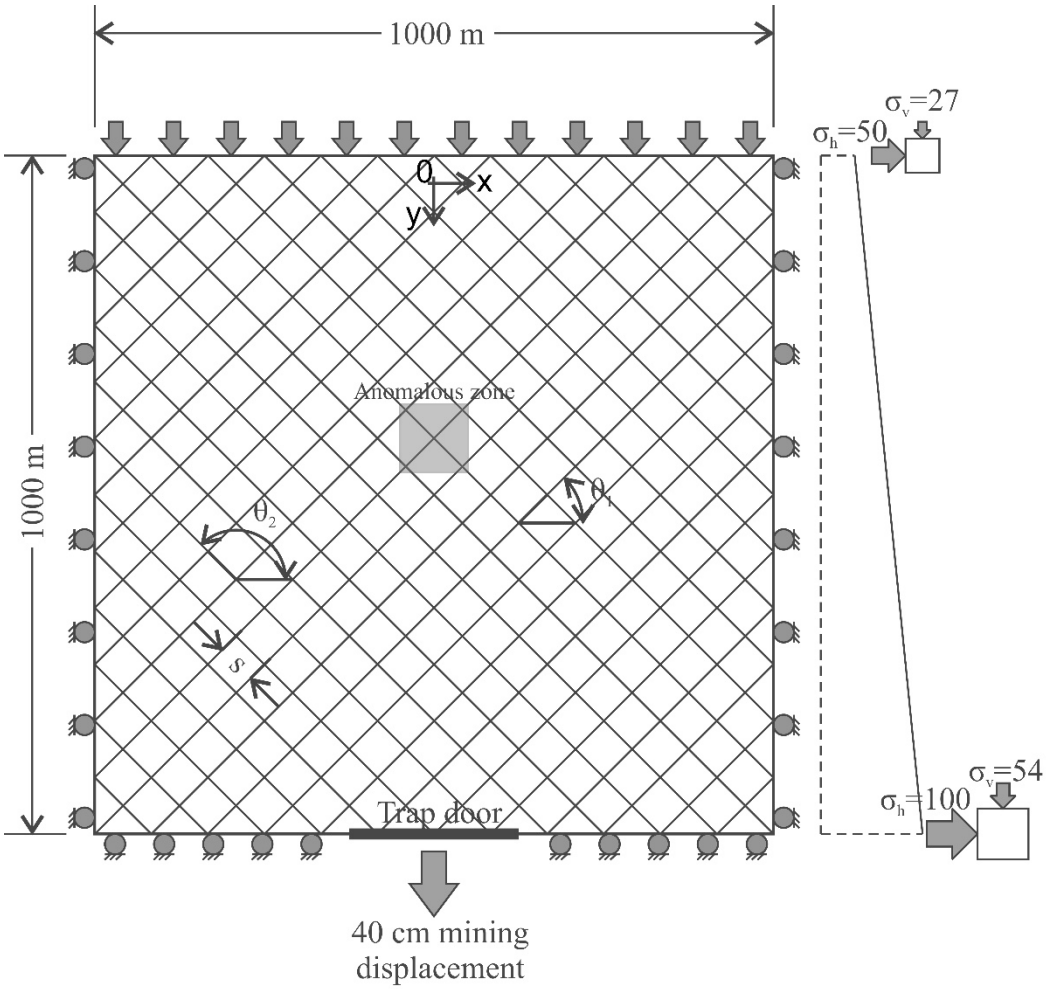

Figure 0-1. Model geometry for parametric study. Blocks might be of different shapes due to various joint geometrical characteristics. Mining simulation through displacement of various length of bottom boundary of the model.

Material properties used for almost all models are given in Table A0-1.

Table A0-1. Material properties for rock blocks and joints.

Properties	Rock	Joint	Backfill
Density (kg/m^3)	2700	-	1800
Young's Modulus (GPa)	75	-	500
Poisson's Ratio	0.22	-	0.25

Cohesion (MPa)	30	0	1
Friction Angle	40	36	33
Tensile Strength (MPa)	5	0	-
Normal Stiffness (GPa/m)	-	2-15	-
Shear Stiffness (GPa/m)	-	0.1-5	-

A.2.2. Modelling approach

After the discrete element block model is geometrically stipulated, it is brought to initial equilibrium; this represents the state of the rock mass before the beginning of mining. For this study, mining is not simulated through physical excavation of rock blocks within the model, but the ore extraction process is conceptually performed through a trap door model (Terzaghi, 1936). This means that a certain length of the bottom boundary (trap door) is displaced downward with a uniform displacement rate. The size of the trap door and the displacement rate both could implicitly simulate the convergence induced by an increasing extraction ratio. The size of trap door should be small compared to the bottom boundary; a size of one-fifth is enough so that boundary effects are not noticeable (Koutsabeloulis & Griffiths, 1989). A 200 m length of the bottom boundary of the model is considered as the trap door. The trap door was moved at a displacement rate of 1 m/s in most simulations for 0.4 seconds in order to simulate a 40 cm mining displacement.

Several parameters, mostly geometry related, are varied in order to follow the modeling objectives. In the first phase, fully persistent joint sets are included to create the rock block assembly. The first two models to study the block size effect are composed of two joint sets with 60° and 120° inclination from the horizontal. The joint spacing for the smaller-block model is 5 m and for the larger block size is 20 m. Later, three more models are considered with various inclinations including 0°-90°, 30°-150°, and 45°-135°, to study the effect of block shape (or joint set orientations). In addition, a single model with non-symmetric joint sets of 30-120 was made to simulate the potential tendency in displacement field due to presence of two different joint set orientations with respect to the horizontal.

In the next phase, the model geometry involves non-persistent joint sets, since it is a more realistic representation of the rock mass. The non-persistent models are also made with 60°-120° inclination for the comparison purposes with their corresponding persistent joint model. The next model physically involves simulation of an old backfilled excavation of 100×100 m at the mid height of the model before mining at the bottom started. Finally, the effect of higher extraction ratio on the displacement transfer process and shear slip events at far distances will be evaluated through a wider trap door mining boundary of 400 m.

A.3. Results and discussion

A.3.1. Block size

Rock block size effect on the displacement transfer to locations away from active mining was studied with two models both containing two joint sets one with 60° and the other with 120°

inclination from horizontal. After examining both rock masses for similar stiffness joint stiffness were reached at [3, 2] and [1, 0.3] ([K_n, K_s]) GPa/m for small and large blocks, respectively, yielding 22.1 and 21.7 GPa rock mass stiffness. It should be noted that for rock mass stiffness evaluation all input parameters except joint stiffnesses were identical.

Error! Reference source not found. shows displacement vectors for these two models at two different mining displacement stages. At early stages of mining (e.g. 10 cm) displacement vectors seem to be quite similar for both models. However, at the same mining displacement the displacement reaches shallower depths with a larger block size. This is actually due to the fact that the block size in the second model is four times higher than in the first model; therefore even small displacements at the beginning of trapdoor movement result in displacement transfer to higher levels with larger blocks.

This trends gradually changes as more mining displacement (e.g. ≥20 cm) is allowed at the trapdoor. As shown in Figure 0-2 for 40 cm trapdoor displacement, the displacement transfer process to shallower levels is more limited to depths closer to the trapdoor in the case of larger blocks. For an example, with smaller blocks 5 cm displacement traveled vertically up to depths -430 m, while this happened at the depth of -600 m for larger blocks.

This can be explained by Terzaghi's stress arching effect (Terzaghi, 1936). Displacement of the trapdoor induces a vertical stress relief in the immediate rock mass above it, as shown in the vertical stress contour at 10 cm displacement in Figure 0-2, and it transfers to the rock mass located at the sides of the trapdoor. Since the rock mass column above the trapdoor is under vertical expansion a lateral contraction occurs due to presence of the springs at rock block boundaries, i.e. at the joints. This lateral shrinkage in turn increases horizontal stress, resulting in more confinement of the rock mass.

It is noticed that at higher trapdoor displacements vertical stress decrease is restricted to deeper levels for larger blocks compared with smaller blocks, as shown for vertical stress at 40 cm displacement in Figure 0-2. This occurs because a detaching wedge containing a number of rock blocks above the trapdoor is under formation in the larger block model. Since in this model the number of joints along a vertical scanline is much less than in the small block model, the same vertical expansion in both models has to be accommodated with fewer joints in the larger block model, resulting in the quicker formation of the detaching wedge. This is why the horizontal stress increases more in the model with larger blocks and creates higher confinement to the rock mass, preventing higher displacements to transfer to the same depths as in the small block model. Also note that since we are examining the same stiffness of rock masses, the joint stiffness in the larger blocks is lower, so the faster formation of the detaching wedge is partly due to this difference.

5 m spacing 20 m spacing Legend

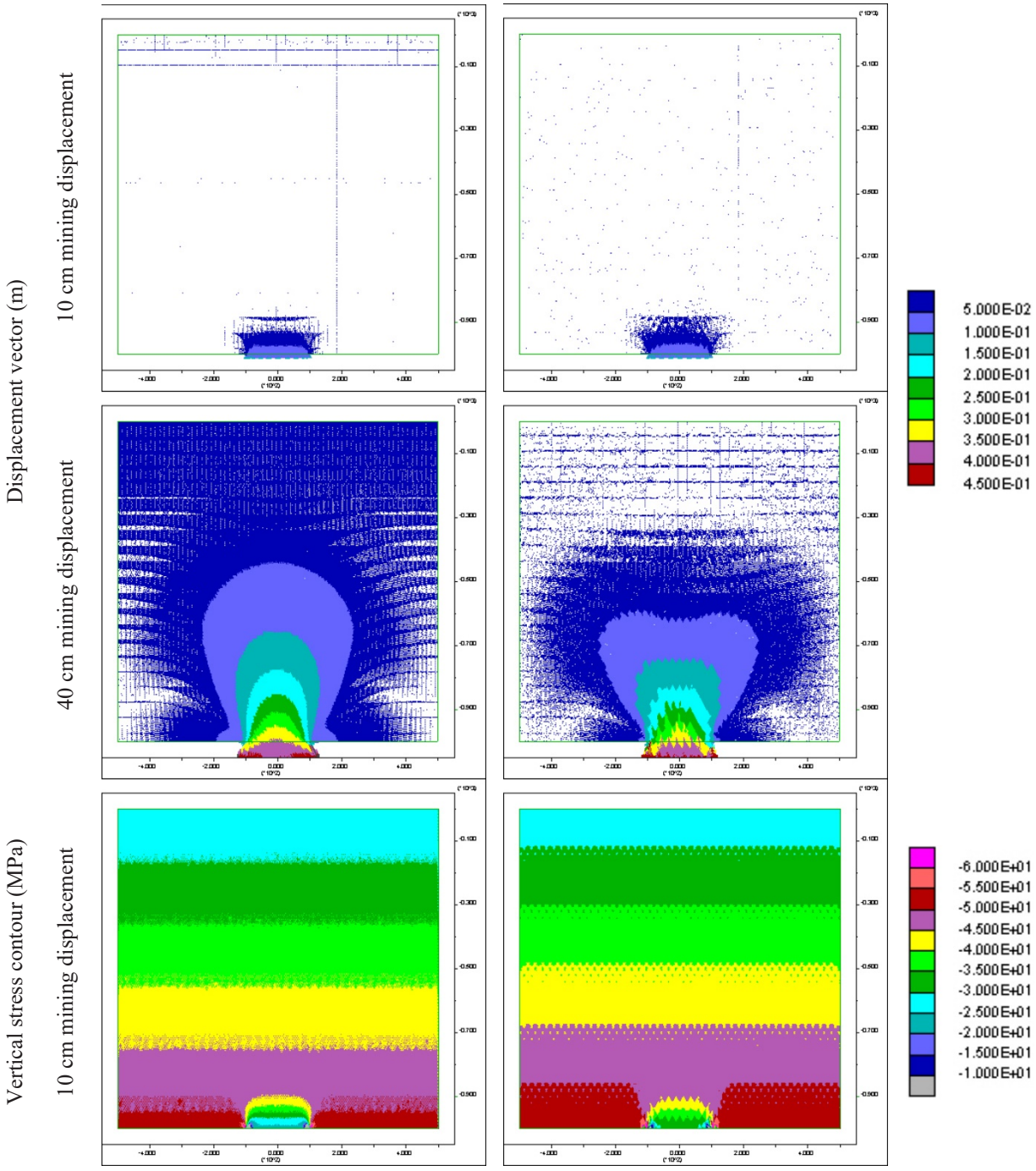
Displacement vector (m)
10 cm mining displacement
40 cm mining displacement
5.000E-02
1.000E-01
1.500E-01
2.000E-01
2.500E-01
3.000E-01
3.500E-01
4.000E-01
4.500E-01
Vertical stress contour (MPa)
10 cm mining displacement
-6.000E+01
-5.500E+01
-5.000E+01
-4.500E+01
-4.000E+01
-3.500E+01
-3.000E+01
-2.500E+01
-2.000E+01
-1.500E+01
-1.000E+01

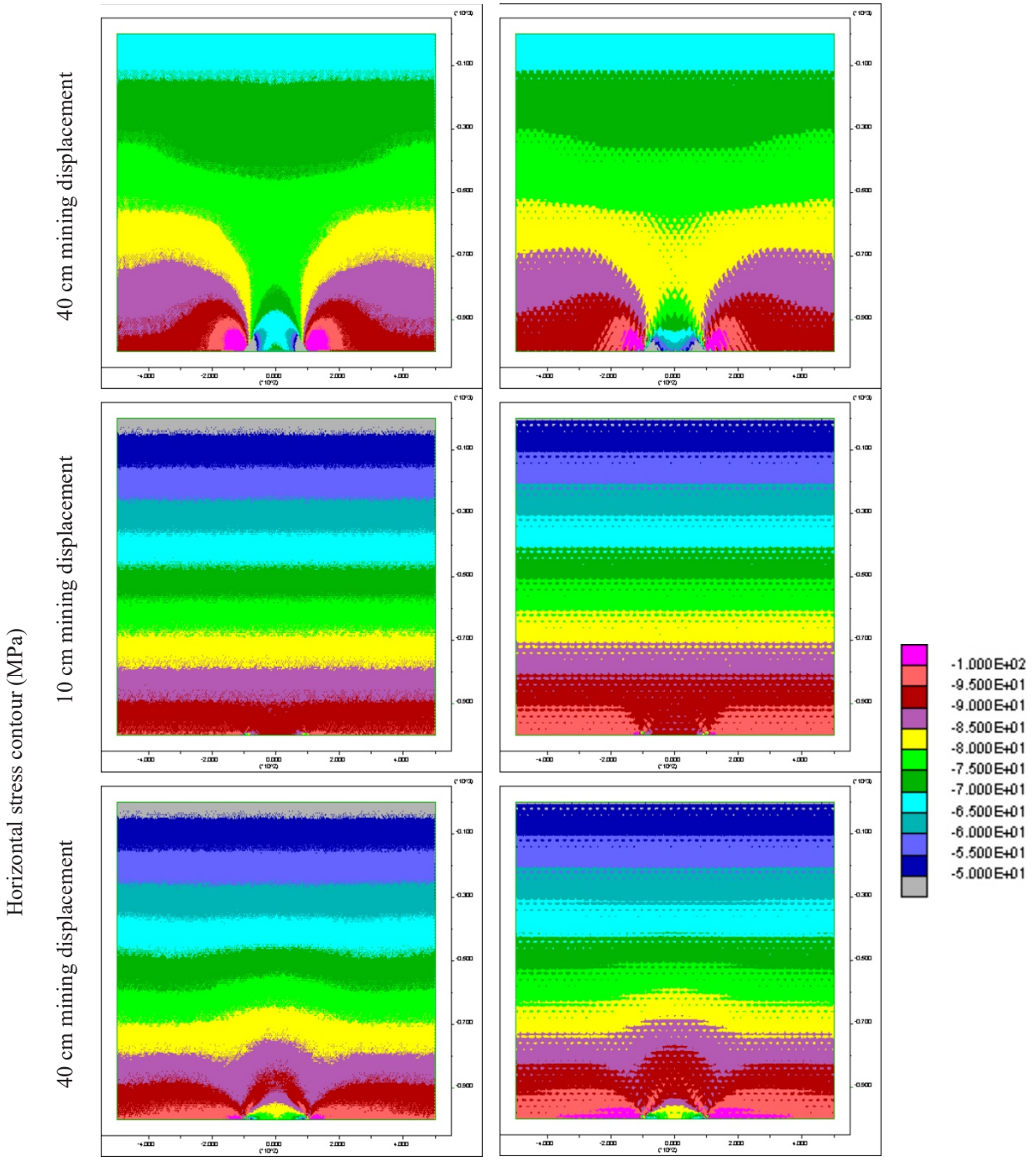

Figure 0-2. Displacement vectors, vertical and horizontal stress contours at 10 and 40 cm mining displacement for small and large blocks model. Displacement transfer to higher levels is more restricted for larger blocks model due to effect of stress arching.

Shear displacements as large as 1 mm along joints can happen at a distance as far as 515 and 755 m from the center of the trapdoor for small and large block models, respectively. However, these displacements are not large enough to cause a plastic shear slip along any of joints at far locations away from the trapdoor. Actually, only a small portion (<1% of entire joints within

model) of joints adjacent to the trapdoor experienced shear slip after final mining displacement, as shown in Figure A-3. Shear slip, when shear stress exceeds shear strength, evolves from the immediate joints, at the trapdoor away from it as more displacement occurs. Joints slipped when at least 17 and 52 mm shear displacement accumulated along the joint. Therefore, although the block size has a significant influence on the displacement field to quite a far distance away from mining, no remote shear seismic event may be expected with the current rock mass configuration.

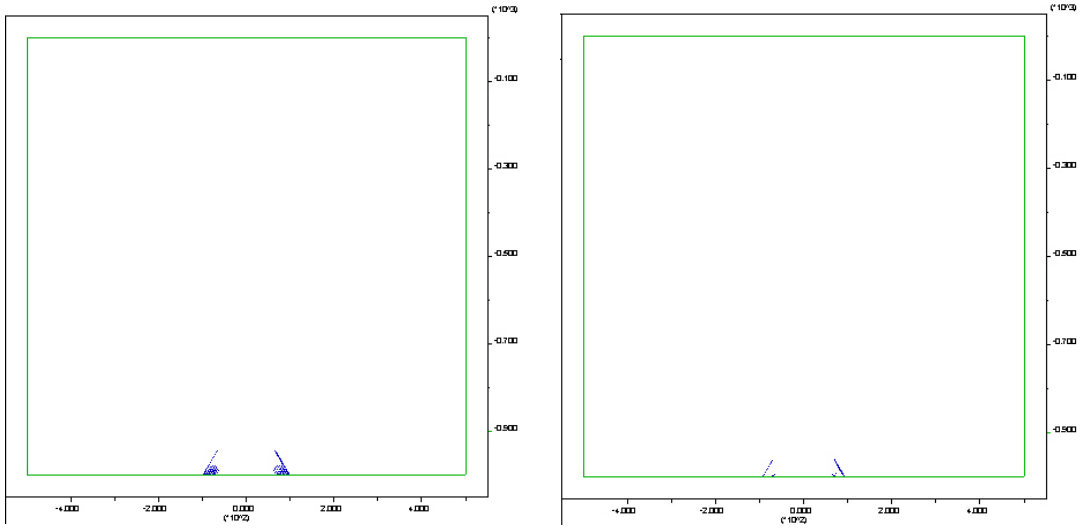

Figure A-3. Spatial distribution of joints that plastically slipped after 40 cm mining displacement. Less than 1% of entire existing joints went to slip located at the closest distance to the active mining.

A.3.2. Joint set orientation

In addition to the preceding 60°-120° inclined joint sets model, three more models with joint set orientations different from one another were constructed, all with 5 m joint spacing. In these models normal and shear joint stiffness ranging from 5 to 7 and 4 to 5 GPa/m, respectively, were used to create rock masses of similar stiffness, i.e. approximately 22 GPa. The trapdoor size and displacement and other material properties remained the same as the models in Section A.3.1.

Displacement fields for these models are shown in Figure A-4. The displacement field grew mostly vertically with vertical joint sets so that displacement bulbs (i.e. similar displacement range fronts) had the largest dimension ratio (i.e. vertical to horizontal extension of a displacement front) of 1.3 with the least rock mass volume laterally affected compared to other modes. As the vertical joint set rotated to shallower orientations, the displacement field developed more laterally so that, for example, the 5 cm displacement bulb achieved a maximum width of almost 500 m with the least steep joint sets, i.e. 30°-150°. In this case the dimension ratio of the displacement bulb was just below 1, implying that the displacement front grew uniformly in all directions, similar to a circle. It should be noted that among all models the displacement field transferred to the shallowest level most with the 60°-120° inclined joint sets model due to the appropriate orientation of the joints to allow displacements to move upward.

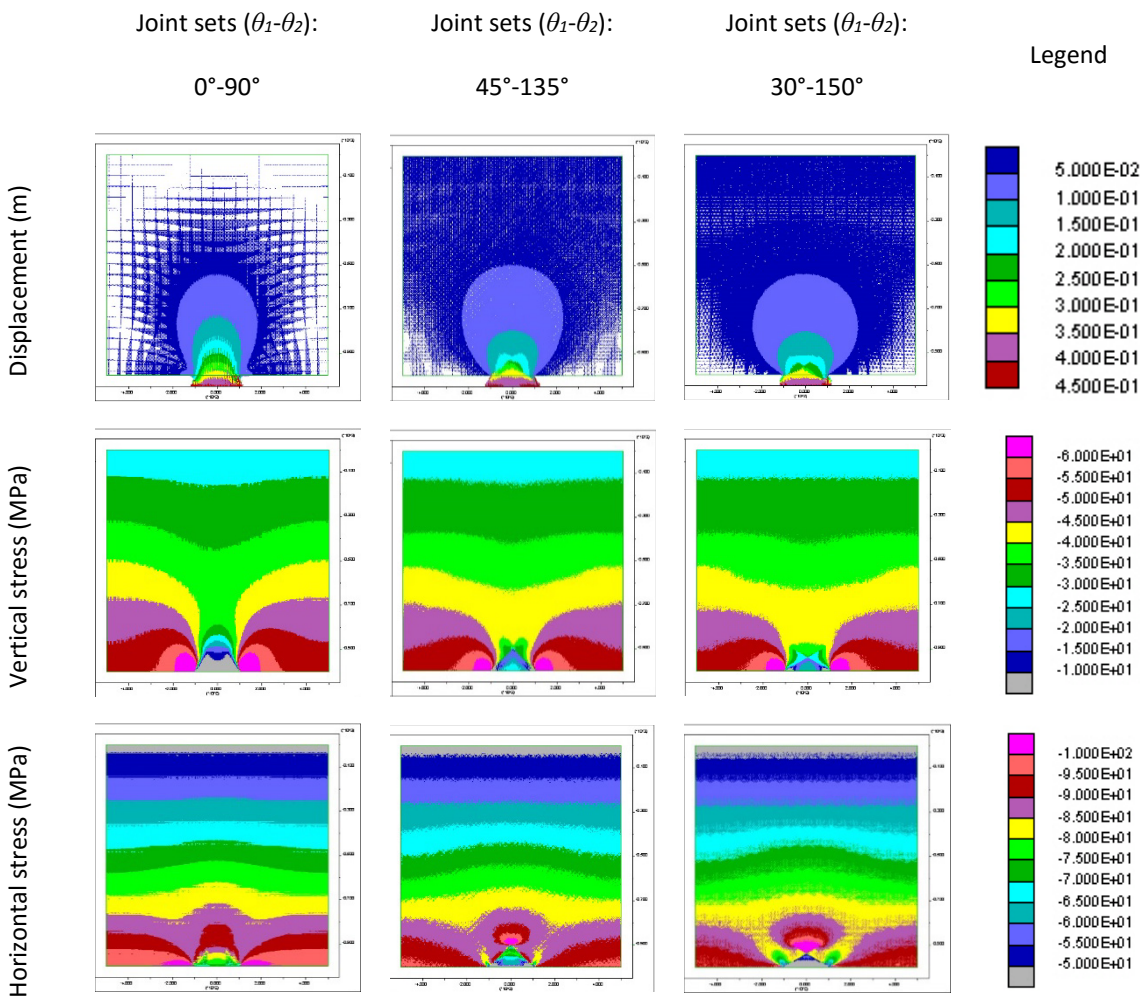

Figure A-4. Displacement vectors, and vertical and horizontal stress contours for three different joint set orientation models. Stress arching as noticed from horizontal stress contours prevents higher displacements transfer to shallower depths

Higher displacement fronts, however, did not follow the same growth pattern as for lower displacement ranges. Over the course of mining (i.e. trapdoor movement) higher displacements were more restricted to depths closer to the mining boundary, particularly with lower angle joint sets, e.g. refer to 20 cm displacement front shown in Figure A-4. This was due to the fact that a wedge of rock blocks was formed as mining displacement increased. This wedge was induced at lower displacements for the shallower joint set of 30°-150° among other models. This was also clear from vertical stress contours where, after 40 cm mining displacement, the decrease was less for the latter model from almost 110 m above trapdoor to higher levels. Horizontal stress for all models also increased above the trapdoor during mining so that it was maximised at the top of the wedge resulting in more confinement in the rock mass and consequently limited the gravity-driven displacements. It is worth nothing that the very low horizontal stress at the immediate site of the trapdoor for 30°-150° joint set model represents the separation of a roof wedge from the rest of the rock mass. Note that the steeper joint sets will result in the delayed formation of the detached zone,

i.e. while after 25 and 30 cm mining displacement the detachment started for 30°-150° and 45°-135° models, respectively, it has not yet occurred after 40 cm displacement in the 60°-120° model.

A.3.3. Non-persistent joint set

A more realistic rock mass rarely includes through-going persistent joint sets as described in the two previous Sections. Joints of different scales in terms of their spatial extent are always present in a typical hard rock mass. The various spatial extension of joints can be expressed with their persistency, particularly in 2D, along a line. This section provides the results from modeling of a rock mass containing non-persistent joints.

To this end, the rock mass model with 60°-120° joint sets in Section A.3.1 was recreated with introduction of persistency for each joint set. In this case joint lengths were set in range varying from 20 to 60 m instead of being of continuous length over the model. Upon the construction of the model, the persistency of the rock mass joints was computed based on the joint length ratio. Here, the cumulative length of all joints of a certain inclination in the non-persistent model was divided by the sum of those in the persistent joint model. Accordingly, the persistency was found to be 73% and 60% for 60° and 120° joint sets, respectively.

Fully persistent joint sets created a rock mass with blocks that have more freedom to displace and rotate, while as soon as non-persistency is involved in the rock mass formation the interlocking degree increases, resulting in less chance to deform when any change is induced. This is because block sizes vary greatly and their shapes will not be near regular. **Error! Reference source not found.** shows the geometry of the rock mass with a non-persistent joint set. It should be noted that joint sets in this model were assigned different stiffness than was used in the persistent joint model to obtain the same rock mass stiffness in both models.

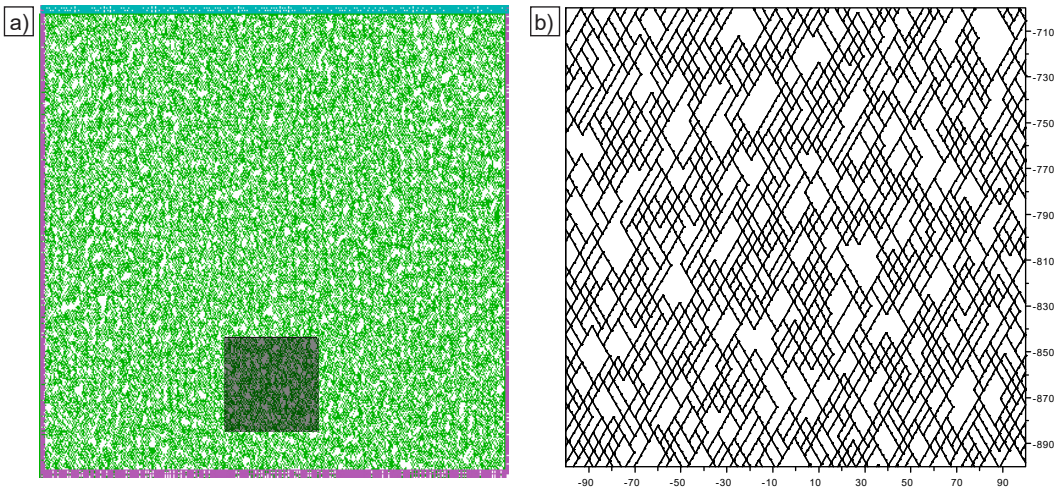

Figure 0-5. The modeled rock mass with non-persistent joint sets (a) and a magnified view of the shaded area for a better clarity (b). 60° joint set with persistency 73% and 120° joint set with persistency 60%.

While the displacement field grew uniformly in space in the persistent joint model, for this model, as shown in Figure 0-5. of various sizes were distributed all over model. Actually, the displacement pattern can be seen an intermediate state to the displacement fields for models

presented in Section A.3.1. While similar displacement transferred to the same depths when compared with the small block size model, the lateral extension of displacement field over the width of the model resembled that for the larger block size model.

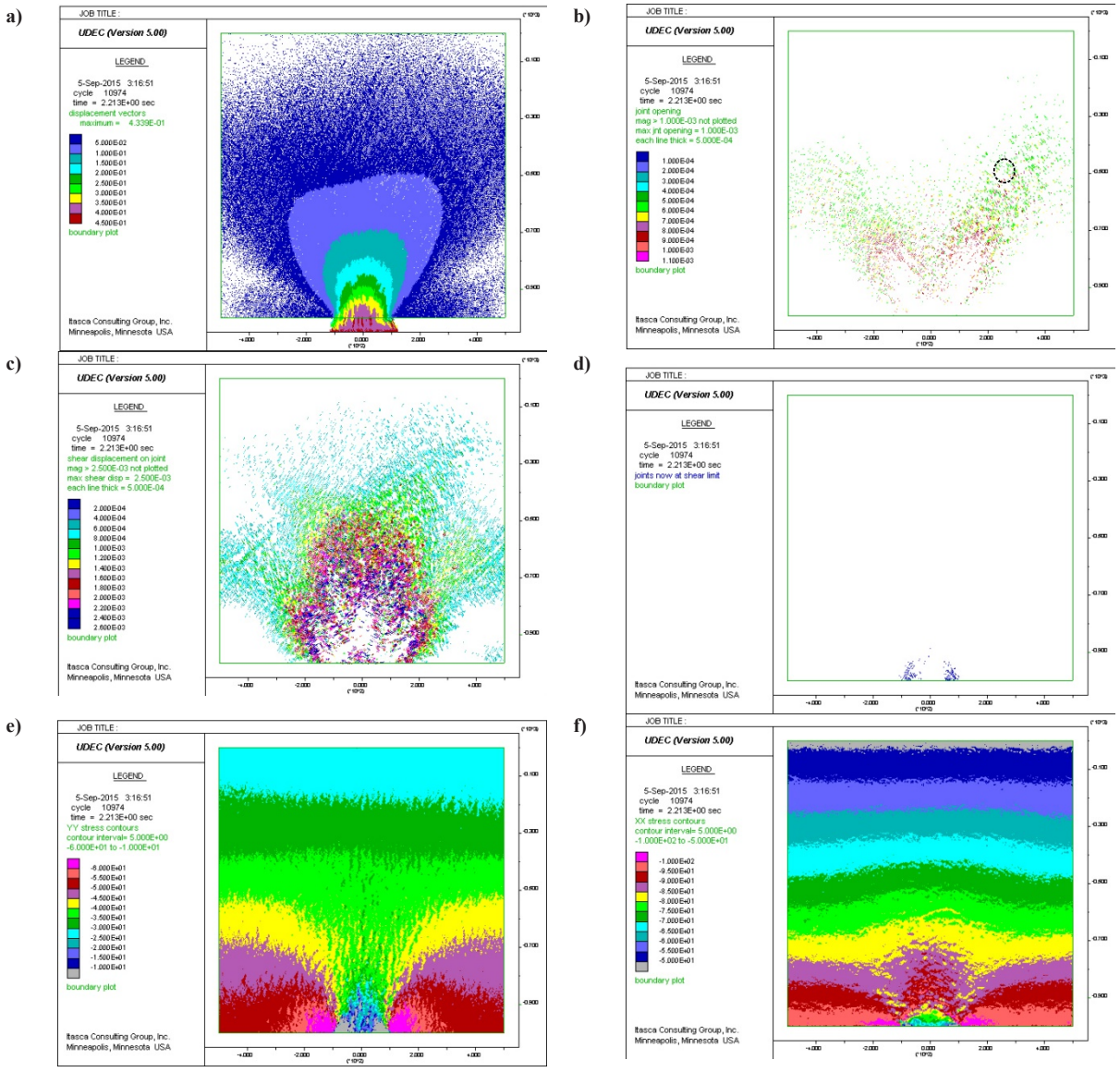

Figure A-6. Displacement vectors (a), joint opening (b) and shear displacement (c), shear slip (d) along with vertical € and horizontal (f) stress contours for the non-persistent joint model after 40 cm trapdoor displacement

The effect of non-persistency of joint sets is better understood by examining the joint displacement field. Both joint opening and shear displacement had a non-uniform pattern over the entire model. It can be seen that joints at a certain location, e.g. within the dashed circle in the joint opening plot, experienced a wider range of opening (0.4-1 mm), while in the continuous joint set model joints within the same location had a much more limited range of opening (0.6-0.7 mm). In this case, one can expect some joints at shallower depths go to higher shear displacement than some other joints at deeper levels. Therefore, a gradually increasing gradient of displacement does not exist when going deeper within a rock mass with non-persistent joints.

More interestingly, shear slip distribution at this model was not uniformly distributed at a certain mining displacement step, as shown in the slip plot in **Error! Reference source not found.** after 40 cm mining. Although slip events did not occur significantly far from the mining boundary, it happened that joints at farther distances from the trapdoor slipped, whereas the deeper joints required more displacement to touch the failure envelope. Such a scattered slip distribution came from the non-uniform horizontal and vertical stress distribution due to non-uniform rock block movement as mining displacement occurred. As shown in Figure A-6, horizontal and vertical stresses significantly varied for neighboring joints. There were joints that experienced an increase in normal stress and a reduction in shear stress, while at the same time normal stress fell and shear stress rose (favorable conditions for slip) at nearby joints.

A.3.4. Conditions with extraction above current mining level

All parameters considered in models presented so far did not cause an odd shear slip along any joint at distances far away from mining boundary, although in the last section it was shown that the slip distribution could occur non-contiguously with non-persistent joint sets. In all cases, the extraction ratio was zero above the mine, a condition that rarely correspond with reality as mining typically starts from the tom and progresses downward, creating a wedge of low ER at higher elevations. Therefore, conditions of pre-existing zone of high shear stress and/or old mining areas with low extraction ratio at some distance from the current mining must be considered. Here, we consider the latter case (extraction above the trap-door) for the next step to see how the displacement field changes and if remote seismic shear slip can be simulated.

In underground mining it frequently happens that two or more stopes or mining blocks are extracted but with a time difference. The model for simulation of this situation was the same model used in Section A.3.3, except that a region of 100 m×100 m in the middle of the model from -450 to -350 m above the trap door was first excavated and then backfilled with cemented sand fill. The model then was brought to equilibrium before applying mining displacement.

The displacement field after backfilling of the old mine and before starting mining at the bottom boundary is shown in Figure 0-7**Error! Reference source not found.**. A large rock mass volume at distances as far as 550 m away from the mine was displaced up to 5 cm by ore extraction and backfilling. The overall direction of rock blocks' movement was horizontal toward the excavation. This was as a result of high horizontal stress initially assigned to the rock mass. Also, horizontal stress changed after backfilling and high stresses were concentrated below and above the square region of the mine, resulting in plastic failure of many of intact rock blocks.

Furthermore, all the rock mass surrounding the old mine experienced high shear displacement (>>2.5 mm, i.e. the maximum value shown in Figure 0-7). Even joints located at a distance of three times the dimension of the mine had a shear displacement of 2.5 mm. Such a high shear displacement caused many joints, particularly close to the top and bottom of the excavation, to go to a condition of plastic shear slip. The slip distribution in the surrounding rock mass was not

uniform, but it seems it had a random pattern according to the locations where the maximum shear displacement occurred, as also seen in Section A.3.3.

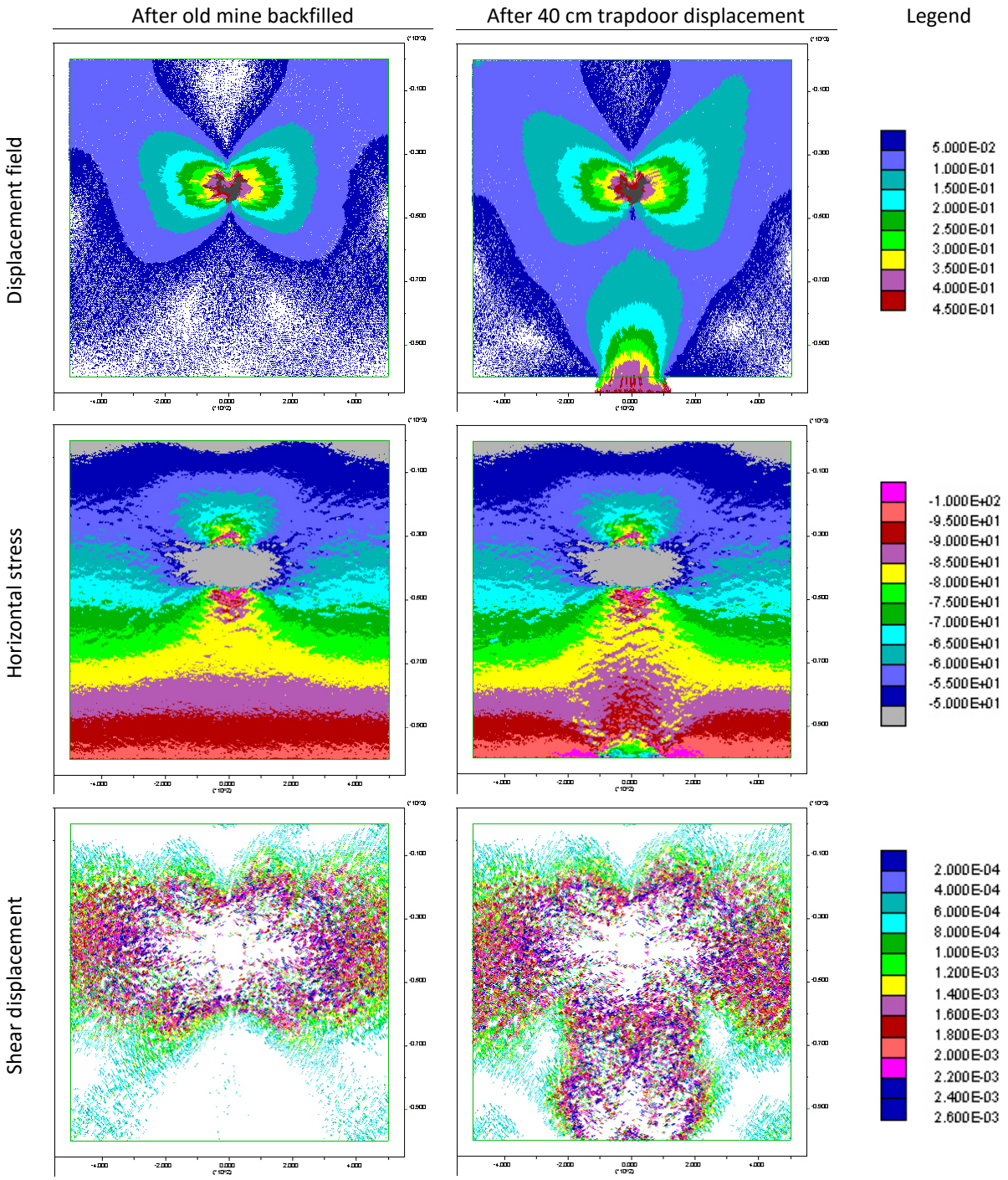

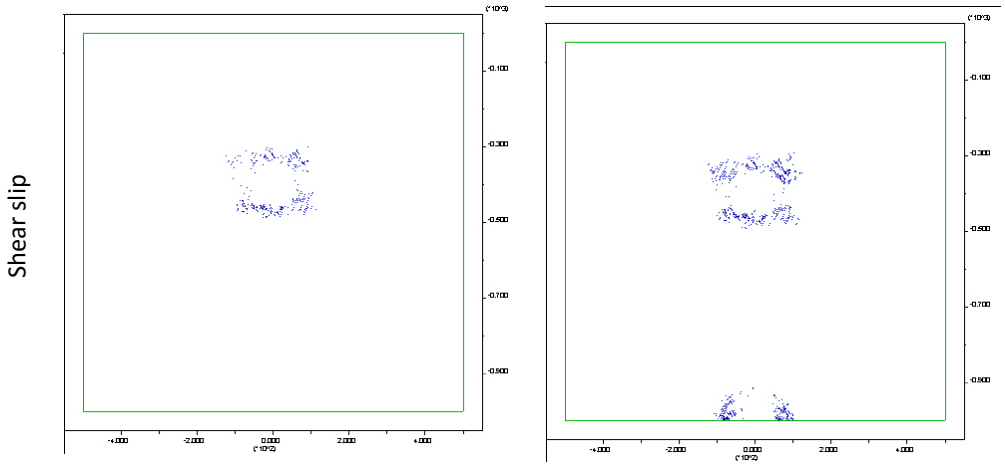

Figure 0-7. Displacement vectors, horizontal stress contours, shear displacement, and shear slip along joints after the extraction and backfilling of the old mine and after 40 cm trapdoor displacement.

After the model reached an equilibrium following backfilling of the old mine, the trapdoor was applied a 40 cm displacement to simulate main mining activity. Figure 0-7 also shows the same plots for the model after 40 cm mining displacement as shown for the backfilled mine. In general, in comparison with model in Section A.3.3, similar displacements transferred slightly to higher levels with the presence of a backfilled excavation before mining, particularly when the displacement front due to trapdoor movement reaches levels already affected by the old mine. As soon as the trapdoor moved, e.g. 5 cm, the displacement field at far distances away from the trapdoor even above the old mine changed so that the extent of each displacement front grew. The final pattern of displacement after 40 cm mining shows that rock blocks became less constrained to displace. This can be viewed as a result of a rock mass weakening effect arising from the influence of the pre-existing mine.

With respect to the horizontal stress, it increased upon movement of the trapdoor while non-uniformly distributed within the rock blocks above the trapdoor, the same as model in Section A.3.3. However, it can be seen that scattered higher horizontal stresses reached shallower depths close to the bottom and top of the old mine. This was due to the pre-existing mined excavation surrounded with already highly stressed rock mass, so that more rock blocks entered a higher induced stress range as the trapdoor displacement continued.

The interesting point is that many more joints around the backfilled opening slipped in shear after 40 cm mining displacement, apart from those that had slipped joints adjacent to the trapdoor. It should be noted that none of the joints located between these two zones of shear slip showed plastic slip. However, the blocks displaced vertically under gravity. Thus, gravity driven displacements occurred without shear slip. In addition, since the rock mass around the old mine had already high shear displacement, upon the trapdoor movement more shear displacement was accommodated within these joints.

A.4. Conclusion

The modeling results showed that that with large massive blocks stress arching can happen and prevent the displacement propagation to farther distance from active mining. If there are more joint sets or random joints or if the intact rock is low strength that can break easily, the arching might not occur and the displacement transfer can reach to remote locations. Therefore, remote seismicity in not possible if there is a single mining zone because arching is developed, unless critically stressed geological structures such as faults exist.

On the other hand, in the absence of such marginally stable structures (i.e. faults), remote seismicity can happen only if stacked mining zones at different levels in the rock mass exist such that the rock mass is already disturbed and softened to some extent. Accordingly, displacement-driven stress changes can propagate to remote location.

This appendix shows that gravity-driven displacements leading to remote seismicity can be a valid hypothesis under certain circumstances. When mining blocks with previous extraction already exist at higher levels underlying extraction can affected the disturbed rock mass surrounding those previous mining zones resulting in a remote seismicity.

Appendix B: Results from Other Tests

B.1. Clamping Effect

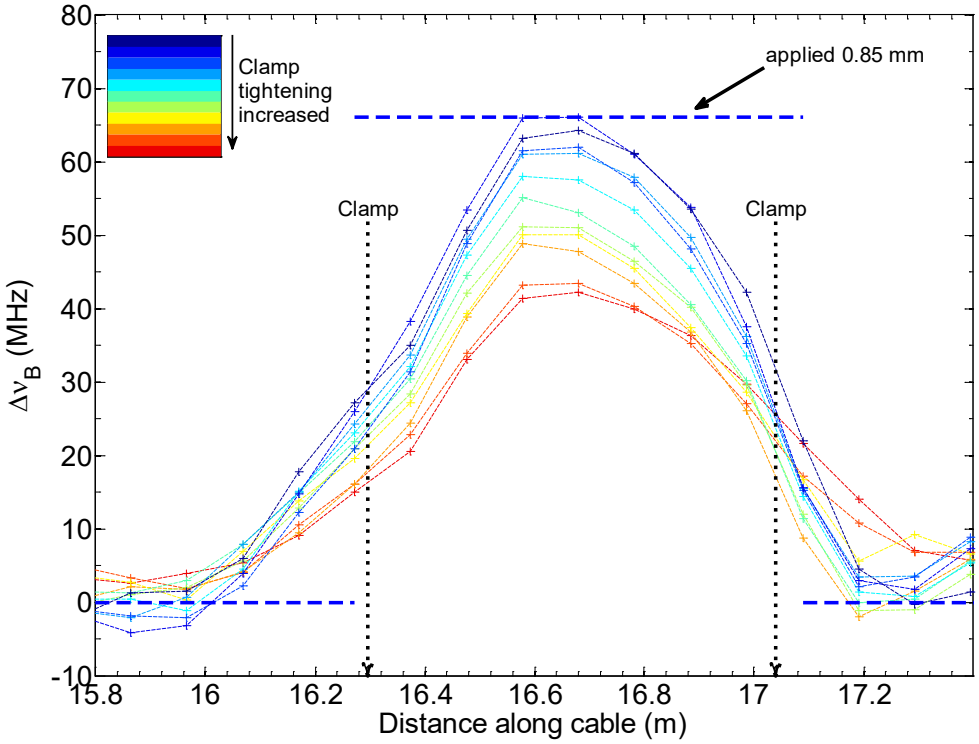

Figure B-1. Stretching a 60 cm length of SMARTProfile™ to 0.85 mm followed by increasing the clamping force and its effect of the frequency registration

B.2. Loading – Unloading Response in Tension

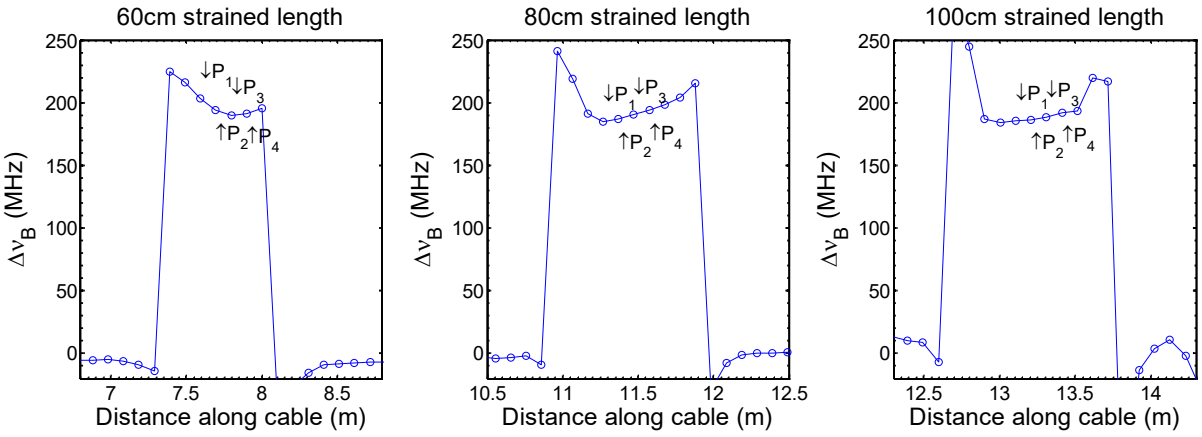

Figure B-2. Three different strained lengths including 60, 80, and 100 cm for loading-unloading response of the DiTeSt™

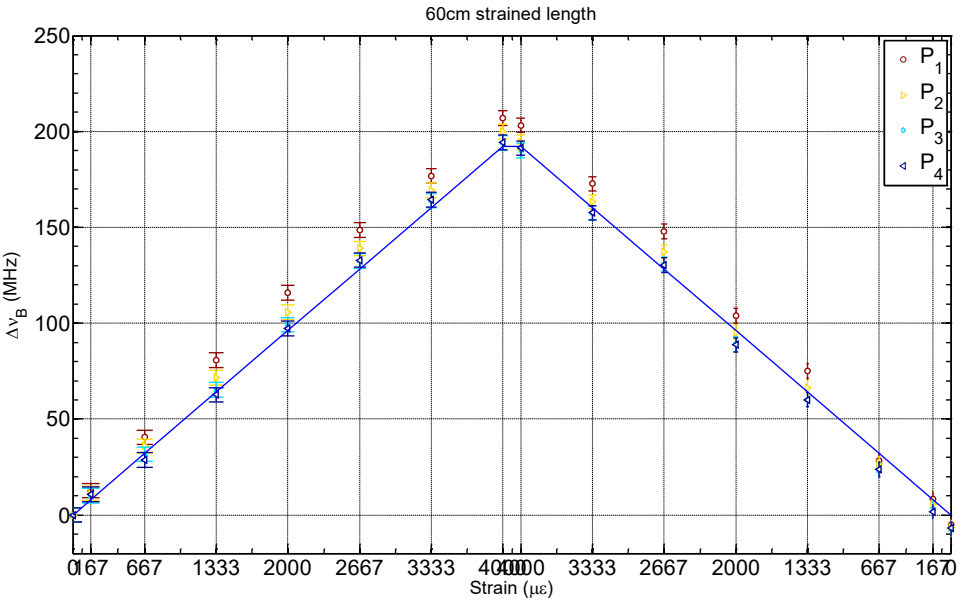

Figure B-3-a. Loading-Unloading response of the DiTeSt™ for a 60 cm strained length of SMARTProfile™

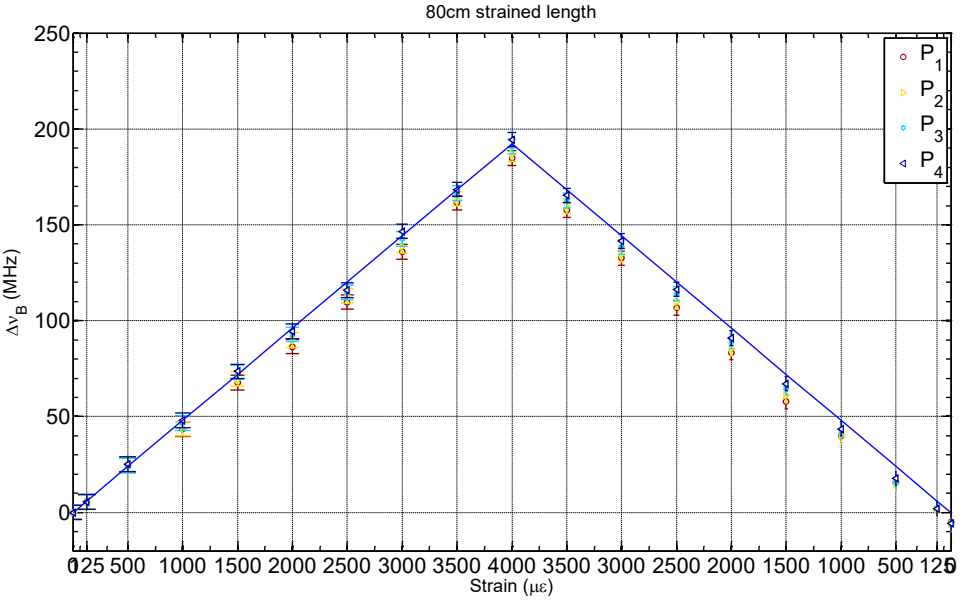

Figure B-3-b. Loading-Unloading response of the DiTeSt™ for a 80 cm strained length of SMARTProfile™

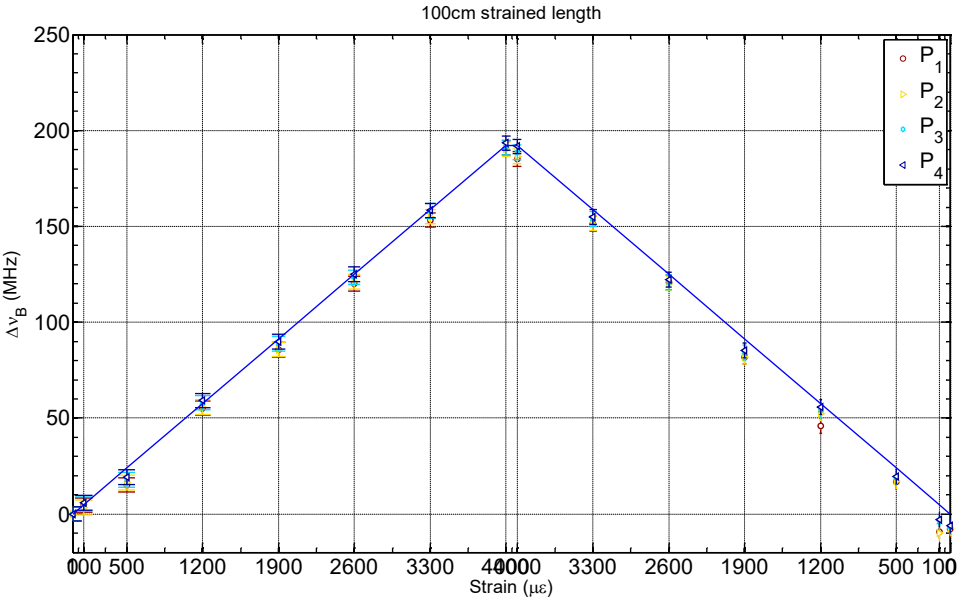

Figure B-3-c. Loading-Unloading response of the DiTeSt™ for a 100 cm strained length of SMARTProfile™

B.3. Glued Cable in Tension to Simulate Debonding Process

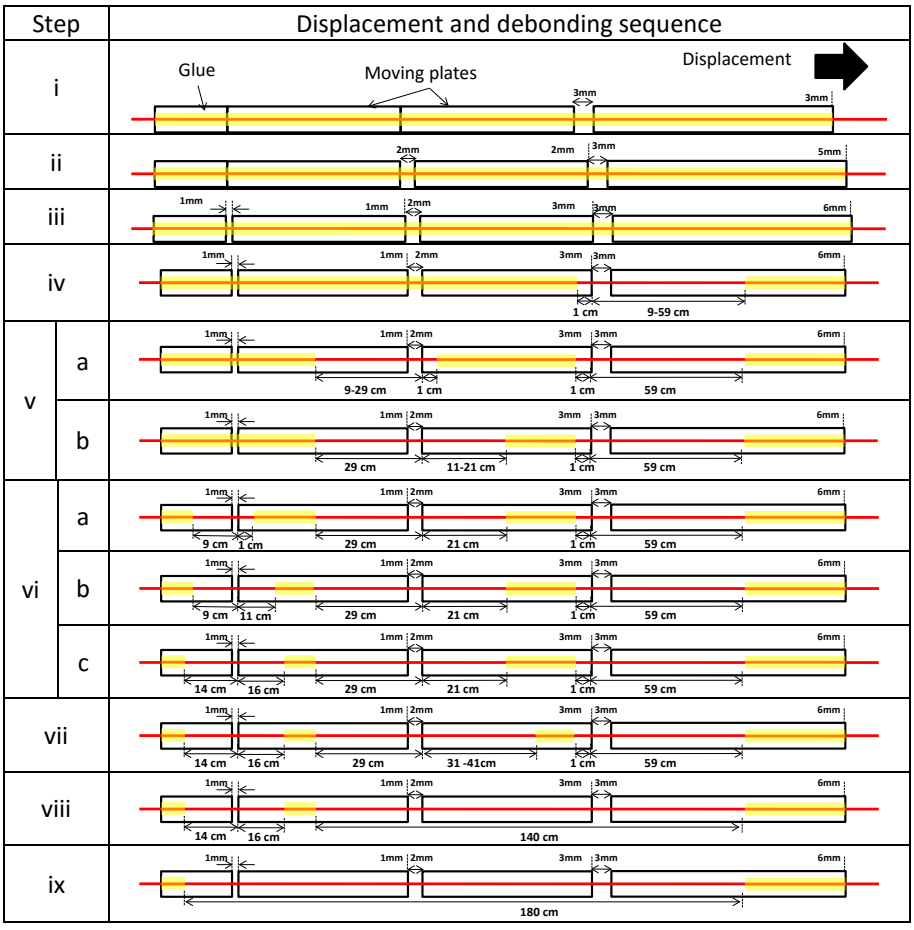

Figure B-4. The displacement and debonding sequence of the glued SMARTProfile™ on the tension test setup

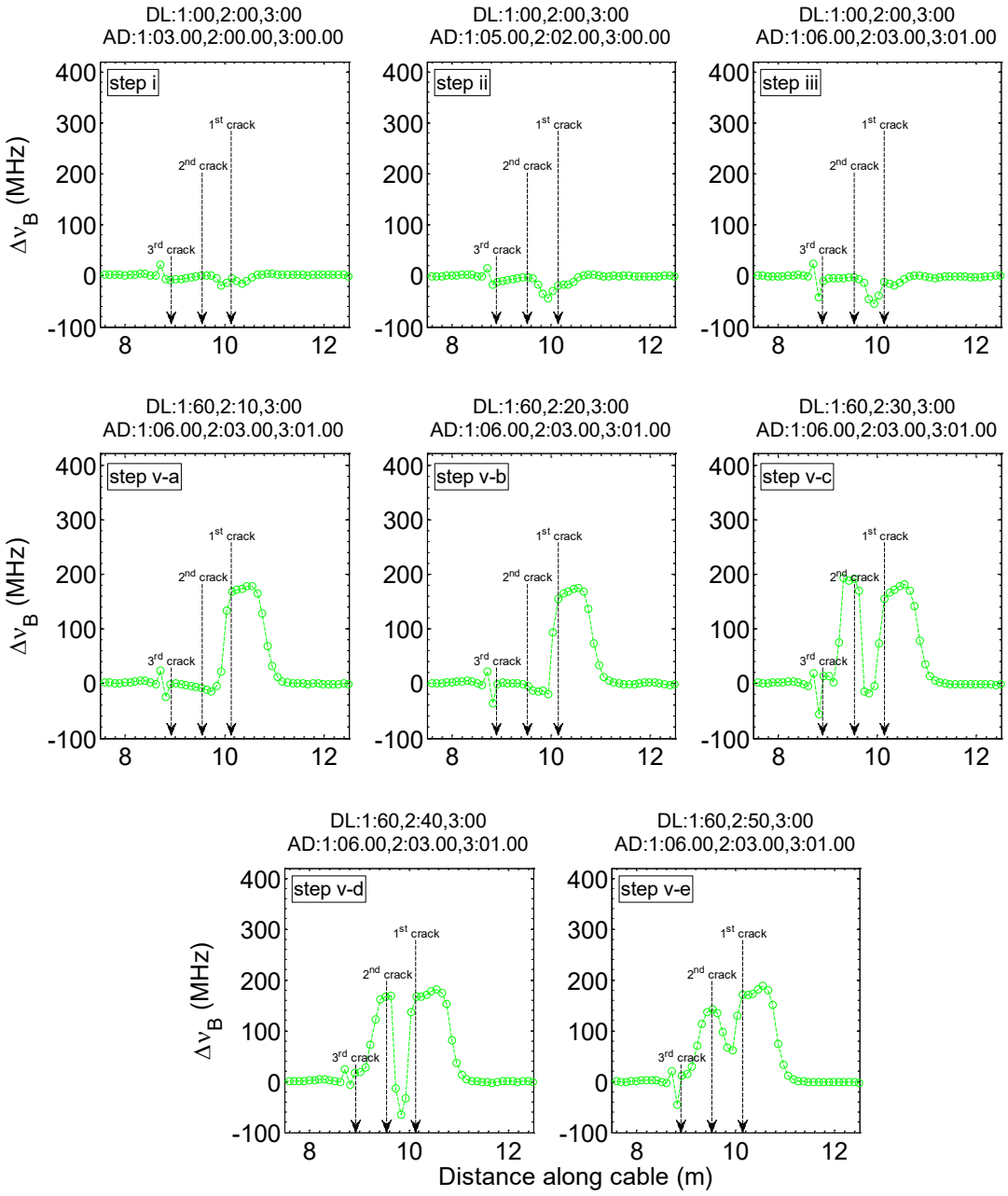
DL:1:00,2:00,3:00
AD:1:03.00,2:00.00,3:00.00
step i
DL:1:00,2:00,3:00
AD:1:05.00,2:02.00,3:00.00
step ii
DL:1:00,2:00,3:00
AD:1:06.00,2:03.00,3:01.00
step iii
DL:1:60,2:10,3:00
AD:1:06.00,2:03.00,3:01.00
step v-a
DL:1:60,2:20,3:00
AD:1:06.00,2:03.00,3:01.00
step v-b
DL:1:60,2:30,3:00
AD:1:06.00,2:03.00,3:01.00
step v-c
DL:1:60,2:40,3:00
AD:1:06.00,2:03.00,3:01.00
step v-d
DL:1:60,2:50,3:00
AD:1:06.00,2:03.00,3:01.00
step v-e
1st crack
2nd crack
3rd crack
Δν_B (MHz)
Distance along cable (m)

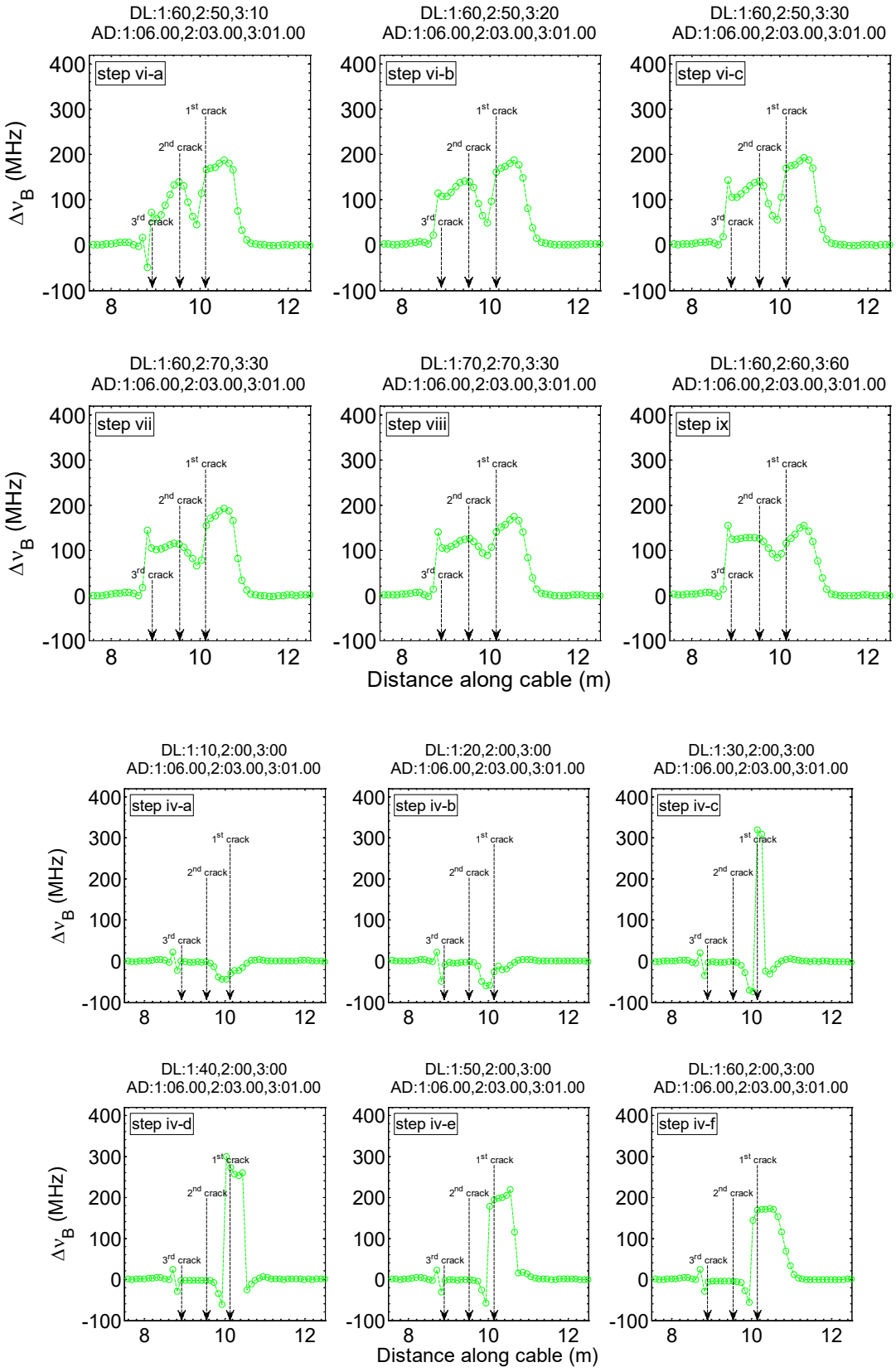
DL:1:60,2:50,3:10
AD:1:06.00,2:03.00,3:01.00
step vi-a
DL:1:60,2:50,3:20
AD:1:06.00,2:03.00,3:01.00
step vi-b
DL:1:60,2:50,3:30
AD:1:06.00,2:03.00,3:01.00
step vi-c
DL:1:60,2:70,3:30
AD:1:06.00,2:03.00,3:01.00
step vii
DL:1:70,2:70,3:30
AD:1:06.00,2:03.00,3:01.00
step viii
DL:1:60,2:60,3:60
AD:1:06.00,2:03.00,3:01.00
step ix
DL:1:10,2:00,3:00
AD:1:06.00,2:03.00,3:01.00
step iv-a
DL:1:20,2:00,3:00
AD:1:06.00,2:03.00,3:01.00
step iv-b
DL:1:30,2:00,3:00
AD:1:06.00,2:03.00,3:01.00
step iv-c
DL:1:40,2:00,3:00
AD:1:06.00,2:03.00,3:01.00
step iv-d
DL:1:50,2:00,3:00
AD:1:06.00,2:03.00,3:01.00
step iv-e
DL:1:60,2:00,3:00
AD:1:06.00,2:03.00,3:01.00
step iv-f
1st crack
2nd crack
3rd crack
Δν_B (MHz)
Distance along cable (m)

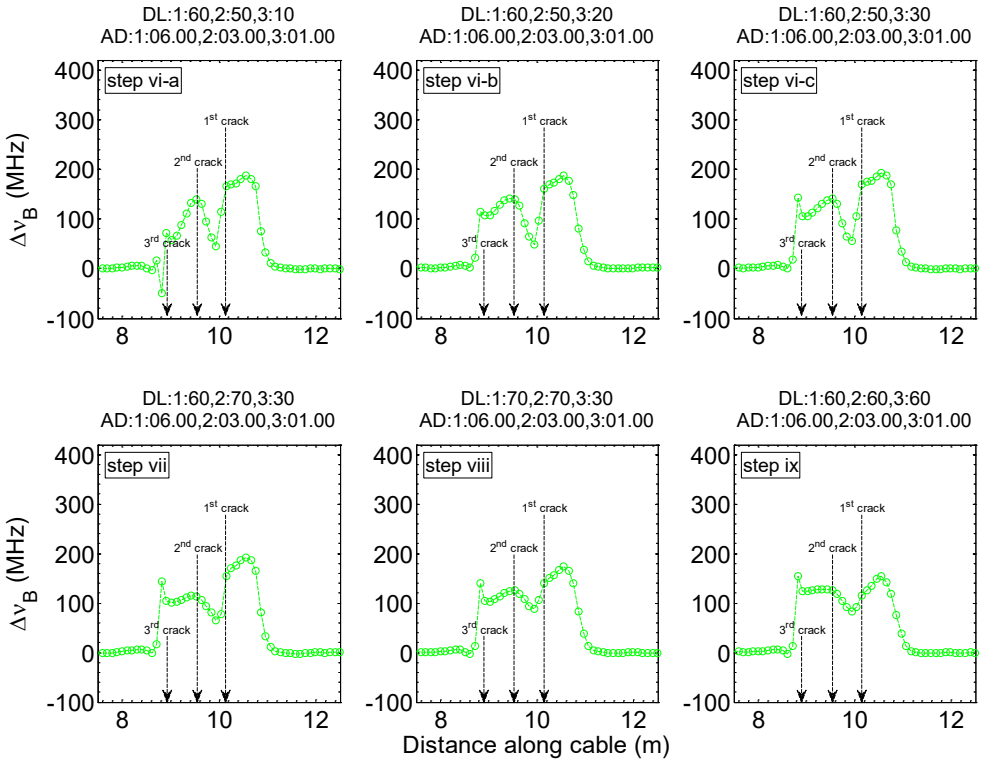

Figure B-5. Frequency response of DiTeSt™ for steps shown in Figure B-4

B.4. Low Performance Debonding Process when Sensing Cable Meeting Three Joints along an Interval

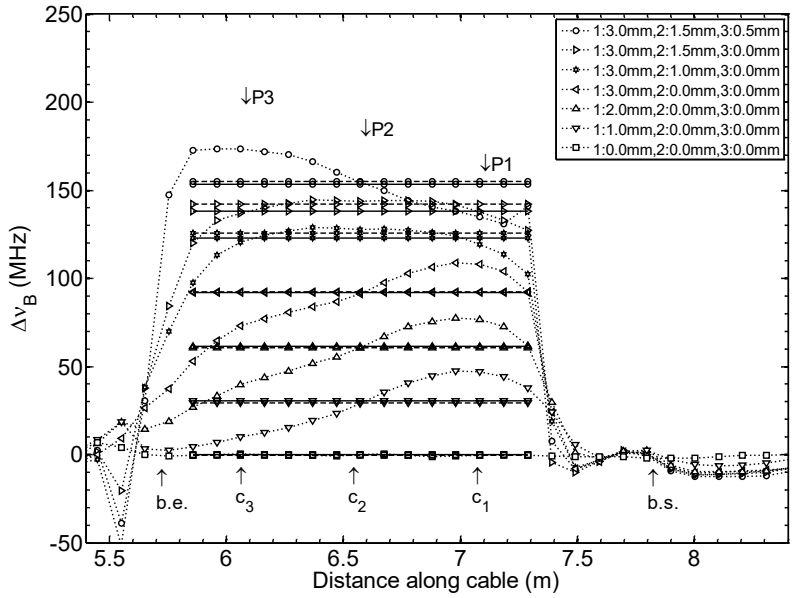

Figure B-6. Frequency response of DiTeSt™ when SMARTProfile™ is not perfectly debonded from mortar

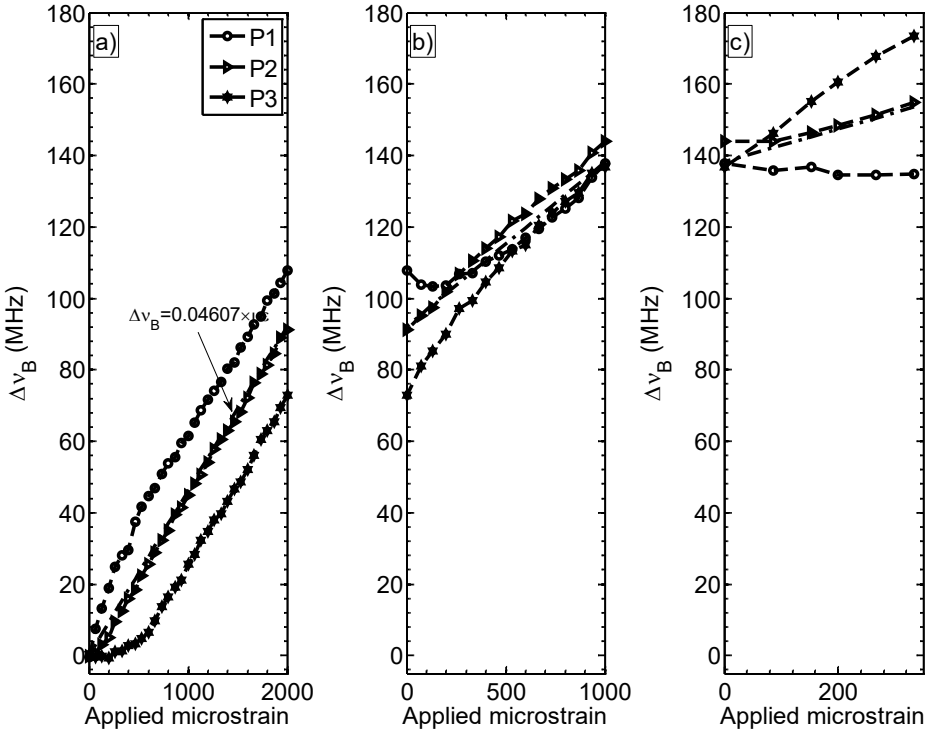

Figure B-7. Frequency-displacement response at three points (P_1, P_2,and P_3) as shown in Figure B-6

B.5. System Response in Shear Displacement with Sensing Cable Embedded in a Sand-filled Flexible Tube

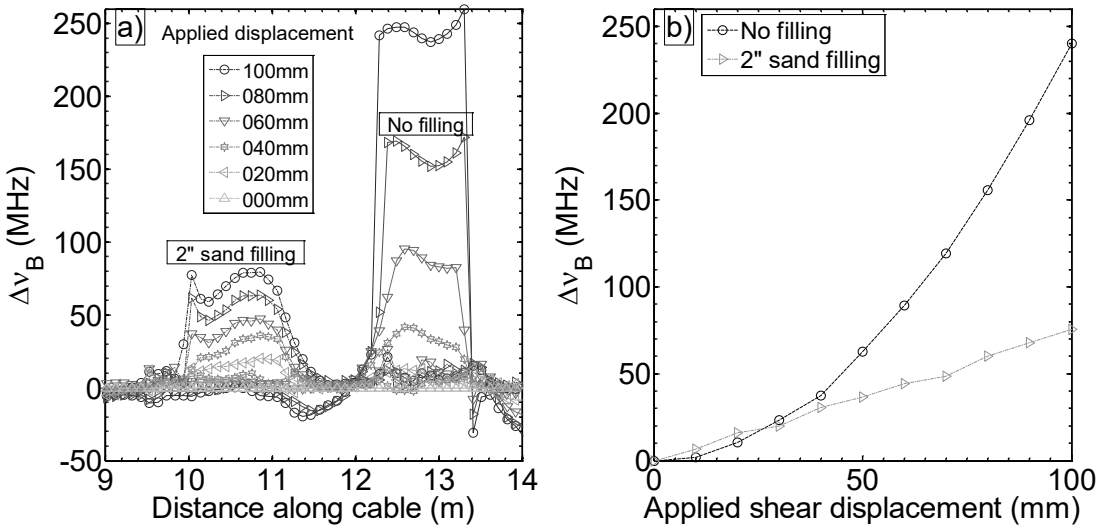

Figure 0B-8. DiTeSt™ response when SMARTProfile™ is under shear displacement within a sand-filled flexible tube